

COMPUTATIONAL STUDIES ON HEMODYNAMICS IN STRAIGHT AND BIFURCATED ARTERIES

Thesis

Submitted in partial fulfillment of the requirements for the degree of

DOCTOR OF PHILOSOPHY

by

PRASHANTHA B.



DEPARTMENT OF MECHANICAL ENGINEERING
NATIONAL INSTITUTE OF TECHNOLOGY KARNATAKA,
SURATHKAL, MANGALORE – 575025

OCTOBER, 2018

DECLARATION

I hereby *declare* that the Research Thesis entitled “**COMPUTATIONAL STUDIES ON HEMODYNAMICS IN STRIAGHT AND BIFURCATED ARTERIES**” which is being submitted to the **National Institute of Technology Karnataka, Surathkal** in partial fulfillment of the requirements for the award of the Degree of **Doctor of Philosophy** in **Department of Mechanical Engineering** is a *bonafide report of the research work carried out by me*. The material contained in this Research Thesis has not been submitted to any University or Institution for the award of any degree.

Register Number : **145007ME14F11**

Name of the Research Scholar : **PRASHANTHA B.**

Signature of the Research Scholar :

Department of Mechanical Engineering

Place: NITK, Surathkal

Date:

CERTIFICATE

This is to *certify* that the Research Thesis entitled “**COMPUTATIONAL STUDIES ON HEMODYNAMICS IN STRAIGHT AND BIFURCATED ARTERIES**” submitted by **Mr. PRASHANTHA B.** (**Register Number: 145007ME14F11**) as the record of the research work carried out by him, is *accepted as the Research Synopsis submission* in partial fulfillment of the requirements for the award of degree of **Doctor of Philosophy**.

Dr. Anish S
(Research Guide)

Chairman - DRPC
Date:

ACKNOWLEDGEMENT

I would like to extend my gratitude to Dr. Anish S, Assistant Professor, Mechanical Engineering, National Institute of Technology Karnataka (NITK), Surathkal for the invaluable constructive guidance and encouragement extended throughout my study.

I would like to thank my Research Progress Assessment Committee members Dr. Arun M. and Dr. Vishwanath K. P. for their valuable inputs. Sincere gratitude is expressed to Prof. Ravikiran Kadoli, Dr. Kumar G N and Dr. Mrithunjaya Doddamani for the help provided during my simulation work.

I would like to thank Prof. Narendranath S., Head of the Mechanical Engineering and all the members of faculty, Mechanical Engineering, NITK for their support throughout this research work.

Constant encouragement of my family to pursue higher studies has made it possible for me to reach at this stage. I wish to thank all my family members for love, help and encouragement provided. Special note of thanks to all my friends and well-wishers for their constant help, encouragement and understanding.

ABSTRACT

Hemodynamic behaviour of blood in the complexed arteries are closely related to the development of cardiovascular disease. Atherosclerosis is the major cause for the cardiovascular disease and is a chronic inflammatory process characterized by thickening of arterial wall cause for the plaque development. The secondary flows generated at the complexed zone promotes the deposition of atherogenic particles on the outer walls. The formation and subsequent rupture of the plaque depends on wall shear stress (WSS) and oscillatory shear index (OSI).

The focus of this present study is to understand the hemodynamics in the complexed region. Numerically, the analysis become more complex when a discrete phase is added to the continuous phase in order to understand the behaviour of atherogenic particles in a pulsatile flow environment. To understand the correlation between the discrete phase (atherogenic) particle behaviour with the characteristics of continuous phase (blood) under varying pulse frequencies in the post stenosis region of complexed geometries are difficult. Hence in simplified way study has been carried out with straight idealized models with different stenosis nature to analyse hemodynamics in the post stenosis region. Continuous phase is modelled by time averaged Navier-Stokes equations and solved by means of Pressure Implicit Splitting of Operators (PISO) algorithm. DPM has been carried out with one way coupling. The transport equations are solved in the Eulerian frame of reference and the discrete phase is simulated in Lagrangian frame of reference.

The study brings out the importance of helicity in the atherosclerosis progression. Result shows that the asymmetric nature of stenosis exhibits less helical flow structure and the vortical structures are not getting transported to the downstream. Consequently the average particle residence time (PRT) of the atherogenic particles are one order higher than the symmetric stenosis model. Low PRT leads to enhanced mass transport in the arterial flow and triggers further occlusion/plaque build-up at the post-stenotic region. The extent of asymmetry in a diseased artery may be considered as a useful parameter in understanding the rate of progression of atherosclerosis.

To understand the effect of pulse frequency on the hemodynamics of a stenosed arterial wall nature. For which the study has used a flexible wall nature. stenosis parts are assumed as isotropic, elastic homogeneous and incompressible. Different material properties can be assigned to each volume (part) to reflect the complexity (Healthy and diseased). For a healthy arterial wall young's modulus (E) of 0.4MPa and Poissons ratio of 0.499 are selected. Stiffness was presented in the stenosed region (diseased) hence diseased part chosen to be four times of the healthy part with a young's modulus of 1.6MPa. At each time step fluid and solid models solved individually using updated solution provided by the other part (Two way coupling). Due to the presence of larger curvature (thick wall) on one side, flow is pushed to one side of the arterial wall leading to higher stress and wall displacement in the asymmetric stenosis.

Study has implemented a new device which aims at suppressing the development of atherosclerosis plaque by inducing helical flow structure in the carotid arterial passage (bifurcated). An idealized carotid artery model, chosen for the computational study. It comprises of three bilateral arteries namely Common Carotid Artery (CCA), Internal Carotid Artery (ICA) and External Carotid Artery (ECA). The CCA empties into a smaller ECA and a large ICA. The functional requirement of the swirl generator is to minimize the relative residence time (RRT) of the fluid layer near the endothelial wall without generating any additional pressure drop. With these criteria, the grooves are provided with triangular ribs at the inner wall of the swirl generator. The parameters taken for analysis are height of the rib, the helical angle and the number of ribs. Each of these parameters are varied systematically to understand their influence on the hemodynamics and the atherogenesis. A total number of 11 different cases are analysed computationally using large eddy simulation (LES) model. It is observed that the induced helical flow redistributes the kinetic energy from the centre to the periphery. A single rib swirl flow generator proximal to the stent treated passage can generate sufficient helicity to bring down the RRT 36% without creating any additional pressure drop. The swirl flow adds azimuthal instability which increase vortex formations in the passage. The induced helical flow in the domain provokes

more linked vortices (coherent vortices), which may act as self-cleaning mechanism to the arterial wall and increase the stent life from restenosis.

Study has investigated influence of pulsatile flow on the mechanical wall parameter after swirl flow induced in the bifurcated arterial passage. Comparisons are made between bifurcated fluid wall with enhanced swirl flow generator (single rib case) and the base case simulation. Arterial wall can be considered as healthy (free from disease), isotropic, elastic homogeneous and incompressible and the Swirl generator device part can be assumed as rigid. Result shows that Vonmises stress on the interaction surface was generally found in the swirl flow inducer case behaving similar fashion way of Base case stress, which is acting on the wall. Additionally at the site of bifurcation, Vonmises stress closer to the base case. This is an evidence there is no such extra additional stress acting at the flow divergence by enhanced swirl flow in the bifurcated passage. uniformly distributed turbulent kinetic energy around the arterial periphery by induced swirl flow in the complexed geometry does not affect on the vascular injury.

Study is focused on understand the effect of hemodynamics on the spatial and temporal variation of WSS and OSI using realistic models with varying degree of carotid artery stenosis. A series of scanned Computed Tomography (CT) images of four patients covering the carotid bifurcation artery with significant carotid artery stenosis, lumen and wall surface of the carotid bifurcation were obtained. The lumen portion was traced out from the CT image using an in-house software (ImgTracerTM, courtesy of AtheroPoint, Roseville, CA, USA). The output of the ImgTracerTM is the x-y coordinates in terms of pixels. This was further converted into millimetre (based on the resolution) and then feed into a commercially available 3D geometry modeller ICEM CFD to prepare the required polylines upon which the surface will be created. Smoothing of the surface was done using 3D modelling software CATIA. A finite volume based CFD method was utilized to understand the hemodynamics in pulsatile flow conditions.

It was observed that, high stenosis models occupied a large value of normalized WSS in the ICA whereas they had smaller values of normalized WSS in the CCA. For

clinical use, present study recommend using the spatial average value of oscillatory shear rather than the maximum value for an accurate knowledge about the severity of stenosis. The bulk flow hemodynamics is represented with the direction of resultant vorticity. It reveals that, after the bifurcation zone a change of spin happens with the resultant vorticity due to the secondary flows originated from the inner wall of the bifurcation zone. Additionally, we propose the use of limiting streamlines as a novel and convenient method to identify the disturbed flow region that are prone to atherogenesis.

Study has been numerically tests the optimized conceptual design of a device (swirl generator) that generate helical flow structure in the patient specific carotid artery models. The length of the helicity generator is three times the CCA diameter and it is placed five diameter distal (-5D) to the bifurcation zone in the CCA passage. At the inlet and outlets sufficient length have been provided to enhance the fully developed flow. As a result of the helical flow movement inside the arterial passage, the kinetic energy has been redistributed from the centre of the arterial passage to the periphery. This helps in washes out the recirculation regions near the bifurcation passage. Hence fluid residence time decreases with induced helical flow in the arterial passage.

Keywords: *Stroke; Stenosis; Hemodynamics; Womersley number; Discrete phase modelling; Helicity; Carotid bifurcation; Swirl flow generator; Relative residence Time; CT; Wall shear stress; Oscillatory shear stress.*

CONTENTS

Declaration	
Certificate	
Acknowledgement	
Abstract	
CONTENTS.....	i
LIST OF FIGURES	iv
LIST OF TABLES	viii
NOMENCLATURE	ix
ABBREVIATIONS	x
1 INTRODUCTION.....	1
1.1 An overview of atherosclerosis plaque formation and development	1
1.2 Importance of fluid dynamic parameters in plaque development.....	2
1.3 Effect of helical flow in the blood vessels	3
1.4 Scope of the thesis.....	4
1.5 Objectives.....	5
1.6 Structure of the thesis	5
2 LITERATURE SURVEY	8
2.1 Plaque development and rupture	8
2.2 Anatomy of carotid bifurcated artery.....	9
2.3 Post stenotic flow behavior	10
2.4 Effect of different physiological states in the blood flow	12
2.5 Significance of helical flow in the artery	13
2.6 Summary of the chapter	15
3 STUDIES ON IDEALIZED STRAIGHT ARTERIES.....	21
3.1 The computational domain.....	21
3.1.1 Model for symmetric and asymmetric stenosis analysis.....	21
3.1.2 Models with different stenosis cross section	23
3.2 Mathematical formulation	23
3.2.1 Continuous phase modelling.....	24
3.2.2 Discrete phase modelling.....	26
3.3 Grid independence study	28
3.4 Validation	28

3.5	Results and Discussions	30
3.5.1	Effect of Womersley number on the hemodynamics.....	30
3.5.2	Analysis of the discrete phase.....	32
3.5.3	Wall shear stress distribution	38
3.6	Effect of stenosed lumen shape on hemodynamics.....	38
3.6.1	Behavior of the jet flow in the post stenosis region.....	38
3.6.2	Particle residence time analysis	41
3.7	Effect of wall displacement: Fluid structure interaction studies.....	41
3.7.1	Modelling of the physical system	41
3.7.2	Fluid modelling.....	43
3.7.3	Solid modelling.....	43
3.7.4	Coupling.....	45
3.7.5	Validation study for fluid structure interaction.....	46
3.7.6	Behavior of pulsatile flow through the flexible artery.....	47
3.8	Summary of the chapter	50
4	STUDIES ON BIFURCATED ARTERY WITH SWIRL GENERATOR	52
4.1	Computational Model.....	52
4.2	The swirl generator.....	54
4.3	Analysis of results	57
4.3.1	Relative residence time (RRT).....	57
4.3.2	Pressure loss in the bifurcated region	58
4.3.3	Descriptors for swirl flow topology.....	58
4.4	Results.....	59
4.4.1	Effect of swirl generator on the hemodynamics	59
4.4.2	Relative residence time (RRT) analysis.....	59
4.4.3	Detailed analysis on the flow modifications.....	63
4.4.4	Analysis on the induced helicity	66
4.5	Discussions.....	67
4.6	Effect of swirl generator in a flexible bifurcated artery	69
4.6.1	Distribution of wall shear stress and Von misses stress on the Elastic wall	69
4.7	Summary of the chapter	72
5	STUDIES ON PATIENT SPECIFIC GEOMETRIES	74
5.1	Geometry reconstruction from CT scan images.....	74
5.2	Fluid models and boundary conditions	76

5.3	Results and discussion.....	77
5.3.1	Effect of degree of stenosis on WSS and OSI	77
5.3.2	Understanding the bulk flow behavior through limiting streamlines plots	83
5.3.3	Resultant vorticity contours	85
5.4	Performance of swirl generator in patient specific models.....	87
5.4.1	TAWSS on the outer wall	87
5.4.2	Flow field analysis with swirl generator.....	89
5.4.3	Effect of relative residence time (RRT).....	92
5.5	Summary of the chapter	92
6	CONCLUSIONS.....	94
6.1	Studies on the symmetric and the asymmetric stenosed models.....	94
6.2	Effect of swirl flow in the idealized bifurcated artery	95
6.3	Studies on patient specific carotid artery models.....	96
6.4	Limitations and suggestions for future work.....	97
	REFERENCES	98
	PATENT	109
	LIST OF PUBLICATIONS	109
	BIODATA.....	111

LIST OF FIGURES

Figure 1.1. Development of plaque on the arterial wall.	2
Figure 3.1. Schematic representation of idealized stenosed arteries (a) symmetric stenosis (b) asymmetric stenosis with 15% eccentricity.....	22
Figure 3.2. Asymmetric stenosis geometry with different circularity at the throat region.	24
Figure 3.3. Inflow velocity profile. T_1, T_2, T_3 and T_4 are the time instances corresponding to the accelerating, peak, decelerating and base velocities used for the analysis.	25
Figure 3.4. Velocity profile at -1D and -2D axial location for various grid elements.	28
Figure 3.5. Comparison of normalized radial velocity along the axial direction at peak systolic time step.....	29
Figure 3.6. Velocity contours for symmetric stenosis model (a) $\alpha = 7.5$ (b) $\alpha = 9$	33
Figure 3.7. Velocity contours for asymmetric stenosis model (a) $\alpha = 7.5$ (b) $\alpha = 9$	34
Figure 3.8. Comparison of symmetric and asymmetric stenosis distributed Helicity contours in the post stenosis region represented at different time instance of the pulse flow for (a) $\alpha = 7.5$ (b) $\alpha = 9$ (c) $\alpha = 12$	35
Figure 3.9. Comparison of particle residence time (<i>PRT</i>) of 680 particles which are uniformly released from the inlet.....	36
Figure 3.10. Behavior of peak resided particles inside the computational domain at different Womersley numbers.....	37
Figure 3.11. Particle trajectories of the peak resided particle at different Womersley numbers.....	37
Figure 3.12. Spatial variation of wall shear stress at different womersley number (a) $\alpha = 7.5$ (b) $\alpha = 9$ and (c) $\alpha = 12$	39
Figure 3.13. Comparison of stream wise velocity profile with different stenosis circularity at deceleration time step (T_3) for $\alpha=7.5$	40
Figure 3.14. Comparison of stream wise velocity profile with different stenosis circularity at deceleration time step (T_3) for $\alpha = 12$	40
Figure 3.15. Particle residence time under different physiological state (a) $\alpha = 7.5$ (b) $\alpha = 12$	42
Figure 3.16. Spatial variation of peak resided particle behavior showed with axial velocity and particle residence time.....	43

Figure 3.17. Symmetric and asymmetric stenosis arterial wall.	44
Figure 3.18. Two-way coupling block diagram for Fluid Structure Interaction analysis.	46
Figure 3.19. Comparison of Wall Shear Stress results with Li et al., 2007 (a) One diameter proximal to the stenosis (-1D) and (b) at throat of the stenosis.	47
Figure 3.20. Distribution of stress on the stenosis arterial wall during systolic peak time instance (a) symmetric and (b) asymmetric stenosed arterial wall.	48
Figure 3.21. Comparison of a time averaged Vonmises stress and wall displacement between symmetric and asymmetric stenosis at different womersley number.	49
Figure 3.22. Velocity contours for asymmetric stenosis model at $\alpha = 7.5$ (a) Rigid wall (b) flexible wall.	49
Figure 3.23. Velocity and wall shear stress comparison made between asymmetric stenosis simulation with rigid and flexible wall assumption.	50
Figure 4.1. (a) Schematic representation of carotid artery in human body (b) Typical plaque formation in carotid artery.	53
Figure 4.2. Patient specific inflow velocity profile (Hoi et al., 2010, Gataulin et al., 2014).	54
Figure 4.3. (a) Location of the swirl generator in the arterial passage (b) conceptual design of swirl generator, where ' γ ' is helical angle.	55
Figure 4.4. Three different views of all the tested cases.	57
Figure 4.5. Relative residence time of fluid layers near the ICA outer wall compared with Base case.	62
Figure 4.6. Helicity contours for different helical angles at the bifurcation region during diastolic deceleration time step.	63
Figure 4.7. Velocity contours at an axial plane during deceleration time step.	64
Figure 4.8. Velocity vectors during diastolic deceleration time instance for different rib heights.	64
Figure 4.9. Coherent vortical structures expressed with Q criterion during diastolic instance.	65
Figure 4.10. Helicity contours (a) Peak systolic (b) Diastolic deceleration time step.	66
Figure 4.11. Quantitative analysis of helical flow strength in the bifurcated artery (a) Amount of helical flow in the domain represented with helical intensity (b) Helical flow structures in the domain.	67

Figure 4.12. Models used for the simulation (a) Base case model (b) Swirl generator case (Case-9).....	70
Figure 4.13. Comparison of wall shear stress distribution between without swirl generator and with swirl generator case (Case-9) during the cardiac pulse plotted on internal walls of ICA at bifurcation zone and in the ICA region.....	71
Figure 4.14. Von mises stress distribution at the bifurcation wall region (AA ¹) during peak cardiac cycle (a) without swirl generator (b) with swirl generator.	71
Figure 4.15. Comparison of Vonmises stress distribution between without swirl generator and with swirl generator case (Case-9) during the cardiac pulse plotted on internal walls of ICA at bifurcation zone and in the ICA region.....	71
Figure 5.1. (a) Tracing of the vessel lumen with image tracer (b) Traced points are converted into polylines in ICEM CFD (c) Final 3D model generated.	75
Figure 5.2. Carotid bifurcation models for the four models, showing the common carotid artery (CCA), external carotid artery (ECA) and internal carotid artery (ICA).	76
Figure 5.3. Computational approach for a real patient specific data.	76
Figure 5.4. Inlet pressure as a function of normalized time used for the simulation within the carotid bifurcation. The corresponding flow rate at the exit of ICA and ECA are also shown.....	77
Figure 5.5. (a) Representative model showing specific locations where the WSS values are extracted. Variation of the normalized WSS during peak systole (b) on the outer wall of the vessel lumen (c) on the inner wall (d) on a point at the outer wall during pulsatile flow (e) on a point the inner wall during pulsatile flow.....	80
Figure 5.6. Angular variation of normalized WSS at different axial locations for (a) <i>patient 1</i> (b) <i>patient 2</i> (c) <i>patient 3</i> and (d) <i>patient 4</i>	81
Figure 5.7. Variation of the OSI (a) on the outer wall of the vessel lumen (b) on the inner wall. Angular variation of OSI at different axial levels for (c) <i>patient 1</i> (d) <i>patient 2</i> (e) <i>patient 3</i> and (f) <i>patient 4</i> (The angular arrows shows the circumferential regions where the OSI value is zero).....	82
Figure 5.8. (a) Surface stream lines during peak systole (t= 0.1 s) for different geometric model (b) Limiting streamlines are shown along with the flow vectors inside the flow passage for <i>patient 4</i>	84
Figure 5.9. (a) The resultant vorticity angle with respect to X axis (b) The resultant vorticity angle at three different longitudinal planes for <i>patient 1</i> (arrow indicates location of spin change).....	86
Figure 5.10. Swirl generator in the patient specific arterial passage.	88

Figure 5.11. Variation of TAWSS along the outer wall of the arterial wall.....	89
Figure 5.12. Velocity contours at an axial plane during diastolic deceleration time step (a) <i>Patient 1</i> (b) <i>Patient 4</i>	90
Figure 5.13. Distributed helicity contours during diastolic deceleration time step (a) cases without swirl generator (b) cases with swirl generator.	91

LIST OF TABLES

Table 2.1 Detailing the importance of swirl flow in the arteries.	17
Table 3.1 Details of cross sectional shape at the stenosis region.....	23
Table 3.2 Mean particle residence time at different Womersley number (α).	37
Table 3.3 Comparison of results with Li et al (2007).	47
Table 4.1 Varied parameters during different model study.	55
Table 4.2 Comparison of swirl generator designs with base case.	61
Table 5.1 Degree of stenosis calculated for each patient.....	75
Table 5.2 Comparison of few critical attributes between the various computational models.	87
Table 5.3 Comparison of swirl generator designs with base case.	90

NOMENCLATURE

d_p	: Particle diameter	μm
H	: Helicity	m^2/s
h_1	: Helical intensity	m^2/s
h_2	: Amount of helical flow	m^2/s
L	: Tube length	m
P_1	: Area average pressure at swirl inlet	Pa
P_2	: Area average pressure at bifurcation	Pa
Q_o	: CCA Flow rate	m^3/s
Q_1	: ICA Flow rate	m^3/s
Q_2	: ECA Flow rate	m^3/s
R	: Radius of the tube	m
R	: Radius of the stenosis	m
Re	: Reynolds number	-----
Re_p	: Particle Reynolds number	-----
R_p	: Radius of the particle	μm
t	: Time step	s
T_p	: Cardiac pulse time	s
U	: Velocity of the fluid	m/s
U_{avg}	: Average velocity of the fluid	m/s
U_p	: Particle velocity	m/s
W	: Vorticity	s^{-1}
α	: Womersley number	-----
γ	: Poisson's ratio	-----
ρ	: Density of fluid	kg/m^3
ρ_p	: Density of the particle	kg/m^3
μ	: Fluid viscosity	Pa s

ABBREVIATIONS

ABG	: Arterial Bypass Grafts
AVG	: Arteriovenous Graft
CCA	: Common Carotid Artery
CT	: Computed Tomography
ECA	: External Carotid Artery
FEM	: Finite Element Method
FVM	: Finite Volume Method
FSI	: Fluid Structure Interaction
ICA	: Internal Carotid Artery
IH	: Intima Hyperplasia
LDL	: Low Density Lipoproteins
LDV	: Laser Doppler Velocimetry
MRI	: Magnetic Resonance Image
OSI	: Oscillatory Shear Index
PIV	: Particle Image Velocimetry
PRT	: Particle Residence Time
PTFE	: Polytetrafluoroethylene
RRT	: Relative Residence Time
SV-VAD	: Spiral Vortex Ventricular Assist Device
TAWSS	: Time Averaged Wall Shear Stress
WSS	: Wall Shear Stress

1 INTRODUCTION

The second most common cause of death in the world, after heart disease, is stroke. Stroke kills approximately five million people/year (Tan et al. 2008). Stroke is caused by blockage (referred as atherosclerosis) of carotid bifurcated artery which feed blood to the brain. Atherosclerosis is a cardiovascular disease of large and medium-size arteries, which involves complex interactions between the arterial wall and the pulsatile blood flow. It is an inflammatory process characterised by the thickening of artery's intima layer and causes the accumulation of plaque. Development of plaque can reduce the supply of blood flowing through the artery leading to ischemia and loss of function. The focus of the present thesis is to understand the hemodynamics of large and medium sized arteries, particularly the bifurcated arteries. Studies have been carried out on idealised arterial models as well as patient specific models to understand the importance of relevant fluid dynamic parameters that contribute to the development of atherogenesis and the subsequent plaque development. This thesis proposes the use of a novel swirl generator to induce helicity in the carotid arterial passage, thereby minimizing the occurrence of plaque formation.

1.1 An overview of atherosclerosis plaque formation and development

Arteries are blood vessels that carry oxygenated blood from the heart throughout the body, they are lined up by a thin layer of cells called the endothelium. The endothelium layer works to keep inside of arteries smooth which helps the blood flow smoothly. Blood is an inhomogeneous fluid consisting of red cells, platelets and a number of white cells. The cells are suspended in a fluid base called plasma, composed of water and a number of macromolecules. Accumulation of white blood cells, macrophages and low density lipoproteins (LDL) on arterial wall is responsible for the atherosclerosis vascular disease.

Artery wall is a three layered structure; intima, media and adventitia (Figure 1.1). Atherosclerosis begins with degenerative materials enters into a dysfunctional endothelium layer. After some years of accumulation, the lumen becomes narrowed due to the formation of plaque. Degree of lumen reduction in the artery is termed as stenosis. The sites of stenotic diseases are commonly found in the curved and complex

geometries (Shuib et al. 2010, Zhang et al. 2007). Continuous development of plaque causes narrowing of the vessel lumen, creating significant flow disturbances such as flow separation, Oscillatory+ flow, recirculation etc.

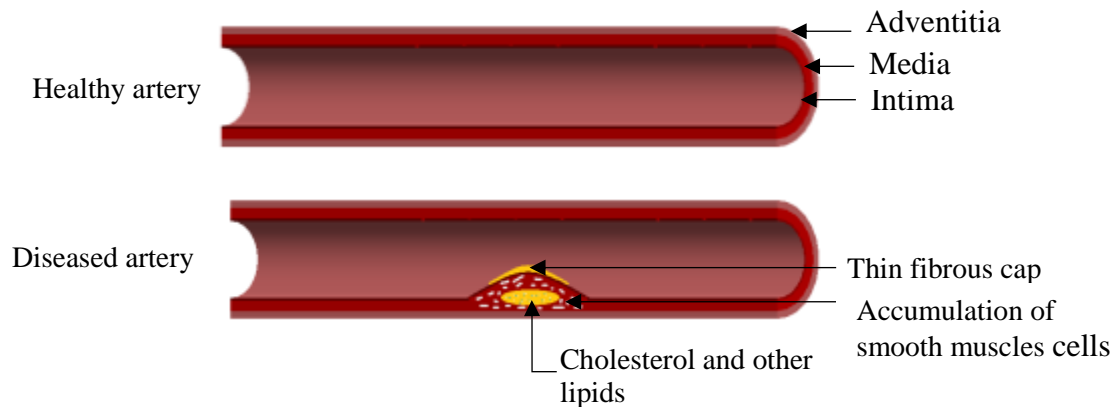


Figure 1.1. Development of plaque on the arterial wall.

Development of plaque results in the rupture of fibrous cap forming complex lesion (Shah 2003). Ruptured atherosclerotic plaque causes thrombosis (Constantinides 1984). Plaque with a large, soft, lipid-rich necrotic core and covered by a thin fibrous cap/core is more vulnerable to rupture (Lee 2000). Rupture of the fibrous cap depends not only on its biological features but also on the biomechanical and fluid dynamic factors, such as the wall shear stress (WSS), wall tensile stress, velocity, flow reversals and flow separations (Lee 2000, Richardson et al. 1989, van der Wal and Becker 1999). The fluid dynamics becomes much more complex by the pulsatile nature of the blood flow.

1.2 Importance of fluid dynamic parameters in plaque development

Hemodynamic factors are important determinants of the local distribution of atherosclerosis and the development of vascular plaques. Cardiovascular diseases are associated with abnormal blood flow patterns that may cause heart attacks and stroke (Shuib et al. 2010). Atherosclerotic plaque in the arteries most commonly forms near the bifurcation zone and curved regions of the vessel. These locations are vulnerable to high flow disturbances leading to low wall shear stress. Atherosclerosis development is affected by many hemodynamic parameters such as blood pressure, blood viscosity, wall shear stress, near wall fluid velocity, pulsations in the blood flow and complex

arterial geometry. Geometry of the vessel lumen is an important factor which influences the flow disturbance and generates pre-existing atherogenic hemodynamic environment (Liu 2007). Presence of stenosis in an artery interrupts the normal flow field. Disturbances in the stenosis region modifies further development of atherosclerosis. The relationship between arterial size and pulse frequency can be expressed in the non-dimensional Womersley number ($\alpha = R\sqrt{\omega/\nu}$) (Tutty 1992), where 'R' is the tube (artery) radius, ' ω ' is the angular frequency and ' ν ' is the kinematic viscosity of the blood. The womersley number is influenced by the physiological condition of the body and affects the hemodynamic parameters in the blocked artery. Atherosclerosis is not evenly distributed over the entire artery. The migration and adhesion of degenerative material to the walls takes place at regions where low wall shear stress, recirculations and secondary flow occurs (particularly at arterial branches, curves and bends)(Arzani et al. 2017).

1.3 Effect of helical flow in the blood vessels

High value of the Oscillatory Shear Index (OSI) and the Relative Residence Time (RRT), which indicates the time of residence the molecules spent at endothelium, have been emerging as appropriate tools for identifying the possible regions of atheromatic plaque localization (Himburg et al. 2004, Soulis et al. 2011). This points to the fact that any hemodynamic modifications in the human circulatory system that can lower the RRT, can also minimize the possibilities of atherogenises. In this aspect, inducing helicity in the arterial passage has been considered as a probable means to minimize the plaque formation.

Several studies have reported the presence of swirl/helical flow in the human circulatory system (Houston et al. 2004, Morbiducci et al. 2011, Stonebridge and Brophy 1991). Inherently, the blood flow through artery is spiral type because of the twisting of heart on its own axis (Stonebridge and Brophy 1991, Stonebridge et al. 2004). Apart from this, the physiological states and certain combination of pulsatile flow through the non-planarity of arterial wall may induce additional swirl flow pattern in the vessel (Caro et al. 1996, Gallo et al. 2012). The spiral component of blood velocity can have both beneficial and detrimental effects according to Stonebridge and

Brophy (1991). The swirl flow suppresses the localization of low density lipoproteins (LDL) and accelerates mass transport in the lumen vessel (Gataulin et al. 2015, Ha et al. 2015, Liu et al. 2015, Stonebridge et al. 2004, Sun et al. 2010, Wong et al. 2010). On the other hand, spiral flow may reduce the recirculation flow region length and results in an early breakout of transitional to turbulence (Gataulin et al. 2015, Ha et al. 2015, Ha et al. 2014, Ha and Lee 2013, Ha and Lee 2014).

1.4 Scope of the thesis

The focus of the thesis is to numerically investigate the role of hemodynamics in the atherogenesis and devise a mechanism to minimize the occurrence of plaque formations in large bifurcated arteries. Even though magnetic resonance (MR) and ultrasound based techniques have been used to provide valuable diagnostic and anatomical information, their temporal and spatial resolution is usually not sufficient for deriving information based on the differentiated velocity vector field (Papathanasopoulou et al. 2003). Computational Fluid Dynamics (CFD) techniques on the other hand can provide significant amount of information on artery blood flow dynamics with greater spatial and temporal resolution, noninvasively, on a patient. The accuracy of this technique depends greatly on reproducing accurate vascular geometry, obtaining patient specific boundary conditions and the mathematical models used for the numerical simulations.

In order to understand the atherogenesis development clearly, it is important to have thorough knowledge about the secondary flow pattern and the correlation between the discrete phase (atherogenic) particle behavior with the characteristics of continuous phase (blood). This aspect has been investigated at the initial portion of this thesis using a straight idealized stenosed artery.

The failure of stenting therapy due to restenosis and late thrombosis remains an issue for clinicians. To overcome this a novel swirl/helical generator has been proposed to enhance the helicity in the bifurcated arterial passage. Implantation of swirl flow generator in the arterial passage induces helicity to the blood flow, which washes away the atherogenic particles that may settle at the low wall shear stress regions. The proposed conceptual design of swirl generator reduces the relative residence time of the fluid layer near the walls. Further, the study has been extended to patient-specific

models. The effect of hemodynamics on the spatial and temporal variation of wall shear stress (WSS) and oscillatory shear index (OSI) has been studied on real patient data. The swirl generator has been inserted in to the patient specific artery model in order to estimate its feasibility in realistic scenarios.

1.5 Objectives

The following objectives are considered for the study:

1. To study the hemodynamics in a straight idealized stenosed artery.
 - Investigate the effect of eccentricity and circularity of stenosed lumen on the hemodynamics under different Womersley number.
 - Analyze the discrete phase (atherogenic) particle behavior with the characteristics of continuous phase (blood) under varying pulse frequencies.
 - Study the effect of wall elasticity on hemodynamics using fluid structure interaction models.

2. To study the hemodynamic behavior in an idealized bifurcated artery with swirl generator for inducing helicity.
 - Conceptual design of a novel swirl generator in the bifurcated flow passage to minimize the occurrences of atherosclerosis.
 - Study of arterial wall behavior with fluid structure interaction.

3. To analyze the hemodynamics of patient specific carotid artery models.
 - Understand the effect of degree of stenosis on the spatial and temporal variation of wall shear stress and oscillatory shear index.
 - Effect of swirl generator in patent specific carotid artery models.

1.6 Structure of the thesis

A brief structure of the thesis along with summary of individual chapters are presented below.

Chapter 1 Introduction: An overview of the research problem and the current state of the relevant knowledge is given. Scope of the thesis and the objectives of the investigations are defined.

Chapter 2 Literature survey: A detailed literature review has been carried out and is presented in this chapter. The development of plaque, the role of hemodynamics and the importance of helicity are detailed in this work. Some of the earlier methods for generating helicity in the arterial passage are detailed in this chapter.

Chapter 3 Studies on idealized straight arteries: This chapter deals with the numerical investigations for understanding the influence of helicity on particle residence time (PRT). The studies have been carried out in a straight idealized stenosed arteries. The effect of stenosis eccentricity and Womersley number on the hemodynamics has been studied through discrete phase modeling (DPM). In the later part of this chapter the effect of cross sectional shape of the lumen in a stenosed artery on the flow behavior has been presented. The lumen shape at the center of the stenosis is made an elliptical and studies has been carried out with different aspect ratios (ratio of minor axis to major axis). The chapter concludes with a study on the effect of wall displacement on hemodynamics.

Chapter 4 Studies on bifurcated artery with swirl generator: This chapter details at understanding the pulsating flow through different bifurcation geometries and devise a mechanism to suppress the development of atherosclerosis plaque by inducing helical flow structure in the arterial passage. A novel swirl generator (stent like structure with an internal groove) has been developed to induce helicity in the bifurcated passage. An ideal swirl generator is identified based on the residence time and pressure drop in the passage.

Chapter 5 Studies on patient specific geometries: In this chapter computational investigations are carried out on patient specific arterial geometries. Initially studies are carried out to understand the effect of degree of stenosis (DOS) on the temporal and spatial variations of wall shear and oscillatory shear. The study was undertaken on four different subjects whose DOSs are 41%, 56%, 62% and 69%. The effect of swirl

generator on the hemodynamics of these real arterial geometries has been studied in the later part of this chapter.

2 LITERATURE SURVEY

According to the American Heart Association, cardiovascular diseases are the number one killer in the nation (Tang et al. 2003). Cardiovascular diseases particularly atherosclerosis is responsible for 30% of death in worldwide and steadily increasing in recent years (Shuib et al. 2010). This disease is often characterised by narrowing of the artery and reduction in blood supply. Narrowing of an artery is called plaque development. Hardened arteries with atherosclerotic plaques, may rupture without warning and causes myocardial infraction (Tang et al. 2009).

2.1 Plaque development and rupture

Thickening of intimal layer of the artery is called as development of atherosclerosis. Progression of atherosclerosis plaque involves several steps. Initially white cells and macrophages are recruited by LDL accumulates in the endothelium layer (where the layer will be dysfunctional by smoking, excess of cholesterol etc.). It is a thin layer forming an interface between the circulating blood. Once the LDL crosses the thin layer of endothelium, it gets oxidized. LDL contained with macrophages and white cells transformed into foam cells. After that, fibrous cap containing smooth muscles cells are formed in order to stabilize the plaque. During these processes cholesterol, fatty substances, cellular waste products are captured inside the endothelium (Haque et al. 2014). At this point stenosis or plaque starts to develop and narrowing the blood flow passage.

Two types of plaque can be seen in the artery; these are stable and unstable (vulnerable) plaques (Teng et al. 2014). Stable plaque consists of small cholesterol and thick fibrous core whereas unstable (vulnerable) plaque has thin fibrous core (Tang et al. 2009). Interaction between the blood and plaque leads to rupture of plaque. Schoenhagen et al. (2000) identified positive and negative remodeling of plaque in the artery wall and correlated with lumen size. Positive arterial wall remodeling is related with an increase of plaque rupture whereas negative remodeling may increase internal plaque resistance to rupture. Schoenhagen et al. (2000) concluded that positive remodeling and larger plaque areas are responsible for the rupture. Atherosclerotic plaques may rupture without warning and cause acute diseases such as heart attack and stroke (Haque et al.

2014, Tang et al. 2009, Tang et al. 2004, Tang et al. 2005). Vulnerability of plaque consists of a large necrotic core, covered by a thin fibrous cap (Shah 2003, Tang et al. 2003).

Plaque is usually associated with a high degree of lumen reduction called stenosis. High degree of stenosis and pulsatile blood flow increases flow resistance in arteries, which forces the body to raise blood pressure to maintain necessary blood supply to the artery. High pressure and narrowing of the blood vessels cause high flow velocity and shear stress (Anayiotos and Papaharilaou 2011, Johnston et al. 2004, 2006). Collapse of the plaque distal to the stenosis may cause formation of the thrombosis, atherosclerosis and plaque rupture (Friedman et al. 1981, Myers et al. 2001, Tang et al. 1999). Understanding of blood flow patterns in different carotid geometries can lead to the identification of people vulnerable to atherosclerosis (Morbiducci et al. 2010, Nguyen et al. 2008). The abnormal blood flow pattern affects the risk of plaque build-up and atherosclerosis (Ethier 2002, Ku et al. 1985, Morbiducci et al. 2011, Raz et al. 2007).

2.2 Anatomy of carotid bifurcated artery

Carotid arteries are major blood vessels that supply oxygenated blood to the neck, head and face. There are two carotid arteries one at the left side and other at the right side of neck. From their origin (Aorta) common carotid arteries are named as left and right (de la Arteria and en Relación 2006). Each system comprises of three bilateral arteries namely Common Carotid Artery (CCA), Internal Carotid Artery (ICA) and External Carotid Artery (ECA). Schulz and Rothwell (2001) revealed that for each individual's vessel diameter and area ratios are different.

Atherosclerotic lesions are frequently found in carotid artery (Antiga et al. 2002, Ethier 2002, Ku et al. 1985, Perktold et al. 1991). If the curvature and bifurcations are more in arteries they are severely affected by atherosclerosis (Ma et al. 1997, Perktold and Rappitsch 1995). Berger and Jou (2000) described steady flow through the symmetric bifurcation. Pulsatile flow from the parent vessels enters in to the daughter vessels resulting secondary motions in the daughter branches. Complexed flow structures

during the cardiac cycle is responsible for the hotspots for the atherosclerosis (Jabir and Lal 2016, Ku 1997, Lantz et al. 2016).

Ma et al. (1997) Computationally studied the effect of mass transfer in the carotid bifurcation artery. Lower mass transfer regions are hot spots for the atherosclerosis disease. Wakes, recirculations and flow separation regions are responsible for the atherogenic particles to reside for the longer time which results particles starts to stick on the arterial wall (Ethier 2002, Ha et al. 2015).

Bharadvaj et al. (1982) observed that flow separation region occurs at the outer wall regions of branched artery. Flow recirculation at the sinus regions are depend on flow rate ratio Q_1/Q_0 (ICA/CCA). Experimental results of Motomiya and Karino (1984) suggests that under physiological condition $Re=600$ and Q_1/Q_0 approximate to 0.7, a standing recirculation zone is created in the sinus region. Presence of flow separation and recirculation zones in the sinus outer wall can affect the local mass transfer and interaction of blood with arterial wall, which may leads to atherosclerosis disease. Hence, due to the complexity of carotid geometry and pulse flow the plaque develops in and around the bifurcated regions (Schulz and Rothwell 2001, Teng et al. 2014).

Chiastra et al (2017) computationally demonstrated the impacts of bifurcation angle on stenosed and unstenosed geometries are negligible. Influence of wall curvature on the flow was compared with stenosed and unstenosed models. Where stenosed model curvature in the bifurcation generates one order higher magnitude of helical flow structure than unstenosed curvature. Curvature radius in the bifurcation, moderately affects near wall hemodynamics of stenosed cases.

2.3 Post stenotic flow behavior

Narrowing of blood vessels due to atherosclerosis, changes artery geometry and cause more flow disturbances in the post stenosis region. Presence of stenosis in the artery reduces supply of blood and replicates significant changes in velocity gradients and flow structures (turbulences). Depending on percentage of lumen reduction (stenosis) flow may separate from the wall and get different flow structures (Ha and Lee 2014, Jabir and Lal 2016).

Ahmed and Giddens (1984) experimentally investigated different degrees of stenosis flow behaviour in the idealized straight tube. Study has revealed WSS will be maximum at the throat region and relatively small and oscillating at the post stenosis region. Turbulence was noticed only at severe case of stenosis (>70% area reduction). Ahmed and Giddens (1984) compared steady and pulsatile flow behaviour in the stenosed artery, where permanent recirculation zones in the steady flow did not exist under pulsatile flow.

The deposition of new cells on the arterial wall will not be uniform, resulting in an asymmetric lumen (Pagiatakis et al. 2017, Paul and Molla 2012). Tang et al. (2003) extended their studies to asymmetric stenosis, complex plaque structure with mechanical properties. Asymmetric stenosis in the artery causes significant changes in the flow conditions and leads to more artery compression, higher shear stress and flow separation. Severe asymmetric stenosis causes more wall shear stress than symmetric and this may be related to the plaque rupture.

Paul and Molla (2012) carried out simulations on biological type stenosis formed eccentrically on the top wall. Results showed that wall shear stress at the upper wall is smaller, just prior to the centre of the stenosis, while it is maximum in the throat of the stenosis. In the post stenotic region wall shear stress (WSS) starts oscillating. Sudden pressure drop at the throat region causes adverse pressure gradient and it enhances recirculation region in the post stenosis region. Guleren (2013) numerically studied different stenosis nature and presented formation of separation bubbles and jets, coherent structures associated with vortex rings and horseshoe vortices, wall shear and pressure drop in the post stenosis region.

Jabir and Lal (2016) carried out numerical simulations of steady and pulsatile flows through asymmetric stenosis. During steady state simulation flow undergoes transition to turbulence in the post stenotic field. However in the pulsatile flow simulation, disturbances are present up to ten diameter (10D) distance from the throat. Pagiatakis et al. (2017) studied on coronary bifurcation lesion (CBL) with concentric and eccentric stenosis, where eccentric stenosis in the vessel influences CBLs. The salient hemodynamic flow features in the diseased artery not only depend on the degree of

stenosis, also on its nature of circularity and physiological state of the body (Banerjee et al. 2012, Buchanan Jr et al. 2000).

2.4 Effect of different physiological states in the blood flow

Stability of the flow depends not only on the velocity and the diameter of the tube, but also on the pulse frequency (Buchanan Jr et al. 2000). Increase in any of these parameter will bring the system nearer to the state at which instability can occur. The relationship between arterial size and pulse frequency can be expressed in the non-dimensional Womersley number ($\alpha = R\sqrt{\omega/\nu}$). The womersley number is influenced by the physiological condition of the body and affects the hemodynamic parameters in the blocked artery.

The non dimensional Womersley number takes care of all these variables and represents the characteristics of pulse flow in arteries. Womersley number is directly proportional to the heart beat. Caro et al. and Tutty (1992) revealed that womersley number in the artery varies from 1 to 12.5. Sherwin and Blackburn (2005) observed that pulsatile flow with a high Reynolds number and a lower womersley number can remains stable and laminar. Buchanan Jr et al. (2000) observed that increasing Womersley number in the pulsatile flow resulted in an increased disturbances in the flow.

Banerjee et al. (2012) revealed hemodynamic flow behavior under different physiological state. Increase of heart beat (pulse rate) increases the strength of vortex structure and flow patterns in the post stenotic region. Buchanan Jr et al. (2000) showed that, irrespective of the degree of stenosis, its location in the arterial system and the physiological state of the body may reflect more on the hemodynamic parameters. The womersley number in the pulsatile flow and flow wave form (flow structures) differ in different sections of arterial system. Due to increase of net shear rate secondary vortices cannot be seen at lower womersley number. During increase of Womersley number (12.5), secondary co-rotating vortices are formed distal to the primary vortex, which enhances the particle entrainment.

2.5 Significance of helical flow in the artery

The first study on the presence of spiral flows in the arteries is reported by Stonebridge and Brophy (1991). They examined presence of spiral folds on the endothelium surface in 51 out of 75 patients who underwent vascular reconstruction. Later on several studies have examined hemodynamic characteristics of swirl flow pattern in the vessel (Caro et al. 1996, Gallo et al. 2012). Preliminary studies (Gataulin et al. 2015, Ha et al. 2015, Houston et al. 2004, Liu et al. 2015, Morbiducci et al. 2011, Stonebridge et al. 2004, Sun et al. 2010, Wong et al. 2010) demonstrated the presence of helical flow might play positive roles in blood flow supply, suppressing disturbed blood flow, preventing the accumulation of atherogenic particles on the lumen surfaces of arteries and enhance oxygen transport from the blood to the arterial wall thereby reducing the atherosclerosis disease.

Stonebridge et al. (2004) developed a method of Magnetic resonance (MR) flow pattern visualization and analyzed flow characteristics of spiral and non-spiral flows in the stenosed (diseased) and non stenosed (diseased free) arteries. There was no big difference in the unstenosed conduit with spiral and non-spiral flow modeling. In the case study of stenosis conduit, spiral flows conserved coherence flow velocity, whereas the non-spiral case show loss of coherence proximal to the stenosis. Non spiral flows can produce greater inwardly directed forces just beyond the stenosis and greater outward pressures at more distal sites. Spiral flows produces lower forces on the arterial wall.

Ha and Lee (2014) examined effects of pulsatile inlet swirl flow with different intensities in the stenosed model investigated using Particle Image Velocimetry (PIV). Pulsatile swirling flow induced in the stenosed channel showed beneficial effects by reducing negative and oscillatory WSS. Vorticity component in the post stenosis regions depicted early breakdown of turbulent flows initiated by swirl flow (disturbs symmetric development of shear layers). Ha et al. (2015) revealed swirling fluid dynamic characteristics in the stenosed model using PIV. Swirling inlet flow enhance increased vortex development at the near wall region of the post stenosis region.

Increased vortices near the wall suppresses the low wake regions and enhances mixed blood flow in the near wall region.

Gataulin et al. (2015) experimentally and numerically investigated weakly swirling flow characteristics in the asymmetrically stenosed straight tube model under steady flow. They developed a procedure for measuring the reverse flow region length using ultrasonic Doppler method. Due to swirling effect the length of the reverse-flow zone in the other plane (symmetry plane) of the stenosis reduces by 5– 10%.

Paul and Larman (2009) computationally investigated the effects of spiral blood flow in a severe (75% area reduction) axisymmetric stenosis model under steady state. The corkscrew type of flow behavior was observed at the stenosis downstream under steady spiral flow at an inlet boundary condition of $Re=500$. Spiral flow effect in the vessel increases the total pressure and velocity of the blood. With increasing Reynolds number ($Re > 500$), no significant difference was noted with centerline turbulent kinetic energy between spiral and non spiral cases. However the tangential component of the velocity was influenced.

Linge et al. (2014) simulated swirl effect through spiral component of the flow field applied at the inlet using tangential velocity component. Increase of turbulence intensity in the post-stenosis region is responsible for the secondary stenosis (Ku 1997). Induced spiral flow in the stenosed vessel reduces the turbulence intensity and oscillatory shear stress in the post stenosis region. In addition, it increases the static pressure during deceleration pulse flow.

Development of Intimal hyperplasia (IH) at the end to side anastomosis was numerically investigated by Fan et al. (2008). Adding 'S'-type bypass graft has strong influences on the flow pattern. End to side anastomosis of 45° S-type graft was compared with 60° , 45° & 30° conventional grafts. Induced helical flows in the post graft suppress the formation of IH. Sun et al. (2010) compared hemodynamic influence of non-circular helical graft with circular one. When swirling flow reaches the end of the circular helical graft, its strength may not be sufficient enough to diminish the flow

disturbance. However, with modified cross sectional shape the flow disturbance got suppressed at the distal anastomosis due to its even flushing effect.

Lack of oxygen (hypoxia) plays a significant role in the initiation and progression of IH. Zheng et al. (2014) showed improved oxygen and mass transfer by helical arterial bypass graft (ABG). Shinke et al. (2008) revealed that helical stent produce less IH in the common carotid artery compared with a conventional stent. Enhanced oxygen supply in the anastomosis suppress the IH formation (Lee et al. 2001). Zeller et al. (2016) used self-expanding tubular nitinol stent (Bio Mimic 3D stent) with helical centerline and compared with a straight stent. Wong et al. (2010) studied the hemodynamic features in a spiral vortex ventricular assist device (SV-VAD) which supports cardiac patients with stubborn heart failure. They reported that spiral flow in the SV-VAD may reduce atherogenesis and stagnant zones in the flow passage. At low Reynolds number the turbulent kinetic energy is reduced by the spiral flow as it induces the rotational stabilities in the forward flow (Paul and Larman 2009) and it may acts as self-cleaning the arterial wall.

A brief summary of the importance of helical flow has been detailed in Table 2.1. From the existing literature it is clear that swirl/helical flow has positive and negative aspects which can influence the atherosclerosis.

2.6 Summary of the chapter

The following major conclusions are identified from the previous work.

- Hemodynamic flow in an artery depend not only on the degree of stenosis, but also on the pulsatile frequency of blood, Womersley number (physiological state) and helical flow nature in the blood vessel. Atherosclerosis disease occurs at sites with complex geometries, such as artery bifurcations and regions of curvature.
- Nature of deposition of new cells on the arterial wall will not be uniform, resulting in an asymmetric stenosis.

- Increase of heartbeat (pulse rate) increases the strength of vortex structure and flow patterns in the post stenotic region and it will be similar up to certain frequency. Pulsatile flow with high Reynolds number and lower Womersley number in the flow remains stable and laminar. Increasing Womersley number in the pulsatile flow resulted increase flow disturbances.
- In the present scenario, vascular diseases are solved clinically by using advanced grafting and stent methods. Reconstructed grafts may fail due to sudden thrombosis, restenosis or by infection. During physiological states, certain combination of pulsatile flow through the non-planarity of arterial wall induce swirl/helical flow pattern in the vessel.
- The swirl flow suppress the localization of LDL and accelerates mass transport in the lumen vessel. Helical flow in the cardiac pulse flushes out the atherogenic particles in the arterial passage and it may act as self-cleaning the arterial wall.
- Helical flow in the blood vessel may improve the life of artery or stent/graft. It plays positive roles in the blood flow supply, suppressing disturbed blood flow, preventing the accumulation of atherogenic particles on the lumen surfaces of arteries and enhance oxygen transport from the blood to the arterial wall.

Table 2.1 Detailing the importance of swirl flow in the arteries.

Sl No.	Author	Journal	Remarks
1	Stonebridge and Brophy (1991)	<i>The Lancet</i> , 338(8779), 1360-1361.	➤ Pioneers of reporting the presence of spiral flows in the arteries.
2	Sherwin et al. (2000)	<i>Journal of biomechanical engineering</i> , 122(1), 86-95.	<ul style="list-style-type: none"> ➤ Studied 45 deg. distal end to side anastomosis with planar and non-planar models. ➤ Non planar models breaks down existence of secondary recirculation zones present in the planar model and also reduces the distribution of low WSS in the distal side.
3	Stonebridge et al. (2004)	<i>International angiology</i> , 23(3), 276.	➤ Authors have noticed no difference in the unstenosed conduit with spiral and non-spiral flow modeling. In the case of stenosis conduit, spiral flows conserves coherence flow velocity, wherein non-spiral case flow increasingly lost coherence proximal to the stenosis.
4	Paul and Larman (2009)	<i>Medical Engineering and Physics</i> , 31(9), 1195-1203.	➤ The corkscrew type of flow behavior was observed at the post stenosis with a steady spiral flow at the inlet boundary condition (for Re=500). The turbulent kinetic energy was reduced by spiral flow effects.
5	Sun et al. (2010)	<i>Artificial organs</i> , 34(1), 22-27.	➤ A helical graft with a noncircular cross section may reduce the possibility of acute thrombus formation in the graft.

6	Wong et al. (2010)	<i>International Journal of Artificial Organs</i> , 33(12), 856-867.	➤ Study revealed that, presence of helical flow might play positive roles in blood flow supply, suppressing disturbed blood flow, preventing the accumulation of atherogenic particles on the lumen surfaces of arteries and enhance oxygen transport from the blood to the arterial wall.
7	Morbiducci et al. (2011)	<i>Biomechanics and modeling in mechanobiology</i> , 10(3), 339-355.	➤ Study has investigated complex helical flow structure arises from the existence of helical folds (asymmetries) on the Aorta wall.
8	Lee et al. (2011)	<i>Medical Engineering and Physics</i> , 33(1), 38-46.	➤ Induced helical flow in the blood vessel due to torsion effect changes large dean type of vortices produced by the curvature to a primary single vortex.
9	Linge et al. (2014)	<i>Computer methods in biomechanics and biomedical engineering</i> , 17(15), 1727-1737.	➤ Induced spiral flow in the stenosed vessel reduces the turbulence intensity and wall shear stress in the post stenosis region.
10	Ha and Lee (2014)	<i>Medical Engineering and Physics</i> , 36(9), 1106-1114.	➤ Pulsatile swirling flow induced in the stenosed channel shows beneficial effects by reducing negative and oscillatory WSS.

11	Zheng et al. (2014)	<i>Computer methods in biomechanics and biomedical engineering</i> , 17(5), 549-559.	<ul style="list-style-type: none"> ➤ Lack of oxygen in arterial walls (hypoxia) plays a very important role in the initiation, progression and development of intimal hyperplasia (IH) and thrombosis. ➤ Effect of helical arterial bypass grafts (ABG) reduces the hypoxia.
12	Gataulin et al. (2015)	<i>St. Petersburg Polytechnical University Journal: Physics and Mathematics</i> , 1(4), 364-371.	<ul style="list-style-type: none"> ➤ Steady laminar models predict experimental results when $Re < 300$. It is preferred to use K-omega SST turbulence model when $Re > 300$.
13	Liu et al. (2015)	<i>Annals of biomedical engineering</i> , 43(1), 3-15.	<ul style="list-style-type: none"> ➤ Existing helical flow in the artery play positive role in facilitating transport of blood flow and suppress disturbed blood flow, prevent accumulation of atherogenic particles.
14	Ha et al. (2015)	<i>Proceedings of the Institution of Mechanical Engineers, Part H: Journal of Engineering in Medicine</i> , 229(2), 175-183.	<ul style="list-style-type: none"> ➤ Induced swirl flow at the entrance, enhances development of vortices near wall region in the post stenosis part. Which can suppress the development of secondary stenosis.

15	Zeller et al. (2016)	<i>Circulation: Cardiovascular Interventions</i> , 9(6), e002930.	➤ Bio Mimics 3D helical stent that is designed to induce laminar swirling blood flow and elevate vascular wall shear in the treated segment.
16	Kabinejadian et al. (2016)	<i>PloS one</i> , 11(11), e0165892.	➤ The induced swirling flow through helical graft increases the wall shear stress and reduces the flow stagnation zones within the anastomotic region and the host artery.
17	Zovatto and Pedrizzetti (2017)	<i>Meccanica</i> , 52(3), 545-553.	➤ The curved streamlines and the more complex vortex wake produce an increase of energy losses in helical vessels. On the other hand this avoid the development of stagnation regions and improve the capacity of self-cleaning.
18	Chen et al. (2017)	<i>Scientific reports</i> , 7, 40724.	<ul style="list-style-type: none"> ➤ Study has developed vena cava filters, which induces helical flow in the filter-working zone to avoid blockage. ➤ The new design of the vena cava filter with the smaller thread pitch is beneficial over the traditional one. Improved local hemodynamics in the vena cava filter may reduce plaque deposition.

3 STUDIES ON IDEALIZED STRAIGHT ARTERIES

Initial portion of this chapter deals with the numerical investigations for understanding the correlation between discrete phase atherogenic particles with the characteristics of continuous phase. Particular emphasis is given to understand the effect of variations in the pulse frequencies of blood flow on the particle trajectories. Comparative studies are carried out using a straight symmetric and asymmetric stenosed tube under three different Womersley numbers. The atherogenic particles behavior is noted down in terms of particle residence time, particle velocity and the particle trajectory. As different pulse rates correspond to different physiological conditions of the artery, the present investigation attempts to identify the hemodynamic scenarios, which are more critical to atherosclerotic progression.

The later part of this chapter is devoted to understand the effect of cross sectional shape of the lumen in a stenosed artery on the flow behavior. Flow behavior in the post stenotic region may be grossly influenced by the nature of the block created by the stenosis. Hence the lumen at the center of the stenosis is made an elliptical shape with different aspect ratios (minor axis to major axis). The changes in the hemodynamics is studied when the lumen cross section varies from circular profile. Following to this, a brief comparative study about the effect of wall displacement on hemodynamics has been presented.

3.1 The computational domain

3.1.1 Model for symmetric and asymmetric stenosis analysis

The topology of arterial lumen is highly irregular and unique for each subject. Hence the simulations with patient specific geometry create difficulties in identifying and separate out the effect of any single parameter on the flow behavior. Present investigation focuses on understanding the effect of two important parameters on the hemodynamics. These are pulse frequency of the flow and the eccentricity of the stenosis. First one is a dynamic characteristic of the flow and the second one is geometry related.

The geometry of the idealized artery model is scaled up with dynamic similarity point of view. Along with the asymmetrically stenosed model, one symmetric model is also used for this study. The symmetric model acts as a basis for comparison for the asymmetric model. The dimensions of symmetric model has been taken from the model used by Ahmed and Giddens (1984) for their experimental analysis. The diameter (D) at the non-stenosed portion is taken as two inch. Though this value is far beyond the physiological range, this value is considered to compare with the experimental results of Ahmed and Giddens (1984). Similar to the experimental set up, the computational geometry is given an upstream stenotic length of $94D$ (Figure 3.1). This makes sure that the flow is fully developed before it reaches the stenosed portion. The post-stenotic region has a length of $36D$ whilst the stenosis region is having a length of $4D$. The profile in the symmetric stenosis region is varied by using a cosine function (Ahmed and Giddens 1984) and is shown below.

$$S(x) = \{(R_0 - R_0 S_0 [1 - \cos(2\pi(x - x_1)/(x_2 - x_1))]/2\} \quad (3.1)$$

$$x_1 < x < x_2$$

$$x_1 = -2D$$

$$x_2 = 2D$$

$$S_0 = (A - a)/A$$

' R_0 ' is the radius of the straight tube, ' A ' is the cross sectional area of the non-stenosed part and ' a ' is the minimum cross sectional area at the stenosis.

The asymmetry is generated by providing a 15% eccentricity ($e = \frac{\delta}{D}$) to the stenosis center in the 90° - 270° degree plane (Figure 3.1b).

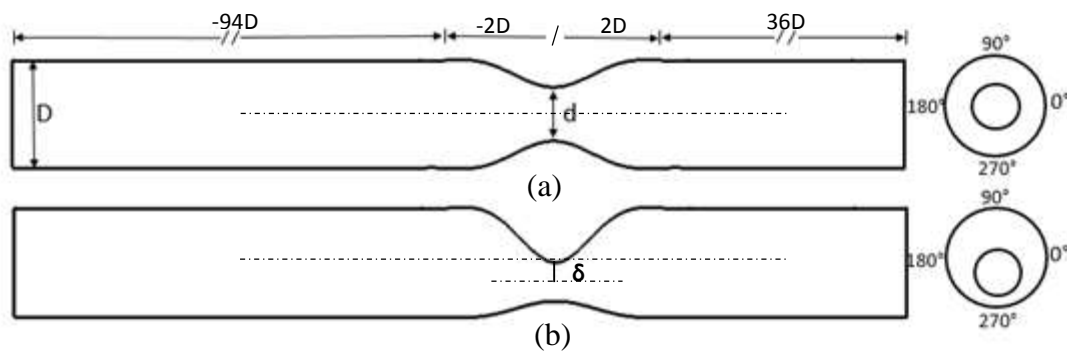


Figure 3.1. Schematic representation of idealized stenosed arteries (a) symmetric stenosis (b) asymmetric stenosis with 15% eccentricity.

The computational models has been generated using CATIA and the grid generation is carried out using ICEMCFD. The degree of stenosis (S_0) has been kept as 75% in all the numerical simulations. The boundary wall is assumed to be rigid and no slip condition is specified (Buchanan Jr et al. 2000, Frattolin et al. 2015, Lee and Steinman 2007, Li et al. 2015, Morbiducci et al. 2011). The effect of deformation of the wall is discussed at a later section.

3.1.2 Models with different stenosis cross section

The cross section of the stenosis region is having an irregular shape in real arterial geometry. To understand the effect of stenosis cross section on the hemodynamics, the lumen shape of the stenosis region is made elliptical and simulations are carried out by varying the aspect ratio (ratio of minor axis to major axis of the ellipse) of the elliptical cross section. Three different cases have been studied whose details are provided in Table 3.1. The ellipse axis length has been varied in such a manner that the degree of stenosis (75%) remains invariant for all the cases. The geometric models used for the study are shown in Figure 3.2. Apart from the deviation in the stenosis cross section region, rest of the geometric parameters are same as the asymmetric model as discussed in the previous section.

Table 3.1 Details of cross sectional shape at the stenosis region.

Case study	Major axis (m)	Minor axis (m)	Area (m ²)
<i>Case-1</i>	0.0254	0.00706	0.0005067
<i>Case-2</i>	0.02117	0.00762	0.0005067
<i>Case-3</i>	0.01524	0.01058	0.0005067

3.2 Mathematical formulation

The computational domain consists of a continuous phase, with properties similar to blood, and a discrete particular phase with similar physical properties of atherogenic particles like LDL, monocytes etc., (Ethier 2002, Tarbell 2003, Zhang et al. 2012). Finite Volume Method (FVM) coupled with Discrete Phase modelling (DPM) is used

to compute the trajectories of suspended particles in a particular flow environment. While the transport equations are solved in the Eulerian frame of reference, the discrete phase is simulated in Lagrangian frame of reference.

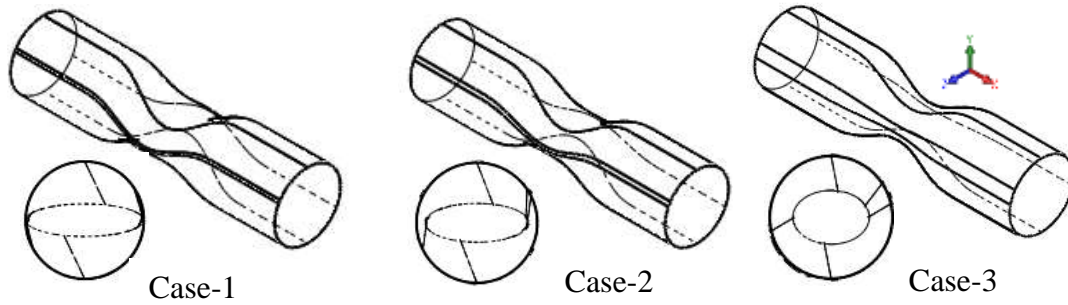


Figure 3.2. Asymmetric stenosis geometry with different circularity at the throat region.

3.2.1 Continuous phase modelling

Blood is treated as continuum and the time averaged Navier-Stokes equations are solved by means of Pressure Implicit Splitting of Operators (PISO) algorithm. The commercial software Fluent is used as the solver. PISO is a pressure-based segregated algorithm. The turbulence methodology adopted for this study is the traditional RANS simulation with standard *k-omega* model which incorporates low Reynolds number effects and shear flow spreading. Turbulence intensity of 7.2% and a length scale of 0.003556m are used as recommended to fully developed flows by Lebanon (2003). The numerical simulations are based on the three dimensional incompressible Navier-Stokes equations and can be expressed as

a) Mass conservation - continuity equation (3.2)

$$\frac{\partial \rho}{\partial t} + \frac{\partial (\rho u)}{\partial x} + \frac{\partial (\rho v)}{\partial y} + \frac{\partial (\rho w)}{\partial z} = 0$$

b) Momentum equations (3.3)

X-Momentum

$$\frac{\partial \rho}{\partial t} + \frac{\partial (\rho u^2)}{\partial x} + \frac{\partial (\rho uv)}{\partial y} + \frac{\partial (\rho uw)}{\partial z} = -\frac{\partial p}{\partial x} + \frac{1}{Re} \left(\frac{\partial \tau_{xx}}{\partial x} + \frac{\partial \tau_{xy}}{\partial y} + \frac{\partial \tau_{xz}}{\partial z} \right)$$

Y-Momentum

$$\frac{\partial \rho}{\partial t} + \frac{\partial (\rho uv)}{\partial x} + \frac{\partial (\rho v^2)}{\partial y} + \frac{\partial (\rho vw)}{\partial z} = -\frac{\partial p}{\partial y} + \frac{1}{Re} \left(\frac{\partial \tau_{xy}}{\partial x} + \frac{\partial \tau_{yy}}{\partial y} + \frac{\partial \tau_{yz}}{\partial z} \right)$$

Z-Momentum

$$\frac{\partial \rho}{\partial t} + \frac{\partial(\rho uw)}{\partial x} + \frac{\partial(\rho vw)}{\partial y} + \frac{\partial(\rho w^2)}{\partial z} = -\frac{\partial p}{\partial x} + \frac{1}{Re} \left(\frac{\partial \tau_{xz}}{\partial x} + \frac{\partial \tau_{yz}}{\partial y} + \frac{\partial \tau_{zz}}{\partial z} \right)$$

Where μ is the viscosity of the fluid, P is the pressure, ρ is the fluid density and u, v, w are the velocity components.

Inflow waveform is considered as a cosine wave similar to the one used by Ahmed and Giddens (1984) for the in-vitro analysis and the velocity profile as a function of time (t) may be expressed as

$$U(t) = \left\{ u_{avg} + \left[(u_{peak} - u_{avg}) * \cos \left(\frac{2\pi t}{T} - 2.53 \right) \right] \right\} \quad (3.4)$$

where u_{avg} is the average velocity, u_{peak} is the peak velocity, ' t ' is the time instances in the pulse and ' T ' is the pulse period time.

Figure 3.3 shows the normalized inflow waveform. Four time instances are marked on this waveform corresponding to the accelerating (T_1), peak (T_2), decelerating (T_3) and base velocities (T_4) of the pulse flow. Detailed hemodynamic analysis have been carried out at these four specific time instances. As the present study focuses only on the effect of pulse rate, similar velocity profiles are used for all the cases with varying Womersley numbers.

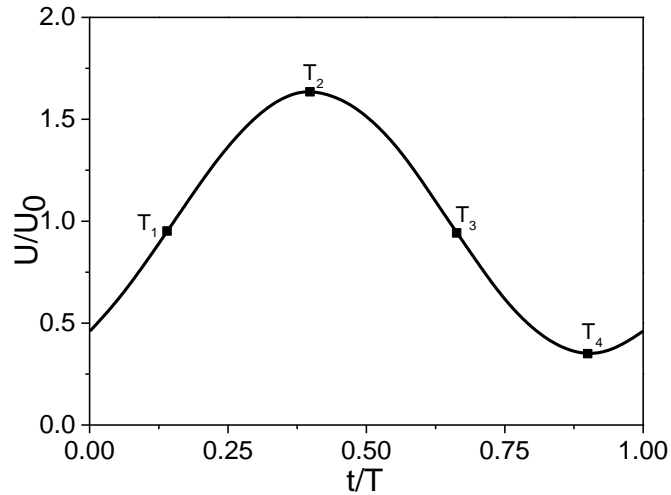


Figure 3.3. Inflow velocity profile. T_1, T_2, T_3 and T_4 are the time instances corresponding to the accelerating, peak, decelerating and base velocities used for the analysis.

To achieve similarity to the human non-bifurcating artery, Reynolds number (based on the centerline velocity) in the artery model has to be varied between 200-1000 (Ahmed and Giddens 1984, Perktold et al. 1991, Peterson and Plesniak 2008). The time period for one pulse is taken as 20s, 14s and 7.7s and the corresponding Womersley numbers (α) are 7.5, 9 and 12 respectively. Number of iterations in the inner loop has been set to 30 with a time step size of 0.001s. The convergence criterion for each time step is governed by a residual criterion of 10^{-7} . As the present study focuses on the hemodynamic through large arteries, blood is modelled as Newtonian fluid with density and dynamic viscosity of 1000Kg/m^3 and 0.0036014 Pa s respectively (Ahmed and Giddens 1984, Banks and Bressloff 2007, Mukherjee et al. 2016, Zhang et al. 2007). Iterations are carried out for sufficient number of pulse cycles until the solution meets the convergence criteria.

3.2.2 Discrete phase modelling

Discrete Phase modelling has been carried out by tracking a number of particles through the calculated flow field of continuous phase. Particle interaction with the local flow structures plays a significant role hence the modelling has been carried out with one way coupling. The influence of continuous phase on particles behaviour alone is significant and the continuous phase is not affected by the particles. This assumption is fairly applicable, as the discrete phase has only a volume fraction of 2% in the computational domain. The atherogenic particles are assumed to be spherical with mean diameter of 5 microns. Particles are released from the inlet surface uniformly and they are accelerated by the resultant force upon interaction with the continuous liquid phase. The particle-wall interaction is assumed to be an elastic collision and modelled accordingly. Interaction between the wall and particles are described with coefficient of restitution (e_n) and it can be expressed as

$$e_n = \frac{v_{2,n}}{v_{1,n}} \quad (3.5)$$

where v_n is the particle velocity normal to the wall and subscripts 1 and 2 refers before and after the collision. A normal or tangential coefficient of restitution equal to one implies that the particle retains all of its normal or tangential momentum after the

rebound (an elastic collision law). Elastic collision sometimes it will be less than one also, it depends upon the property of the particles. A normal or tangential coefficient of restitution equal to zero implies that the particle retains none of its normal or tangential momentum after the rebound (Lebanon 2003). In case of a moving wall the coefficients need to consider the velocity of the wall. The trajectory of a discrete phase particle was predicted by integrating the force balance on the particle. In a Lagrangian frame of reference the particle's inertia with the force can be written as follows equation (3.8).

$$\frac{dx}{dt} = u_p \quad (3.6)$$

$$\frac{d\vec{u}_p}{dt} = F_D(\vec{u} - \vec{u}_p) + \frac{\vec{g}(\rho_p - \rho)}{\rho_p} \quad (3.7)$$

$$F_D = \frac{18\mu C_D Re_p}{\rho_p d_p^2 24} \quad (3.8)$$

here F_D is the drag force per unit particle mass, \vec{u} is the fluid phase velocity, \vec{u}_p is the particle velocity, ρ_p is the particle density, ρ is the fluid density, μ is the viscosity of the fluid, and d_p is the particle diameter and Re_p is the particle Reynolds number based on the relative velocity between particle and fluid. The term $\frac{\vec{g}(\rho_p - \rho)}{\rho_p}$ represents the buoyance force. The particles are assumed to be floating along with the blood stream hence buoyancy force can be treated as neutral. The spherical drag law by Morsi and Alexander (1972) is used to get the value of C_D .

$$C_D = \frac{24}{Re_p} \quad \text{for } Re_p < 1 \quad (3.9)$$

$$C_D = \frac{24}{Re_p} (1 + 0.015 Re_p^{0.687}) \quad \text{for } 1 < Re_p < 400 \quad (3.10)$$

$$Re_p = \frac{\rho d_p |\vec{u} - \vec{u}_p|}{\mu} \quad (3.11)$$

The trajectory equations of the particle are solved by stepwise integration over discrete time steps. Integration of time in Equation 3.6 yields the velocity of the particle at each point along the trajectory. The differential equations are solved using Euler implicit discretization schemes.

3.3 Grid independence study

Roache (1998) identified grid-convergence studies are the most reliable technique for the quantification of numerical uncertainty. The results of the numerical simulations must be independent of the number of grids used for the simulations. The grid independency study is also helpful to arrive at an optimum number of grids and to reduce computational time without compromising the accuracy of the solution. Hence simulations are carried out for different number of grid elements keeping the same boundary conditions and the results are compared.

The radial distribution of axial velocity profile has been plotted at one diameter ($1D$) and two diameter ($2D$) distance before the throat region of symmetric stenosis. The finest grid consisted of 0.87 million elements and this has been taken as the reference grid to which results from other grids are compared. The coarse grid with 0.35 elements are deviating far away from the finest grid. On the contrary, grids with 0.78 million and 0.58 million elements show close match with the finest grid (Figure 3.4). Hence, further numerical simulations are carried out on grid with 0.58 million elements due to the better accuracy and smaller computational time (15% lower than the convergence time of the finest grid). Similar procedure is adopted for all the straight idealized models also and optimum number of grid elements is identified to be 0.87 million.

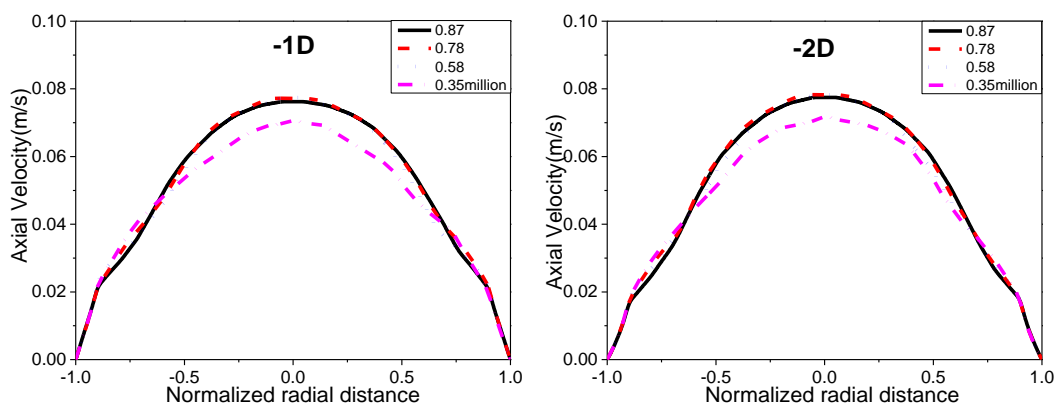


Figure 3.4. Velocity profile at $-1D$ and $-2D$ axial location for various grid elements.

3.4 Validation

Validation and verification are the primary step in any computational modeling, both are similar in measuring or estimate the errors (Babuska and Oden 2004). Validation

involves comparison of numerically predicted model results with observed physical model. In the numerical simulations of pulsatile flow through an idealized stenotic long tube, accurate results can be obtained only if the solution method is too appropriate. The causes of errors rise during discretizing and converging of Navier-Stokes governing equations. Hence, validation is an essential step in numerical simulations.

In the present study, numerical results are validated with experimental results of Ahmed and Giddens (1984) for the symmetric stenosed model under pulsatile flow. Comparisons are made for the radial variation of normalized axial velocity profile (U/U_0) at different axial locations, (viz. $1D$, $1.5D$, $2.5D$ and $4D$ distance) downstream to the minimum cross sectional area (throat region) of stenosis. The results are plotted during peak cardiac time step (T_2) and numerical results obtained through RANS based simulations as well as large eddy simulations are shown in Figure 3.5. The LES results matches both quantitatively and qualitatively with the experimental results well. Beyond $4D$ distance, RANS results are under-predicted in comparison with the experimental values which has been also reported and justified previously by Ryval et al. (2004) and Tan et al. (2008). For the present discrete phase analysis RANS has been selected, because the use of LES coupled with a lagrangian field incurs higher computational cost. However, for analysis through bifurcated channel LES has been used (Chapter 4).

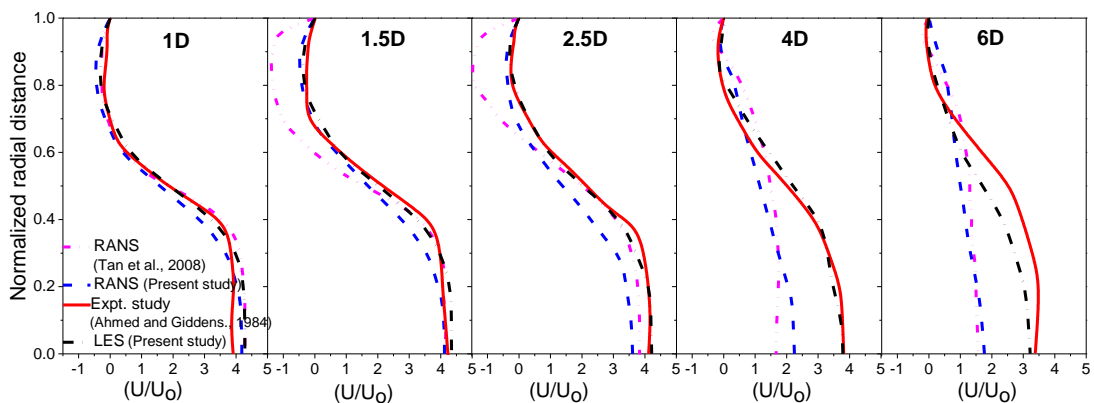


Figure 3.5. Comparison of normalized radial velocity along the axial direction at peak systolic time step.

3.5 Results and Discussions

3.5.1 Effect of Womersley number on the hemodynamics

As mentioned earlier, simulations are carried out at three different Womersley numbers (α) representing different pathological condition of a diseased human artery. To understand the three dimensional flow pattern, in the post-stenotic region, velocity contours are plotted at two orthogonal planes (0° - 180° and 90° - 270° planes). The evolution and development of the recirculation zones are monitored during the accelerating (T_1), peak (T_2), decelerating (T_3) and base points (T_4) of the pulse flow.

Figure 3.6 represents the velocity pattern for symmetrically stenosed model. A well-known jet type flow can be observed at the stenosis throat with thin shear layer that separates the recirculation zone at the periphery. The length of the jet region varies in accordance with the inlet flow profile. At higher Womersley number the symmetric nature of jet changes and the recirculation zones varies its size and shape with the pulsatile flow. As a result, recirculation region on one side get thicker and pushes jet to the opposite wall. This results in a swaying movement of the jet region. It is to be noted that, with increase in Womersley number, length of the jet region diminishes with growing instabilities. At peak time step, the length of recirculation zone becomes smaller and point of reattachment shift closer to the stenosis region.

For the asymmetric stenosis model also, the swaying motion of the jet region and the flow disturbances increases with Womersley number (Figure 3.7). However, symmetric nature of the velocity profiles no longer exists in the two selected orthogonal planes. In the 90° - 270° plane (where the asymmetry is visible) the jet region bend towards the point of primary recirculation zone. Accordingly, opposite to the point of reattachment, a secondary recirculation zone develops. Long et al. (2001) observed ring shaped vortex structure at six diameter distal to the stenosis, which is formed by combination of primary and secondary vortices. In the present investigation also, this phenomenon is observed at lower Womersley number. However at higher Womersley number an additional tertiary vortex is formed due to the higher instabilities and swaying movement of the jet region.

A better insight into the blood flow behavior can be obtained by looking at the helicity contours. Helicity defines projection of a spin vector and represents the alignment of vorticity vectors in the fluid stream. Helicity is important at a fundamental level in relation to flow kinematics and it states topological interpretation in relation to the linkages of vortex lines of the flow. If the spin vectors points in the same direction as the momentum vector then the helicity is positive and if it is in the opposite directions then the helicity is negative. Helicity contours changes its sign across a separation or reattachment line (Moffatt and Tsinober 1992). Helicity sign is a useful indicator of the rotational direction and density of the swirling fluid. It can be expressed mathematically as $H = \int \mathbf{U} \cdot \boldsymbol{\omega} \, dV$ where ‘U’ is the absolute velocity and ‘ ω ’ is the vorticity.

Figure 3.8 shows the comparison of helicity plots for symmetric and asymmetric stenosis model. Proximal to the symmetric stenosis, strong helical structures but with opposite sign are seen emerging from the upper and lower wall. Symmetric stenosis exhibits stronger linked vortices in comparison with the asymmetric case. Asymmetric stenosis model exhibits less helical flow structure than the symmetric stenosis model. Stretching of vortices and strong velocity fluctuations (weaker velocity zones) in the post-stenotic regions are the main causes for the distribution of weak helicity contours in the flow field (Hunt and Hussain 1991). In other words, the vortical structures or the flow disturbances are not getting transported to the downstream side of the flow. This indicates that, the probability of the atherogenic particles settling down at the post-stenotic region is much higher with increasing asymmetry of the stenosis.

The symmetric stenosis induces more helicity in the flow structure. Due to the spinning nature flow the chances of occlusion of new cells on the arterial wall are rare. If the flow carries multiple linked vortices with high velocities then it can washes out the atherogenic particles along the arterial passage. This has been demonstrated by the works of (Ha et al. 2015, Zovatto and Pedrizzetti 2017) and it may suppress the further development of plaque. The helicity responds positively to the increase in the Womersley number. In the present investigations, the Womersley number is varied by increasing the pulse rate. Hence, an enhanced pulse rate during exercise or work out may increase the helical nature of the flow which washes out the atherogenic particles and minimizes the chances of plaque progression distal to stenosis. For the asymmetric

stenosis model, strong helicity contours are absent, instead the presence of wake formation in the post-stenosis region makes the particles to settle on the wall. The linking of the vortices and their transportation along the mean blood flow is not seen even at higher Womersley number.

3.5.2 Analysis of the discrete phase

At the inlet of the computational domain particles are distributed uniformly with a velocity that matches with the continuous phase and allowed to mix up with the transient pulsatile flow. The time required for the particles to travel from $-2D$ distance proximal to the stenosis to $6D$ distance distal to the stenosis location are calculated to get the Particle Residence Time (*PRT*). The *PRT* is defined as follows (Buchanan Jr et al. 2000)

$$PRT = \frac{T_{Trans}}{T_{Steady}} \quad (3.12)$$

where T_{Trans} is the time spend by the particle in the selected domain during transient simulation and T_{steady} is time spend by the particle in the selected domain during steady state condition (i.e. at mean Reynolds number flow). As the computational effort involved in the discrete phase modelling is too high, simulations are carried out only for the two Womersley numbers (viz. 7.5 and 12). A total of 680 particles have been introduced at inlet and their PRT analysis is shown in Figure 3.9.

The analysis reveals that *PRT* of asymmetrical model is one order higher than the symmetric case. As there are multiple recirculation zones in the post-stenotic region of an asymmetric stenosis model, particles undergo looping and need longer time to escape from it. The mean particle residence time is shown in Table 3.2. The average residence time (mean *PRT*) for the symmetric stenosis model decreases with the Womersley number which can be attributed to the increased helicity in the symmetric stenosis model. On the other hand, the mean *PRT* value increases with the Womersley number for asymmetric stenosis model. This contradicting behavior of asymmetric model is due to the presence of large localized recirculation zones. Unlike the symmetric model, the vortices formed in the post-stenotic regions are not getting carried away in the asymmetric model. The axis of the spinning vortices need not necessarily lie in the

mean flow direction and hence there may not be a large value for helicity even though high flow disturbances and swirling strength are present for asymmetric stenosis model.

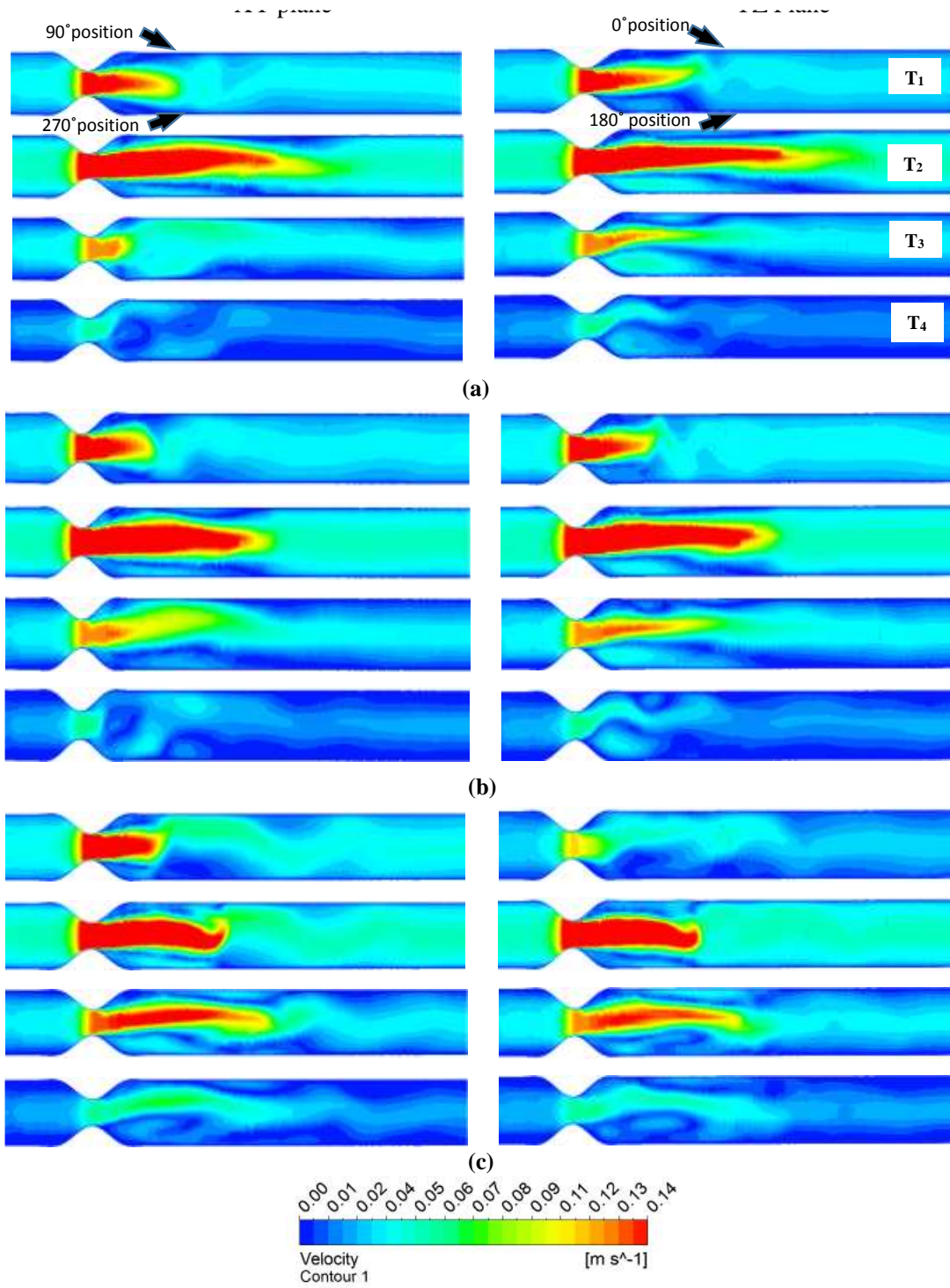


Figure 3.6. Velocity contours for symmetric stenosis model (a) $\alpha = 7.5$ (b) $\alpha = 9$ (c) $\alpha = 12$.

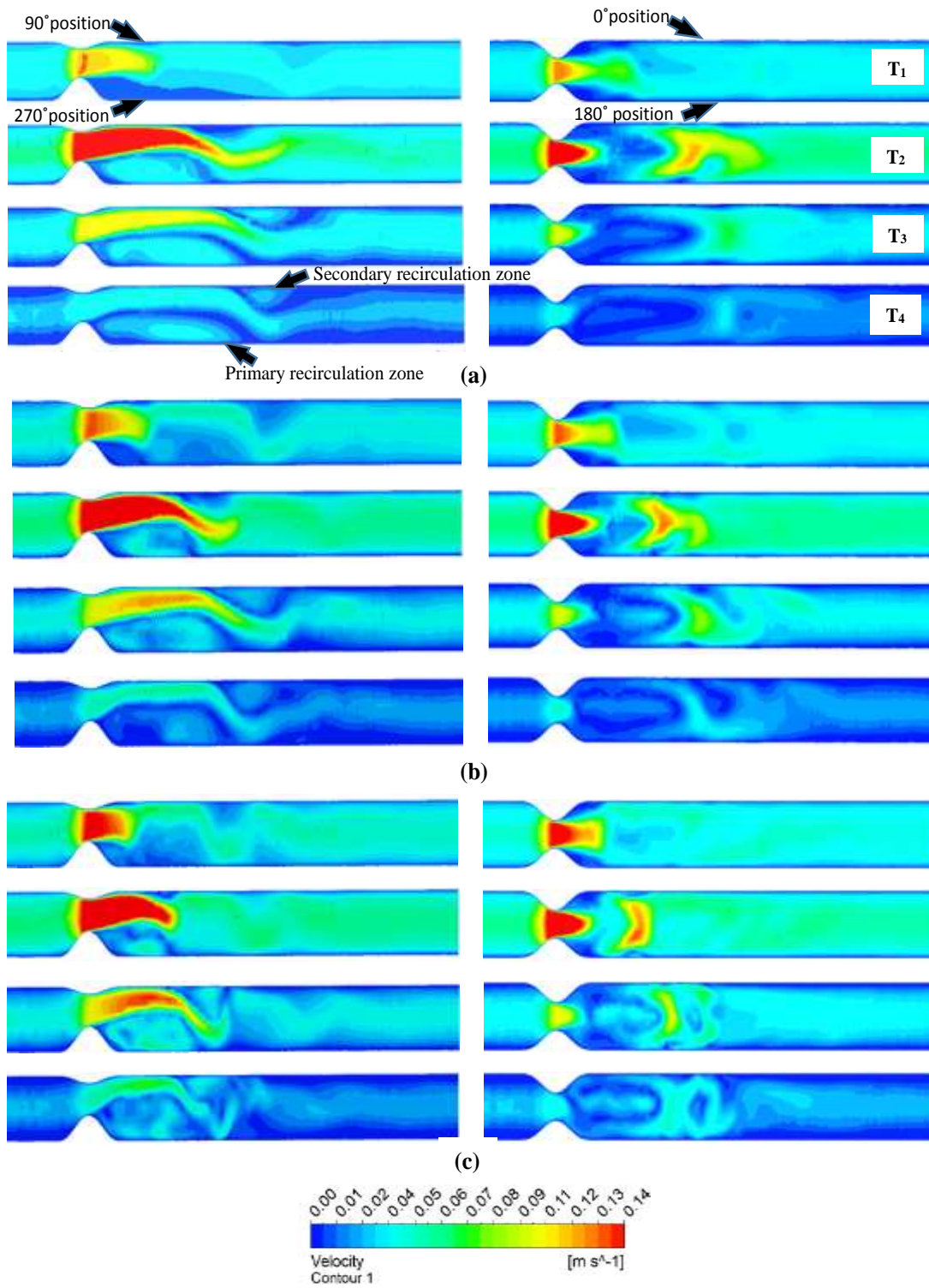


Figure 3.7. Velocity contours for asymmetric stenosis model (a) $\alpha = 7.5$ (b) $\alpha = 9$ (c) $\alpha = 12$.

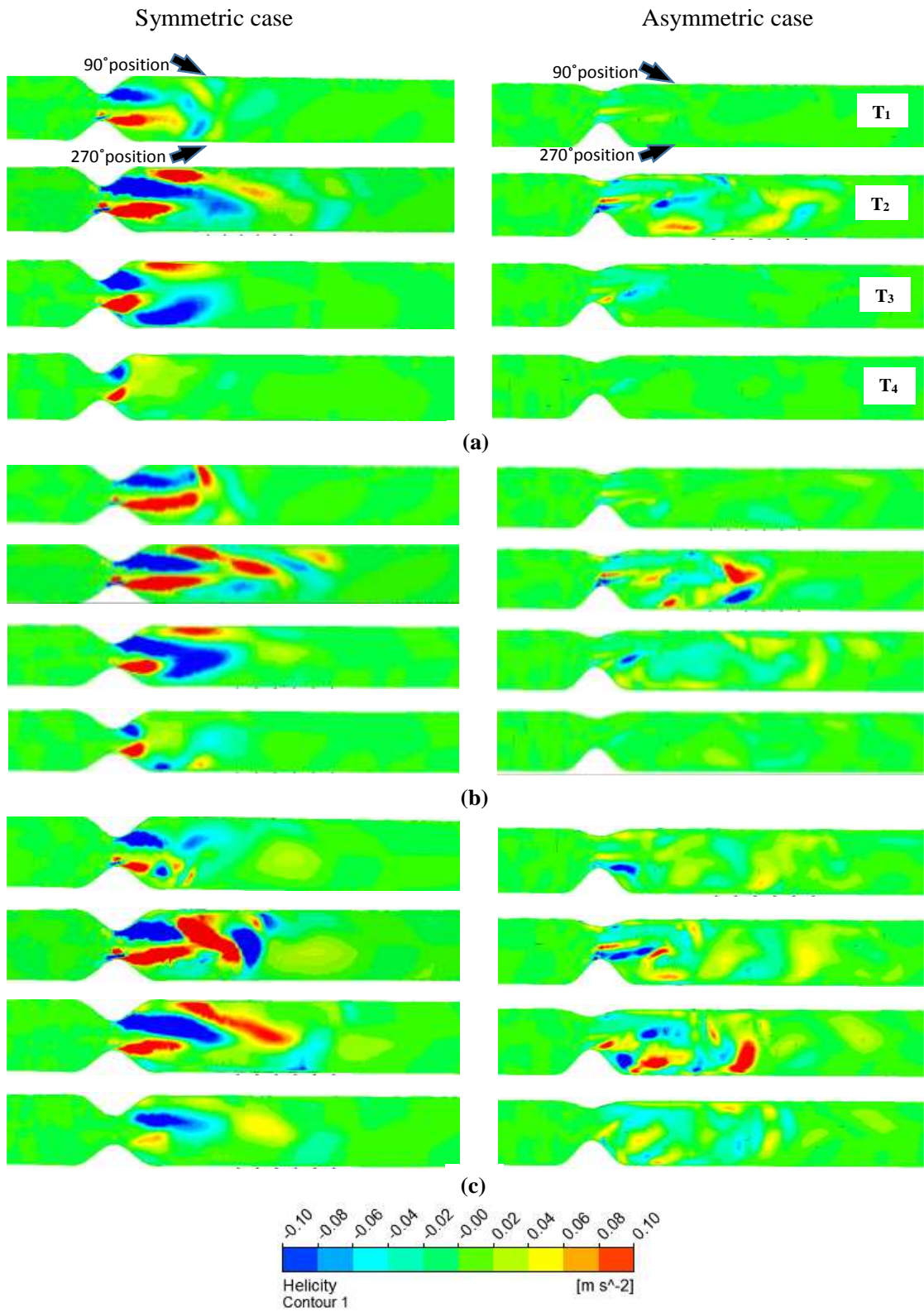


Figure 3.8. Comparison of symmetric and asymmetric stenosis distributed Helicity contours in the post stenosis region represented at different time instance of the pulse flow for (a) $\alpha = 7.5$ (b) $\alpha = 9$ (c) $\alpha = 12$.

Plotting the trajectories of all the seeded particles in a single graph makes it cumbersome. Instead, the behaviour of peak resided particle inside the computational domain is shown in Figure 3.10. The particles velocity and residence time are plotted against axial location. An axial distance zero refers to the minimum cross sectional area (throat) of the stenosis. The axial velocities of the particles are almost similar for symmetric and asymmetric model up to the stenosis throat, beyond that significant differences are spotted in their behaviour. The particle trajectories of peak resided particle in a three dimensional space is shown in Figure 3.11. The erratic behavior of the particles in the asymmetric model can be observed from this, especially at higher Womersley number. The effect of weaker flow regions near the wall enhances the *PRT* in the post stenotic region which triggers further occlusion/plaque build-up (Fatourae et al. 1998, Ma et al. 1997). This suggests that understanding the extent of asymmetry in a diseased artery may be useful as the patient with higher eccentricity in stenosis may encounter a faster progression of atherosclerosis.

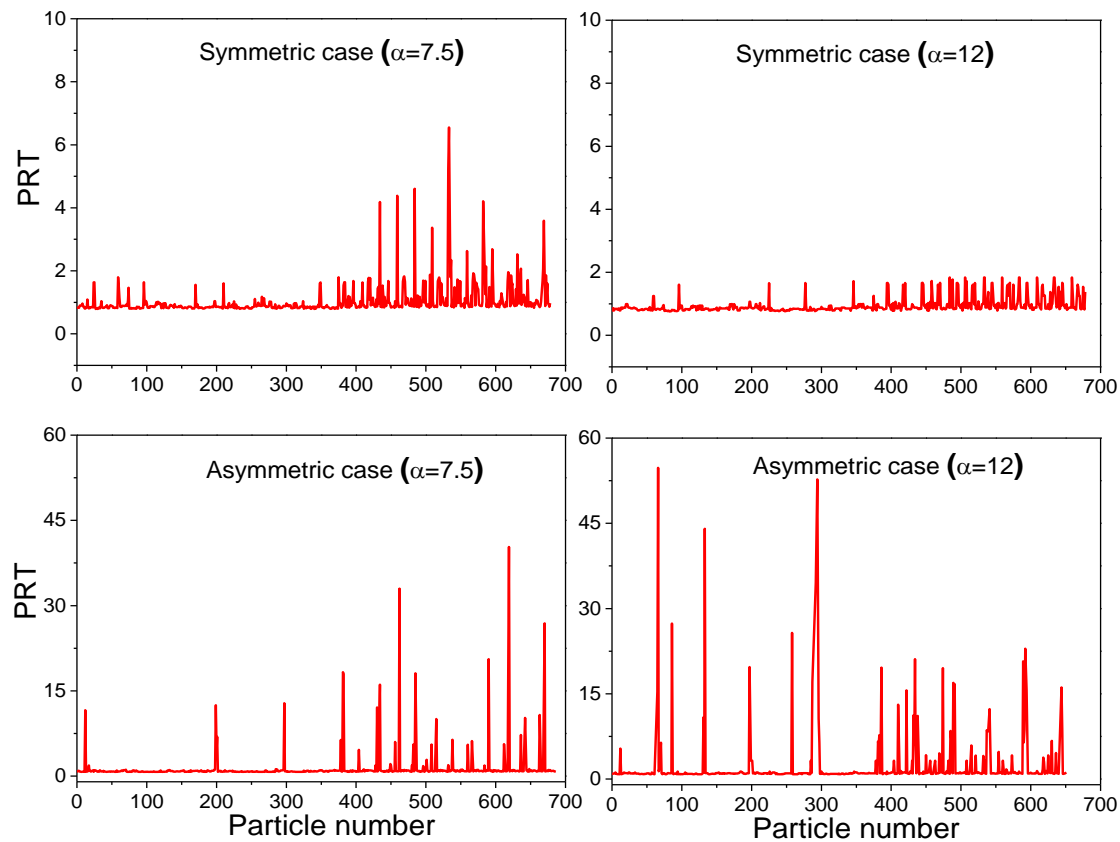


Figure 3.9. Comparison of particle residence time (*PRT*) of 680 particles which are uniformly released from the inlet.

Table 3.2 Mean particle residence time at different Womersley number (α).

Stenosis	Womersley number(α)	Mean PRT (-2D to 6D)
Symmetric case	7.5	1.025347
	12	0.938191
Asymmetric case	7.5	1.410647
	12	2.175722

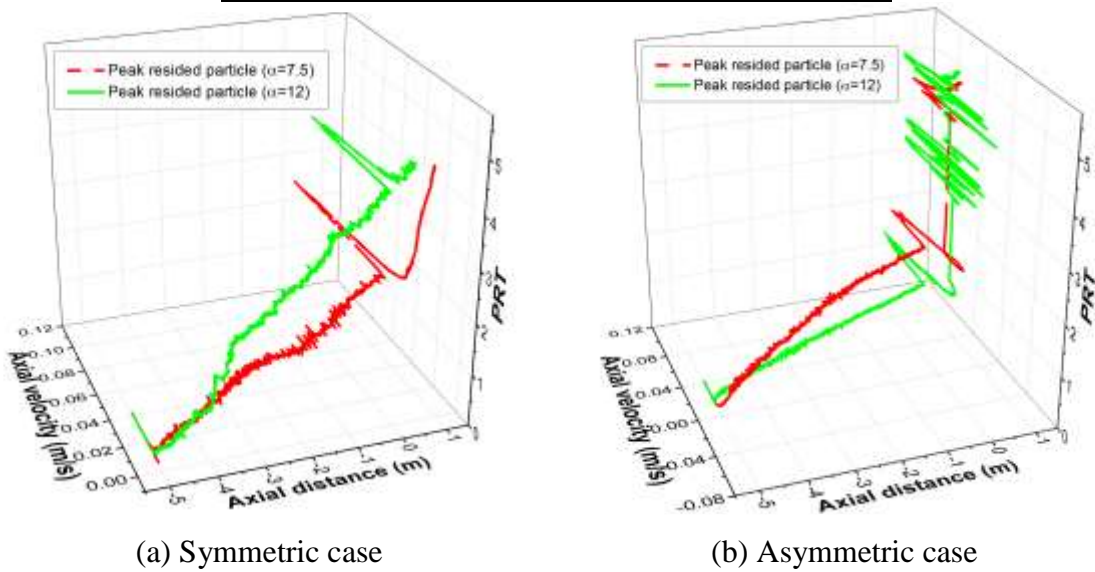


Figure 3.10. Behavior of peak resided particles inside the computational domain at different Womersley numbers.

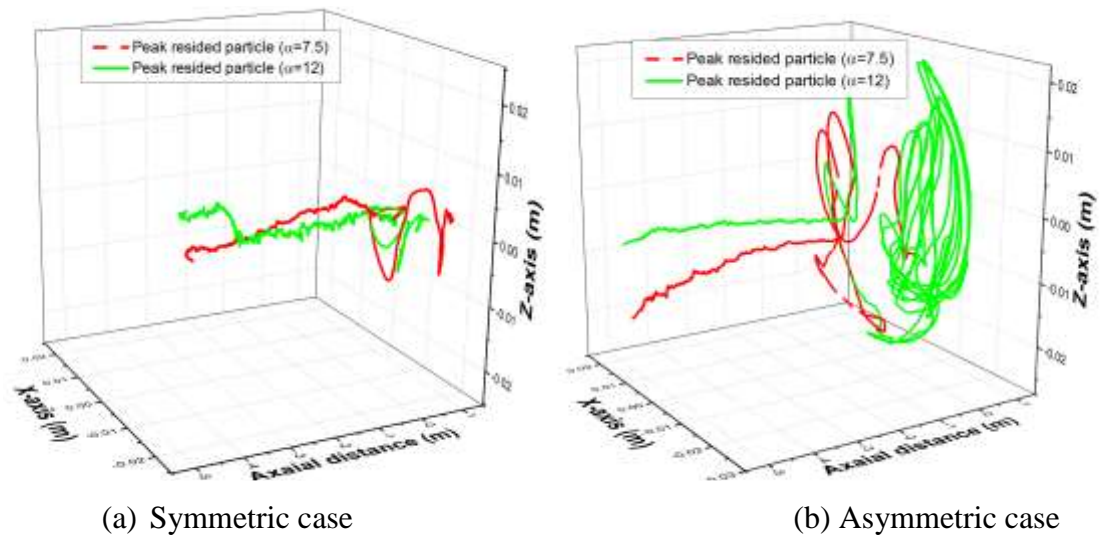


Figure 3.11. Particle trajectories of the peak resided particle at different Womersley numbers.

3.5.3 Wall shear stress distribution

Flow separation zones breaks into two parts in the post-stenotic region during systolic deceleration time instance (Long et al. 2001) and the flow disturbances are also high during this time instance. Hence, it is worth to analyze wall shear stress (WSS) distribution during deceleration time step (T_3). The asymmetry of the stenosis lies on the 90° - 270° plane and the primary and secondary recirculation zones are more visible in this plane. Hence the wall shear stress variations are noted on two polylines, which are running along the 90° and 270° angular position of the arterial wall from $-2D$ distance to $14D$ distance. An increase of frequency in the pulse provokes more oscillations in the flow field, which are reflected in the WSS distribution also in the form of ups and downs. The WSS values are normalized with their corresponding spatial average value and shown along the axial directions in Figure 3.12.

The normalized value of WSS for an asymmetric stenosis model is lower than the symmetric one in one side of the arterial wall (90°). The WSS peaks at the stenosis throat region (corresponds to zero axial location) and comes to a steady value at an axial location of $0.5m$. Majority of the oscillations in the WSS values are focused close to the stenosis region for the symmetric model. Whereas in the case of an asymmetric stenosis model, the undulations are more sever slightly away from the stenosis region, more specifically at regions between $0.15m - 0.35m$. These oscillations in the WSS values are triggered by the presence of secondary vortices which are seen only in an asymmetric stenosed artery. The WSS value rises at the point where the primary vortex reattaches to the wall. In other words, blood flow is constricted at the reattachment point due to the blockage created by the secondary vortices. This causes a rise in the WSS at this location and it become stronger at higher Womersley number.

3.6 Effect of stenosed lumen shape on hemodynamics

3.6.1 Behavior of the jet flow in the post stenosis region

Different stenosis circularity in the diseased arteries effects on scattering of jet flow during cardiac cycle (Zhang et al. 2007). The details of geometry corresponding to case 1,2 & 3 are given in Table 3.1. Radial variation of axial velocity is plotted at different axia locations ($1D$, $1.5D$, $2.5D$, $3D$ and $4D$) and shown in Figure 3.13. The

plots are made at peak time step as well as deceleration time step. The shear layers which are formed by stenotic jet oscillates in the post stenotic region with respect to pulse rates (different womersley number).

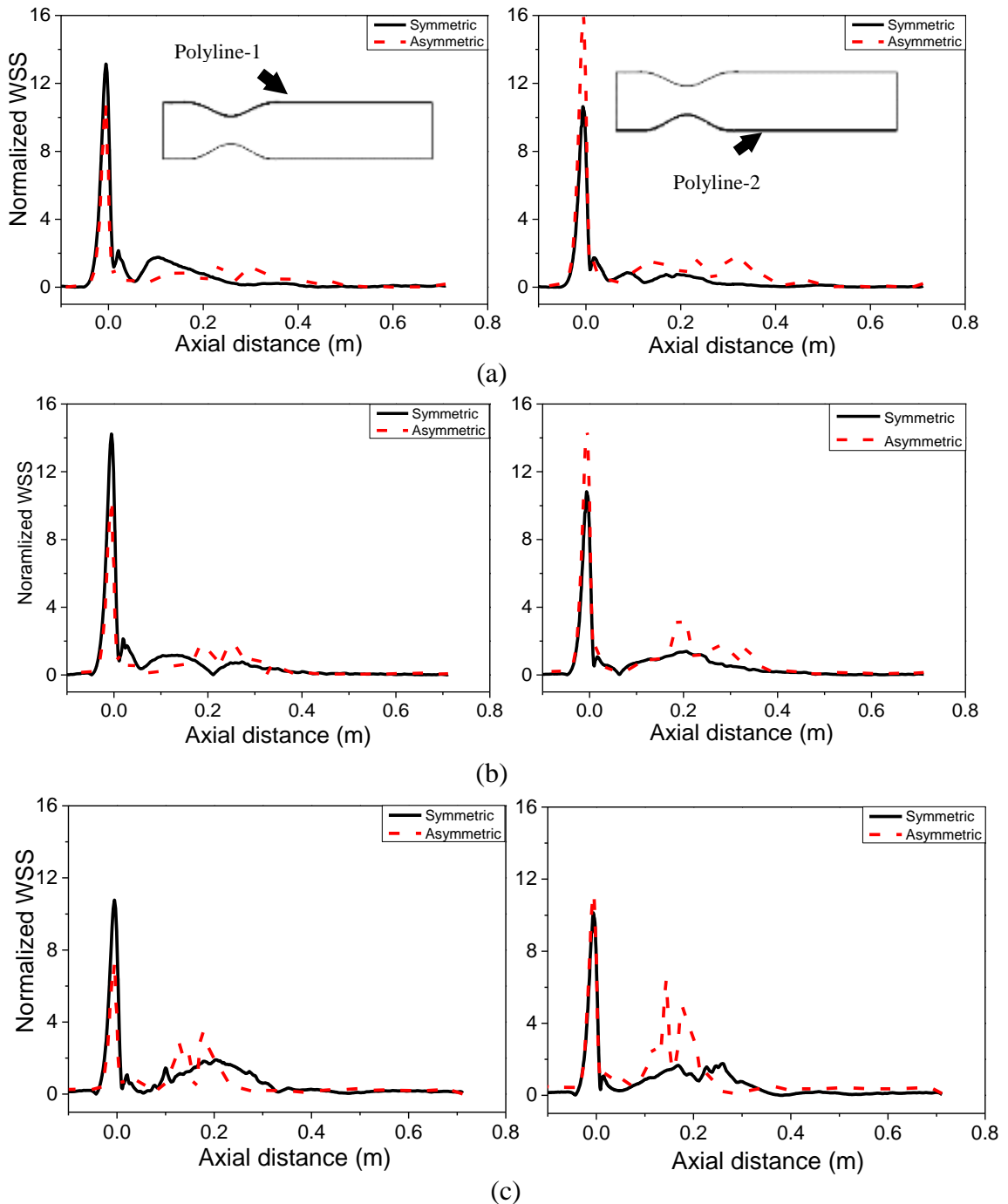


Figure 3.12. Spatial variation of wall shear stress at different womersley number (a) $\alpha = 7.5$ (b) $\alpha = 9$ and (c) $\alpha = 12$.

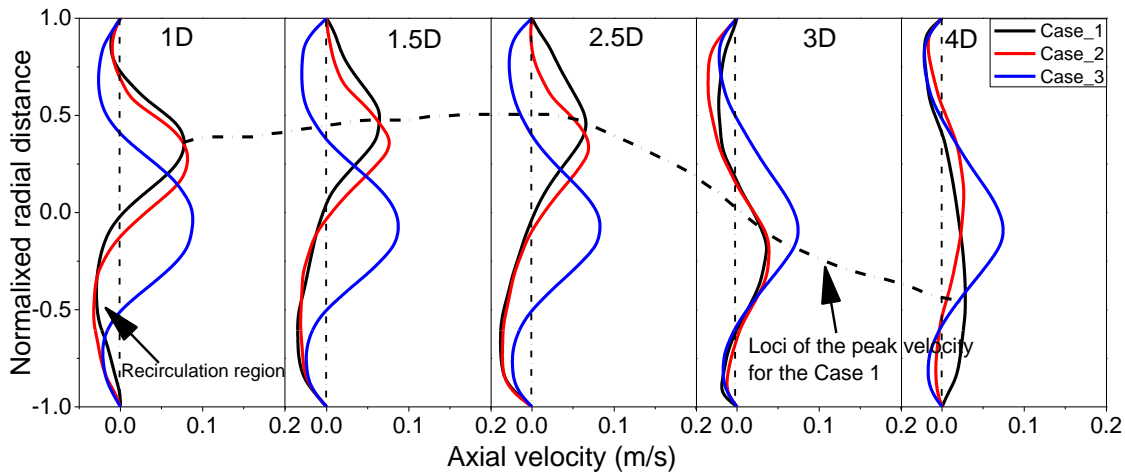


Figure 3.13. Comparison of stream wise velocity profile with different stenosis circularity at deceleration time step (T_3) for $\alpha=7.5$.

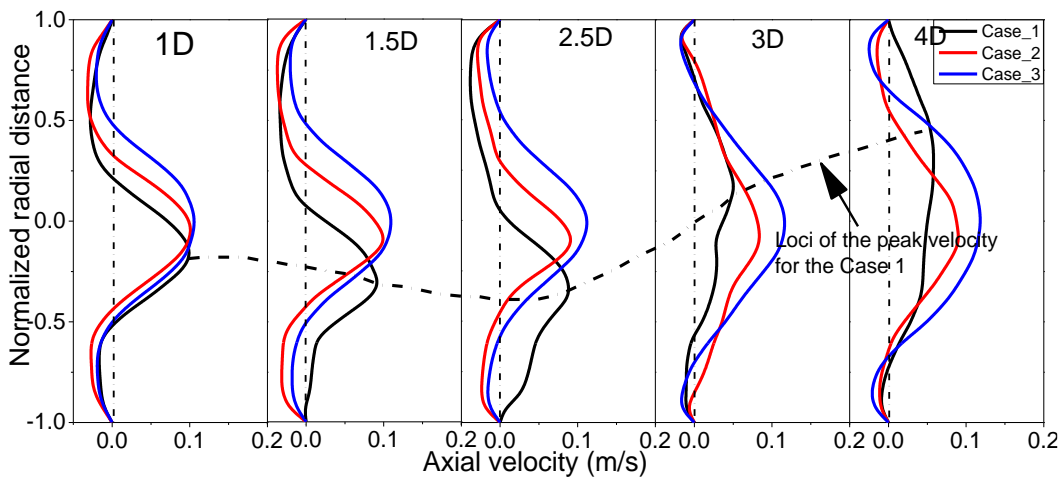


Figure 3.14. Comparison of stream wise velocity profile with different stenosis circularity at deceleration time step (T_3) for $\alpha = 12$.

For Case- 1 (where the circularity is minimum) the peak velocity does not appear at the center, rather it is offset at some radial distance. As the flow moves along the downstream side, the jet moves down to the bottom wall. Similar observations are made at higher pulse flow rate also (Figure 3.14). At higher Womersley number, the jet movement is more rapid. The loci of the peak velocity for Case 1 stenosis profile is show in Figure 3.13 and Figure 3.14. As the stenosed lumen becomes closer to a circular profile (Case-3) the velocity profile is less undisturbed in the downstream side. Significant amount of reverse flow is observed when the stenosis cross section moves away from a circular profile. This flow reversal is major factor which pushes the peak

velocity to one side of the tube in Case-1 profile.

3.6.2 Particle residence time analysis

The particle residence time (PRT) analysis shows that Case 1 & 2 have higher value of PRT than Case 3 (Figure 3.15), evidently due to the increased separation and reverse flow. As the lumen becomes closer to circular profile the flow becomes has more symmetric with a lower flow separation. As a result, Case 3 exhibits a lower PRT value. With change of physiological state (Womersley number from $\alpha=7.5$ to 12), the average PRT value in the domain decreases.

For better understanding the particle trajectory of one single particle (the one with maximum PRT) is selected and shown in Figure 3.16. The axial position and velocity of the particle is identified. The residence time is shown in the third axis. Even though the particles undergo severe swirling motion at higher Womersley number the residence time is much shorter. The axial distance zero corresponds to the center of the stenosis and looping of the particle happens in the post stenosis region.

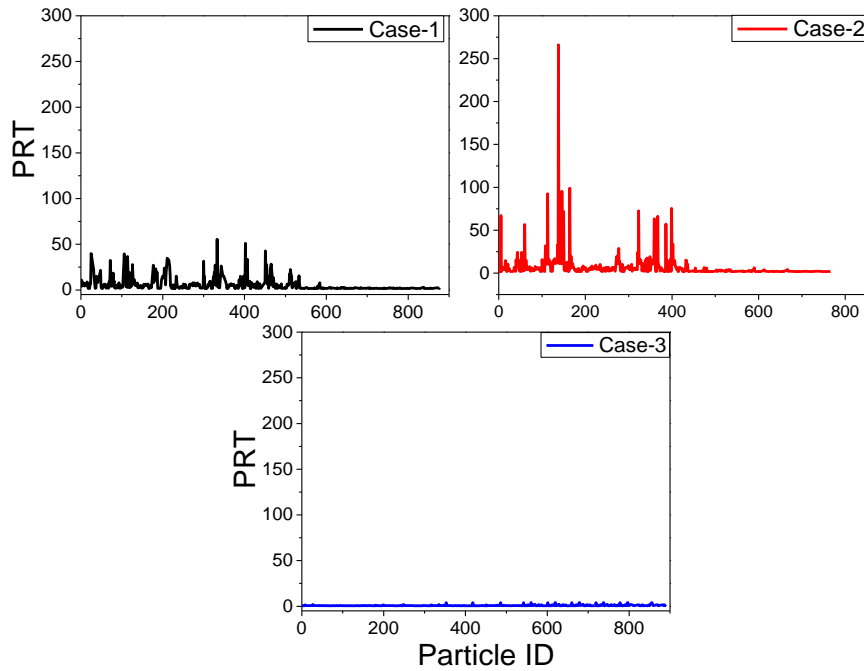
3.7 Effect of wall displacement: Fluid structure interaction studies

Fluid-structure interaction (FSI) problems are those that involve the coupling of fluid and structural mechanics. In FSI problem, the stresses and deformations of a given structure are computed simultaneously with the flow parameters that surrounds the structure. The deformations of the solid structure are due to the pressure gradients of the fluid, and likewise the pressure and velocities depend upon the deformation of the structure.

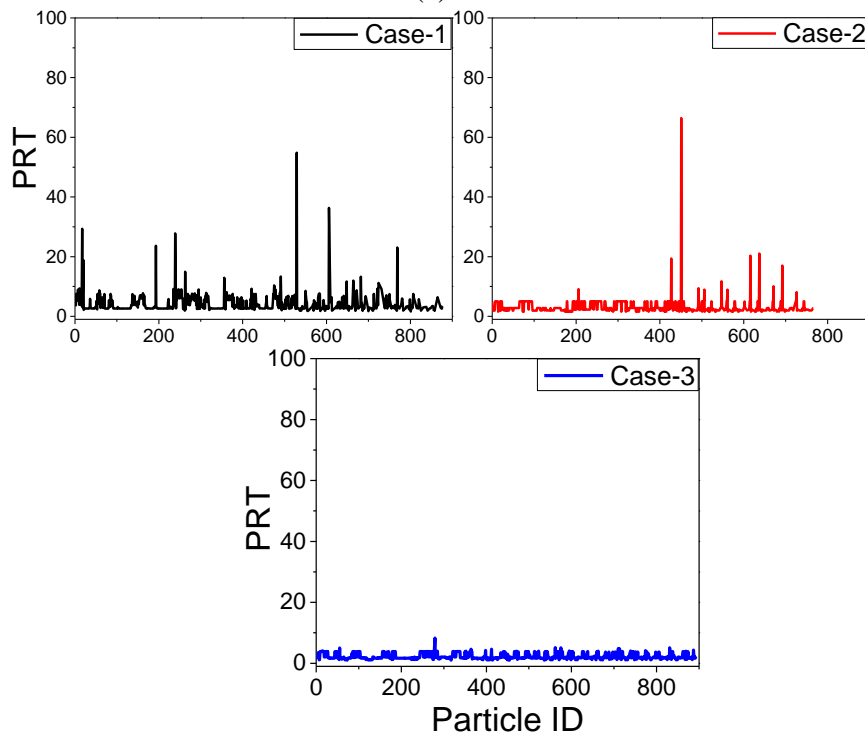
3.7.1 Modelling of the physical system

Stenosis nature is one of the most important parameter affecting on the flow and wall behaviors. Present study has chosen severe case of stenosis with 75% area reduction for the symmetric and asymmetric stenosis models (15% eccentricity). The objective is to understand the effect of pulse frequency on the hemodynamics of a stenosed flexible arterial wall. Previous simulations are carried out with rigid wall assumption. For FSI simulations the same symmetric and asymmetric models have been selected and a uniform thickness of 5mm has been added (Figure 3.17). Fluid and solid domain

models are constructed using 3D modeling software. Fluid meshing has been carried out with ANSYS FLUENT workbench and solid meshing in the APDL workbench for the finite element analysis.



(a)



(b)

Figure 3.15. Particle residence time under different physiological state (a) $\alpha = 7.5$ (b) $\alpha = 12$.

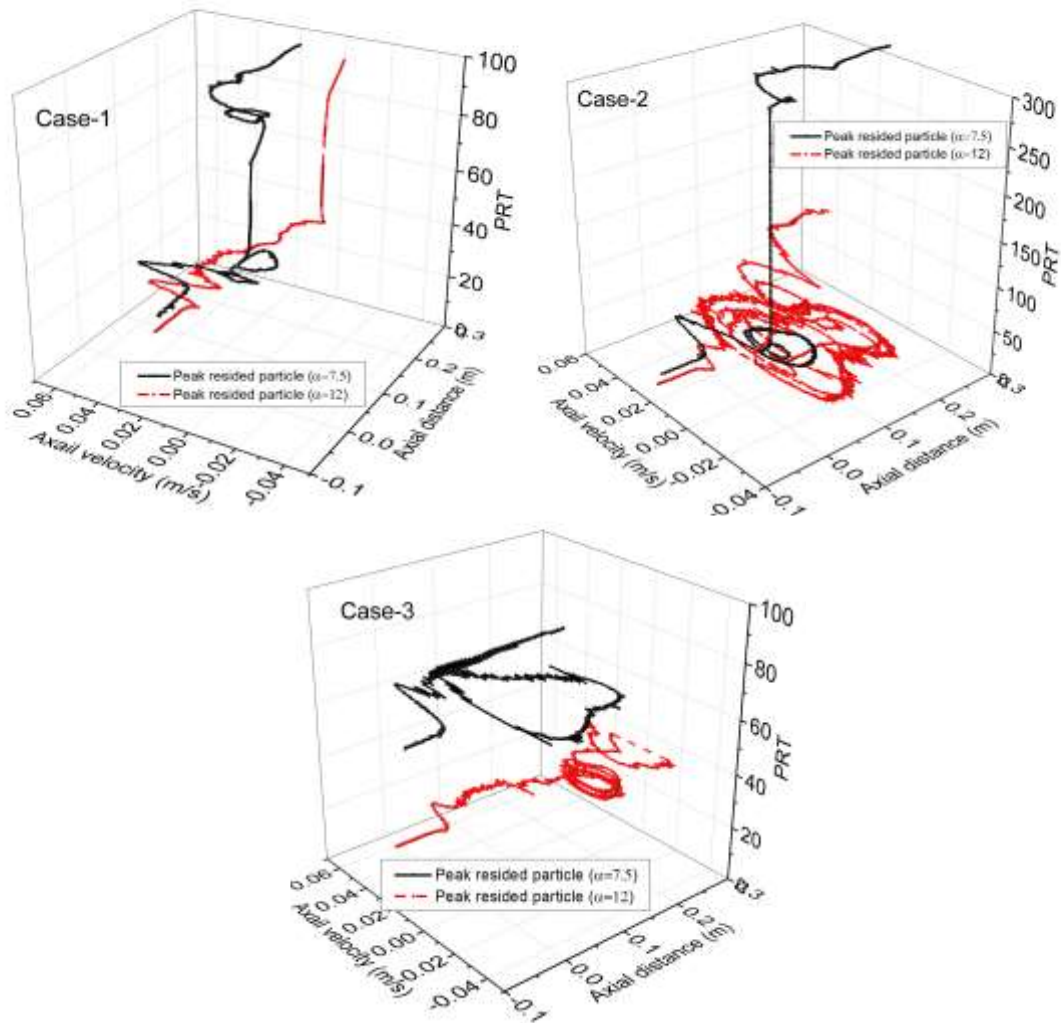


Figure 3.16. Spatial variation of peak resided particle behavior showed with axial velocity and particle residence time.

3.7.2 Fluid modelling

For solving time averaged Navier-Stokes equation Semi Implicit Method for Pressure Linked Equations Consistence (SIMPLEC) algorithm has been used (Li et al. 2007). Second order upwinding scheme is used for the momentum equations. The turbulence modeling and the values of turbulent intensity and length scale remains same as detailed in section 3.2.1. Similarly, the inlet waveform and the fluid properties are also kept similar to the previous analysis.

3.7.3 Solid modelling

The coupled FSI solid (wall) models are solved by Finite Element Method using ANSYS Mechanical APDL. Nonlinear incremental iterative procedures are used to

handle fluid structure interactions. Governing finite element equations of solid models are solved by Newton Raphson method (solution process continues till the solution reach steady state). In the present study, artery wall and stenosis parts are assumed as isotropic, elastic, homogeneous and incompressible. Different material properties can be assigned to each volume (part) to reflect the complexity (Healthy and diseased). For a healthy arterial wall young's modulus (E) of 0.4MPa and Poissons ratio of 0.499 are selected (Baldeusing et al. 2004). Stiffness is present in the stenosed region (diseased) hence diseased part chosen to be four times of the healthy part with a young's modulus of 1.6MPa (Li et al., 2007). The diseased model arteries are stretched axially and pressurized (Kanyanta et al. 2009). Current simulations have been carried out with an axial stretch ratio of 1.5. At each time step fluid and solid models solved individually using updated solution provided by the other part (two way coupling).

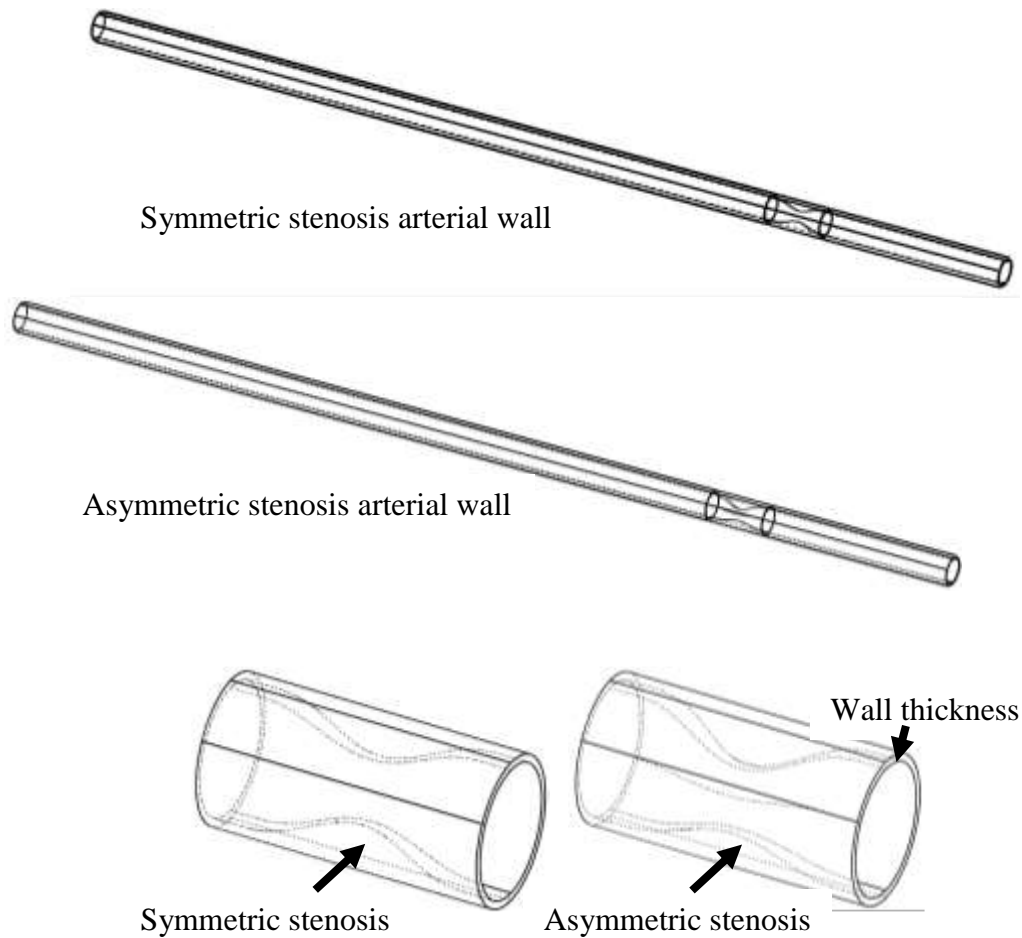


Figure 3.17. Symmetric and asymmetric stenosis arterial wall.

The governing equations for the solid-fluid coupling are (Jahangiri et al. 2017)

$$d_f = d_s : \text{Displacement}$$

$$n \cdot \sigma_f = n \cdot \sigma_s : \text{Traction}$$

where d , n and σ are displacement vector, normal vector and stress vector, subscripts f and s - stands for fluid and solid part respectively. The governing equation of the solid domain can be expressed as

$$\rho_s \ddot{d}_s = \nabla \cdot \sigma_s + \rho_s f_s \quad (3.13)$$

where d_s is the wall displacement vector, f_s is the volume force vector, σ_s is the Cauchy stress tensor and ρ_s is the wall density.

$$\sigma_s = \begin{bmatrix} \sigma_{xx} & \tau_{xy} & \tau_{xz} \\ \tau_{xy} & \sigma_{yy} & \tau_{yz} \\ \tau_{xz} & \tau_{yz} & \sigma_{zz} \end{bmatrix}$$

Stress – Strain relationship can be expressed as

The stress is related to the strain by (limited to linear materials).

$$\{\sigma\} = [D]\{\varepsilon\} \quad (3.14)$$

σ is the stress vector and it can be expressed as $\{\sigma_{xx} \ \sigma_{yy} \ \sigma_{zz} \ \tau_{xy} \ \tau_{yz} \ \tau_{zx}\}^T$, ε is the strain vector and it can be expressed as $\{\varepsilon_{xx} \ \varepsilon_{yy} \ \varepsilon_{zz} \ \gamma_{xy} \ \gamma_{yz} \ \gamma_{zx}\}^T$, D is the stiffness matrix.

3.7.4 Coupling

Fluid structure interaction algorithm uses the solution of coupled equations, governing the fluid and solid motions. Hence, inclusion of FSI effects would add significant complications in numerical simulation. Fluid motion is coupled with the displacement of the vessel wall and vice-versa. Hence, unsteady problems become significantly more complex than steady state problems. Steady state problem involve one way coupling between fluid and the adjacent wall (structure). Which means, the displacement of the structure is affected by fluid flow field but the fluid flow field is not affect by structural field. In two way coupling fluid flow field is influenced by the wall displacement, which calls for additional computational cost.

In two way coupling fluid and solid models are solved simultaneously with information transferring between the two models through fluid solid interface (Figure 3.18). Which

means, the fluid models are solved by latest displacement provided by the solid part of the previous time step. Then the obtained/solved loading conditions from the fluid model will be the boundary conditions to the solid model. Sequence will be repeated until the final step. Simulations are carried out till the solution meets the convergence criteria and the results of the final cardiac cycle has been used for the post processing analysis. During the cardiac cycle, at each nodal point distribution of stress, strain and displacements are analyzed in the post processing.

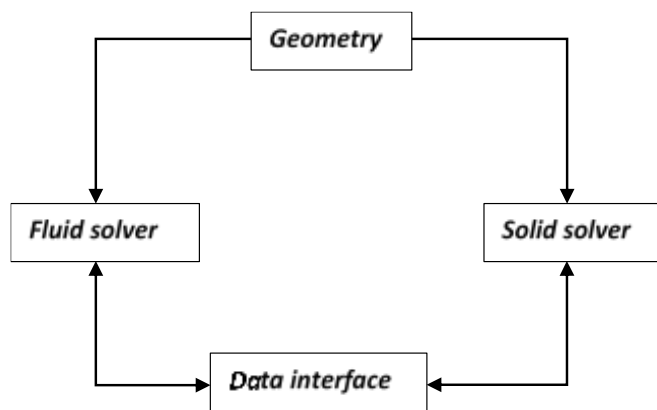


Figure 3.18. Two-way coupling block diagram for Fluid Structure Interaction analysis.

3.7.5 Validation study for fluid structure interaction

Apart from the validation study mentioned in the section 3.4 separate studies have been undertaken to validate the FSI problem. In the present study, numerical FSI results are validated with results of Li et al. (2007) for a 70% stenosed model under pulsatile flow. Comparisons are made for the flow shear, pressure drop, velocity at the throat and wall displacement. Figure 3.19 shows the wall shear stress (WSS) variation during a pulse cycle at one diameter proximal to the stenosis (-1D) and at throat of the stenosis. In both cases, the present simulation matches well with the Li et al. (2007). Table 3.3 compares the absolute value of WSS, velocity pressure drop at the throat and radial wall displacement. The deviations of results obtained through present simulations are quite small in comparison with the results of Li et al. (2007) which ensures the validity of the present numerical procedure.

Table 3.3 Comparison of results with Li et al (2007).

During peak time step (symmetric stenosis with 70% area reduction)	<i>Li et al., 2007</i>	<i>Present study</i>
WSS (Pa) at throat	230	198
Velocity (m/s) at throat	3.2	3.13
Pressure drop from inlet to throat (KPa)	5.3	5.229
Radial wall displacement (μm) at peak time step	205	196

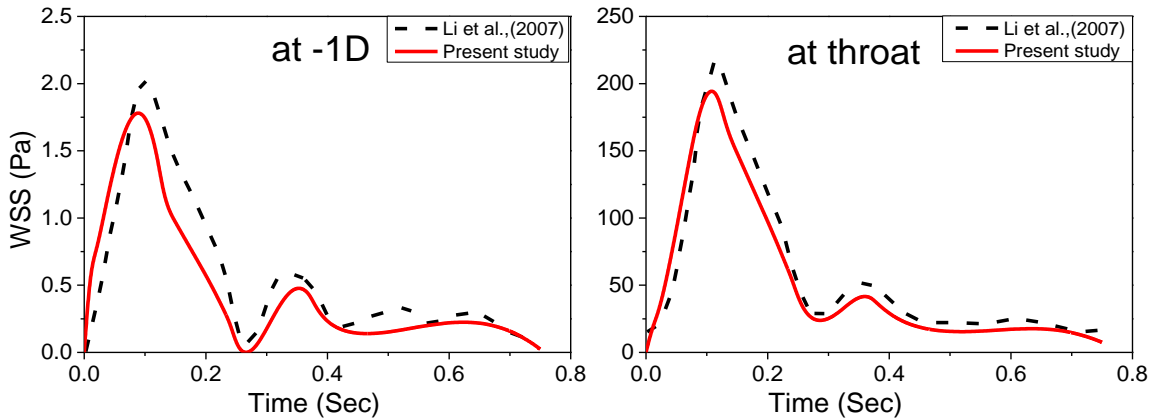


Figure 3.19. Comparison of Wall Shear Stress results with Li et al., 2007 (a) One diameter proximal to the stenosis (-1D) and (b) at throat of the stenosis.

3.7.6 Behavior of pulsatile flow through the flexible artery

Structural simulation results such as von mises stress and displacements are analyzed and the corresponding time averaged results are derived. Von mises stress is used to express yield/rupture criterion in this study. These criteria predict that material (ductile) starts yielding when von mises stress reaches a maximum value, called as yield strength. It is calculated by using all the three principal stresses (3D models) and it can be expressed as

$$\text{Von mises stress} = \sqrt{\frac{(\sigma_1 - \sigma_2)^2 + (\sigma_2 - \sigma_3)^2 + (\sigma_3 - \sigma_1)^2}{2}} \quad (3.15)$$

where σ_1 , σ_2 , and σ_3 are three principal stresses.

Figure 3.20 shows stress distribution on the stenosed arterial wall during peak cardiac time step. Maximum stress is found in the asymmetric stenosis model, particularly on the thinner wall side. A comparison of von mises stress and radial wall displacement has been made between symmetric and asymmetric stenosed models at different locations on the upper wall. The values from these locations are time averaged over one cardiac cycle and their percentage deviations (of asymmetric model with respect to symmetric stenosis) are shown as a bar chart in Figure 3.21. The wall displacement is 50% more than symmetric case. With increase of pulse rate (Womersley number) the stress distribution on the arterial wall as well as the wall displacement increases. Due to the presence of larger curvature (thick wall) on one side, flow is pushed to one side of the arterial wall leading to higher stress in the asymmetric stenosis. This makes the plaque undergo higher compressive force. During the cardiac cycle increase of mechanical stresses at one side of the wall undergo can cause early rupture. The larger displacement of wall in the asymmetric case enhances flow separation in the post stenosis, which provides a hotspot for the adhesion of new cells than symmetric case.

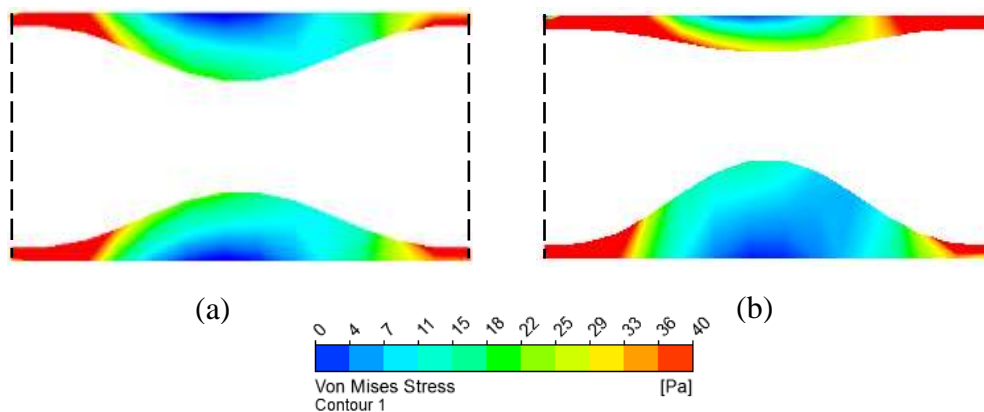


Figure 3.20. Distribution of stress on the stenosis arterial wall during systolic peak time instance (a) symmetric and (b) asymmetric stenosed arterial wall.

Figure 3.22 and Figure 3.23 compares few critical fluid dynamic parameters to estimate the effect of rigid wall assumption on the simulations. The wall shear stress and the velocity are compared at the stenosis region over a cycle. The deviations are found to be very marginal. Detailed comparison is made with velocity contours on two orthogonal axial planes and the obtained results from the two analysis (rigid and elastic wall) reveals no significant difference in the flow pattern. This observation is in accordance with studies carried out by Bonfanti et al. (2018) wherein the rigid wall

assumption reflected similar results of elastic wall assumption during the hemodynamic analysis.

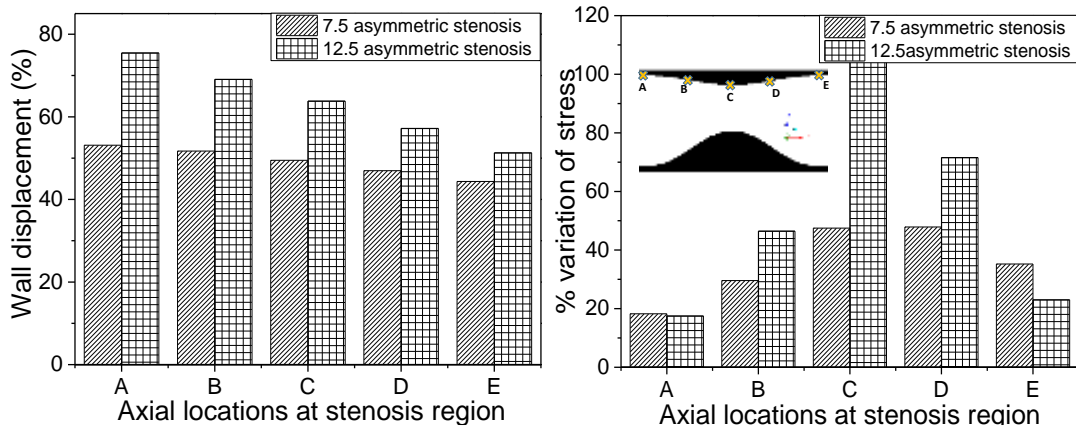


Figure 3.21. Comparison of a time averaged Vonmises stress and wall displacement between symmetric and asymmetric stenosis at different womersley number.

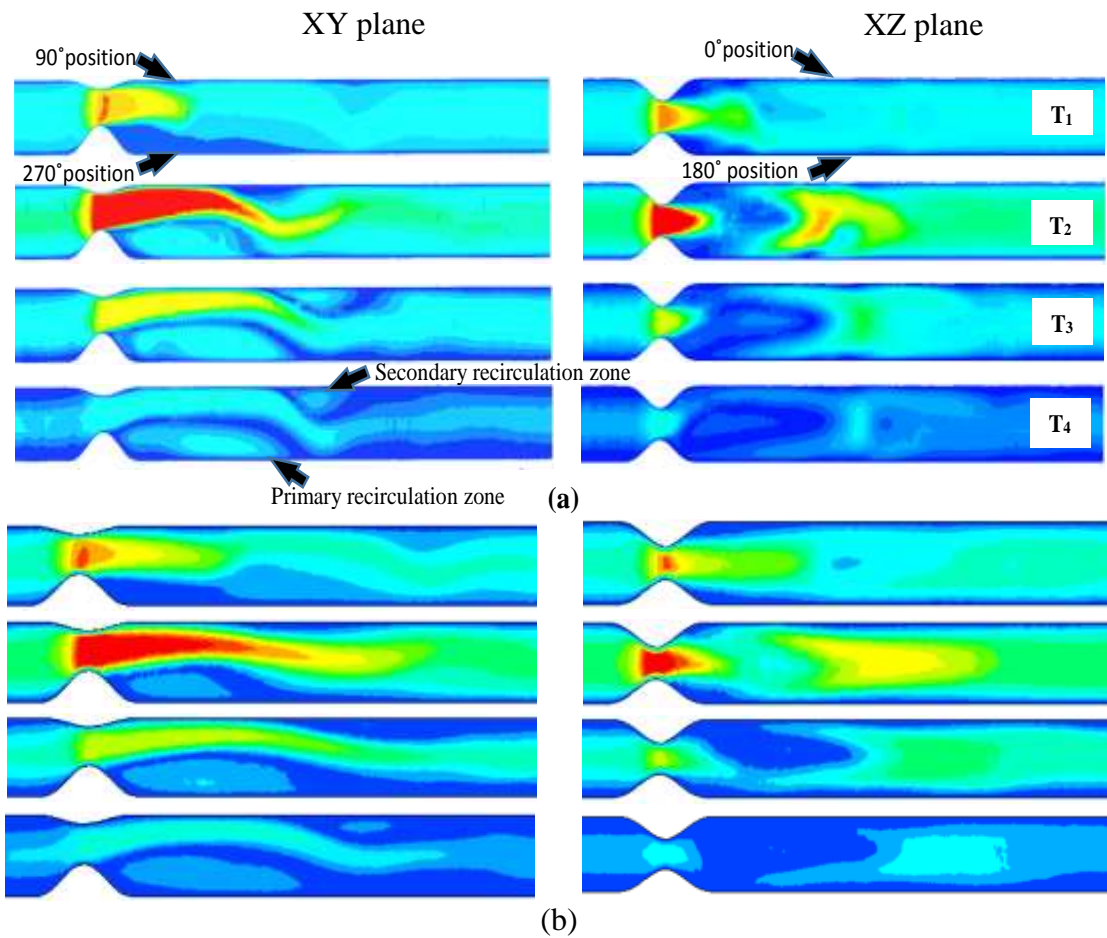


Figure 3.22. Velocity contours for asymmetric stenosis model at $\alpha = 7.5$ (a) Rigid wall (b) flexible wall.

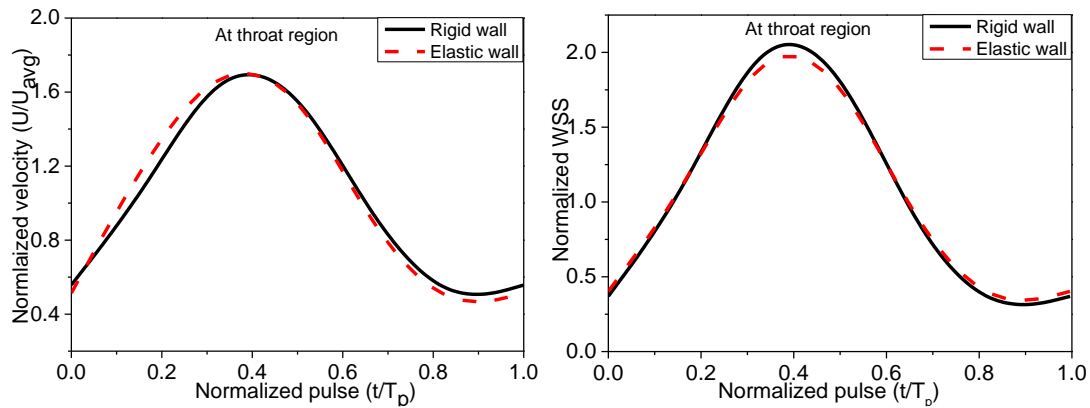


Figure 3.23. Velocity and wall shear stress comparison made between asymmetric stenosis simulation with rigid and flexible wall assumption.

3.8 Summary of the chapter

Computational studies carried out straight idealized stenosed artery yields the following major results.

- Helicity in the post-stenotic region can be considered as an indicator for the progression of the atherosclerosis, as it directly influences the particle residence time (*PRT*) at that region.
- The asymmetric stenosis model exhibits less helical flow structure than the symmetric stenosis model. The vortical structures or the flow disturbances are not getting transported to the downstream side of the flow, which decreases the mass transport near to the arterial wall and triggers further occlusion/plaque build-up at the post-stenotic region.
- Symmetric stenosis induces more helicity in the flow structure and hence the chances of occlusion of new cells on the arterial wall are minimal. The average residence time (mean *PRT*) for the symmetric stenosis model decreases with the Womersley number due to the increased helicity.
- The mean *PRT* value increases with the Womersley number for asymmetric model. More number of localized vortices are found in the asymmetric stenosed model.

- Vortices formed in the post-stenotic regions are not getting transported in the asymmetric model. The formation of secondary vortices in asymmetric model leads to severe undulations in the WSS distribution distal to the stenosis throat region.
- Patients with complex circularity in the stenotic region may have further chances of plaque deposition due to swaying motion of stenotic jet in the downstream cause for the secondary vortices.
- Due to the presence of larger curvature (thick wall) on one side, flow is pushed to one side of the arterial wall leading to higher stress and wall displacement in the asymmetric stenosis.
- Comparisons of velocity contour made between the rigid wall and flexible wall artery models yields almost similar results. Deviations are found to be very marginal, hence for simulations in medium and large sized arteries rigid wall assumption is quite valid.

4 STUDIES ON BIFURCATED ARTERY WITH SWIRL GENERATOR

Having understood the influence of helicity in the particle residence time in the previous chapter, the study has been extended to bifurcated arteries and is presented in this chapter. A significant proportion of cerebral stroke is a consequence of the arterial stenotic plaque rupture causing local thrombosis or distal embolization in the carotid bifurcated artery. The atherosclerotic plaque in the carotid arteries most commonly forms near the bifurcation zone and curved regions of the vessel. These locations are vulnerable to high flow disturbances leading to low wall shear stress (WSS) suggesting that blood fluid dynamics (hemodynamics) has an important role in deciding the formation and development of the atherosclerotic plaques. The secondary flows generated at the bifurcation zone promotes the deposition of atherogenic particles on the outer walls. Presence of swirl/helical flow can suppress the localization degenerative materials that may cause plaque.

The present study aims at understanding the pulsating flow through different bifurcation geometries and devise a mechanism to suppress the development of atherosclerosis plaque by inducing helical flow structure in the arterial passage. To realize this objective a novel swirl generator (stent like structure with an internal groove) has been developed to induce helicity in the bifurcated passage. The functional requirement of the swirl generator is to minimize the relative residence time (RRT) of the fluid layer near the endothelial wall without generating any additional pressure drop.

4.1 Computational Model

The common carotid artery (CCA) bifurcates in to internal carotid artery (ICA) and external carotid artery (ECA). Figure 4.1 shows a schematic representation of atherosclerotic plaques formation at carotid artery bifurcation region. Present numerical study has been carried out on a population-based healthy idealized bifurcated geometry similar to the carotid artery. Such an idealized model-based approach will enable to carry out a more rigorous systematic study, by varying one specific geometrical feature at a time while keeping the others constant. This enables to identify if and to which extent anatomic features promote atheroprotective or atherosusceptible hemodynamic

phenotypes (Chiastra et al. 2017). The vessel geometry and the diameter ratio specifications are taken from the works by Ku et al. (1985) and Schulz and Rothwell (2001). Chiastra et al. (2017) has demonstrated that the impacts of bifurcation angle on stenosed and unstenosed geometries are negligible. For the present study, a bifurcation angle (β) 25 deg. is selected for all the simulations.

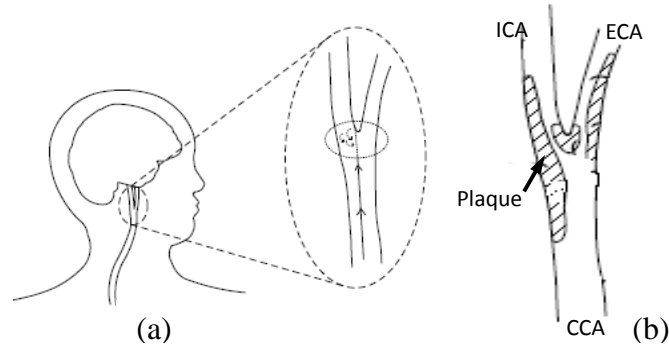


Figure 4.1. (a) Schematic representation of carotid artery in human body (b) Typical plaque formation in carotid artery.

As in the previous study (Chapter 3), here also blood is modelled as Newtonian fluid with density and dynamic viscosity of 1060 kg/m^3 and 0.0036014 Pa s respectively (Banks and Bressloff 2007, Mukherjee et al. 2016). Patient specific inflow boundary condition is used from healthy volunteers, which is similar to the wave form used by Hoi et al. (2010) and Gataulin et al. (2015) in their studies (Figure 4.2). Fabbri et al. (2014) suggested that constant pressure boundary condition would be safer to use for the bifurcated models, because of flow resistance/pressure drop will be similar in all branches. Hence, present study has used a constant pressure boundary condition at the outflow (Augusto et al. 2016, Gataulin et al. 2015). The boundary wall is assumed to be rigid and no slip condition is specified ((Balossino et al. 2009, Hasis et al. 2018, Lee and Steinman 2007, Linge et al. 2014, Morbiducci et al. 2011). CFD solver was customized through user defined functions. Number of iterations in the inner loop has been set to 30 with a time step size of 0.0001s. The convergence criterion for each time step is set by a residual criterion of 10^{-7} .

Direct numerical simulation (DNS) resolves all spatial and temporal scales of the flow, but the computational cost is too expensive. Use of complex geometries for the simulation is strongly limited due to the high order numerical schemes. The turbulence methodology adopted for this study is the Large Eddy Simulation (LES) (Germano et

al. 1991, Jabir and Lal 2016, Lilly 1992, Smagorinsky 1963). LES resolves the larger turbulent eddies whereas the smaller ones are modelled during the pulsatile flow (Lantz et al. 2016, Varghese et al. 2008). Computational cost of LES is comparatively lower than DNS. Whereas the classic Smagorinsky LES model is closer to DNS data (Varghese et al. 2007). Hence the present simulation has been carried out with LES Smagorinsky model. Very fine grids have been generated to each geometric model so that the maximum value for y^+ can be maintained smaller than 1. The computations are performed on a windows 64bit operating system with Dual processor (2 no.) INTEL XEON V3 8cores, 64GB RAM.

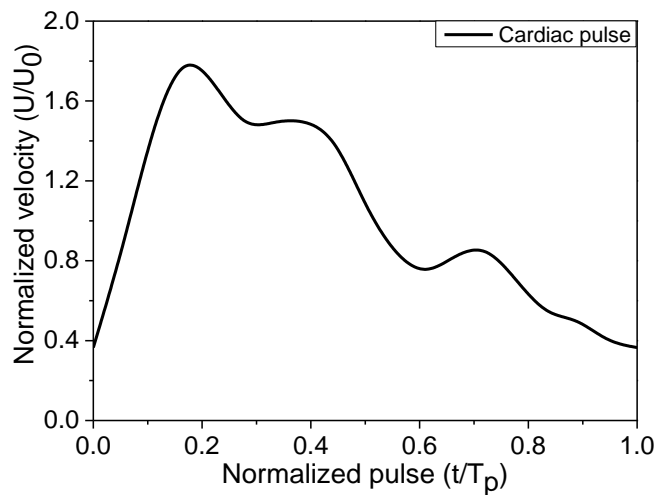


Figure 4.2. Patient specific inflow velocity profile (Hoi et al., 2010, Gataulin et al., 2014).

4.2 The swirl generator

This section details about the conceptual design of swirl generator which can generate helical flow structure in the bifurcated arteries. The swirl generator can be envisaged as a stent like device with internal grooves. The swirl generator must provide a helical flow to minimize the relative residence time of the fluid layer closer to the wall and at the same time it must not be creating significant pressure drop and additional fluid resistance in the arterial passage. With these criteria, the grooves are provided with triangular ribs at the inner wall of the swirl generator (Figure 4.3b). The parameters taken for analysis are height of the rib, the helical angle and the number of ribs Figure 4.4. Each of these parameters are varied systematically to understand their influence on

the hemodynamics and the atherogenesis. A total number of 11 different cases are analysed whose details are shown in Table 4.1. Figure 4.3a shows the idealized carotid artery model, chosen for the computational study. The common carotid artery (CCA) empties into a smaller external carotid artery (ECA) and a large internal carotid artery (ICA). The length of the helicity generator is three times the CCA diameter and it is placed five diameter distal ($-5D$) to the bifurcation zone (Figure 4.3a) in the CCA passage.

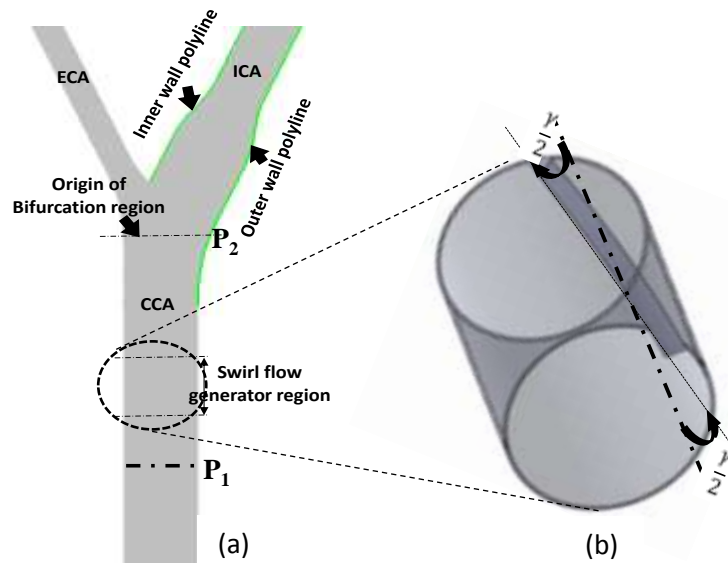
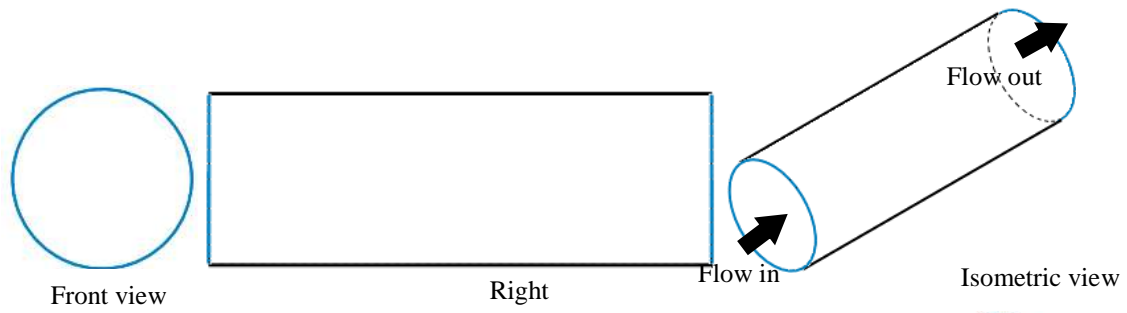


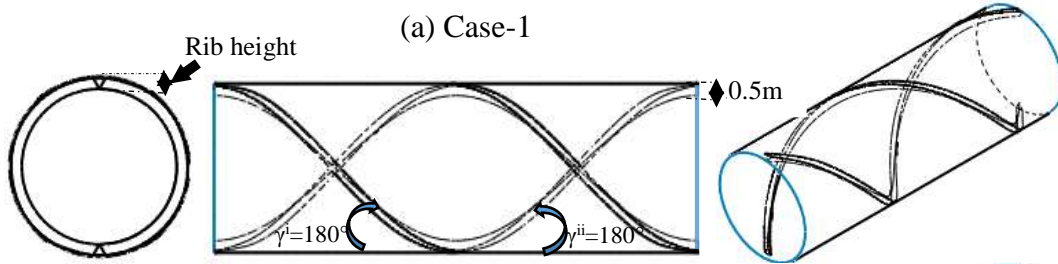
Figure 4.3. (a) Location of the swirl generator in the arterial passage (b) conceptual design of swirl generator, where ' γ ' is helical angle.

Table 4.1 Varied parameters during different model study.

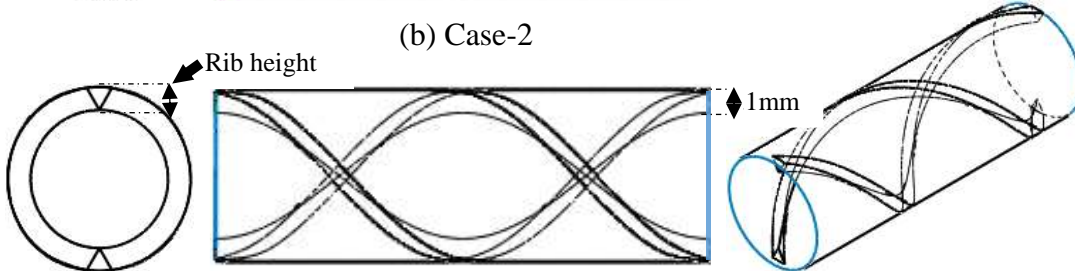
Models used for study	Rib Height (mm)	Helical angle (γ)	No. of ribs used
Case-1	0.5	360°	2
Case-2	1.0	360°	2
Case-3	1.5	360°	2
Case-4	2.0	360°	2
Case-5	1.5	45°	2
Case-6	1.5	90°	2
Case-7	1.5	180°	2
Case-8	1.5	270°	2
Case-9	1.5	360°	1
Case-10	1.5	360°	4
Base case	-	-	-



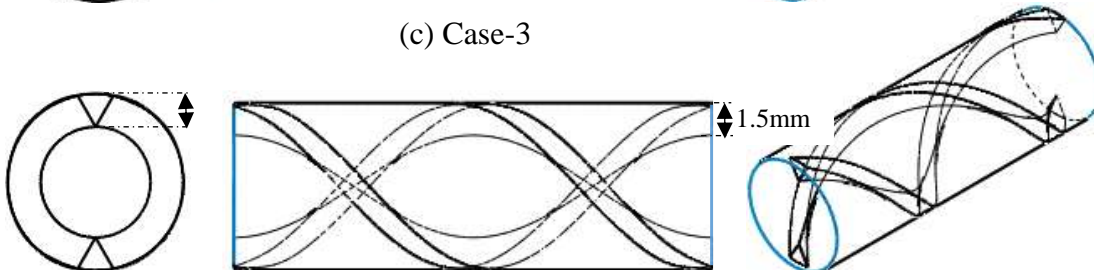
(a) Case-1



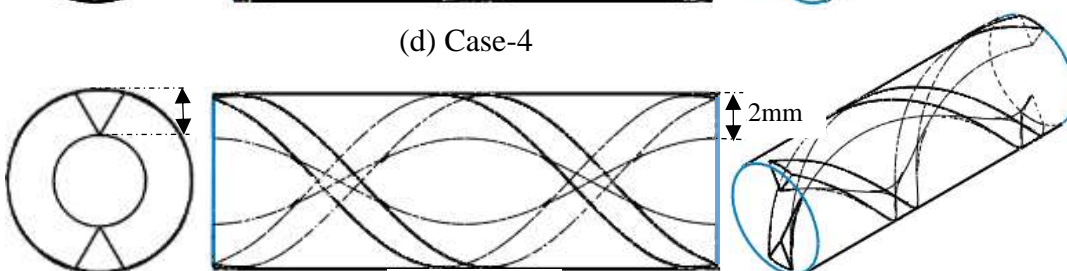
(b) Case-2



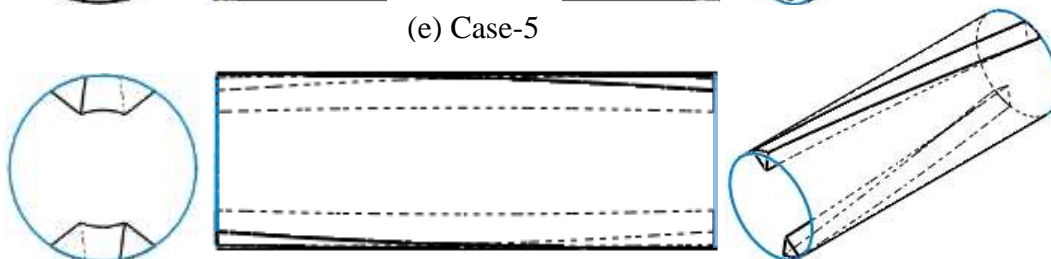
(c) Case-3



(d) Case-4



(e) Case-5



(f) Case-6

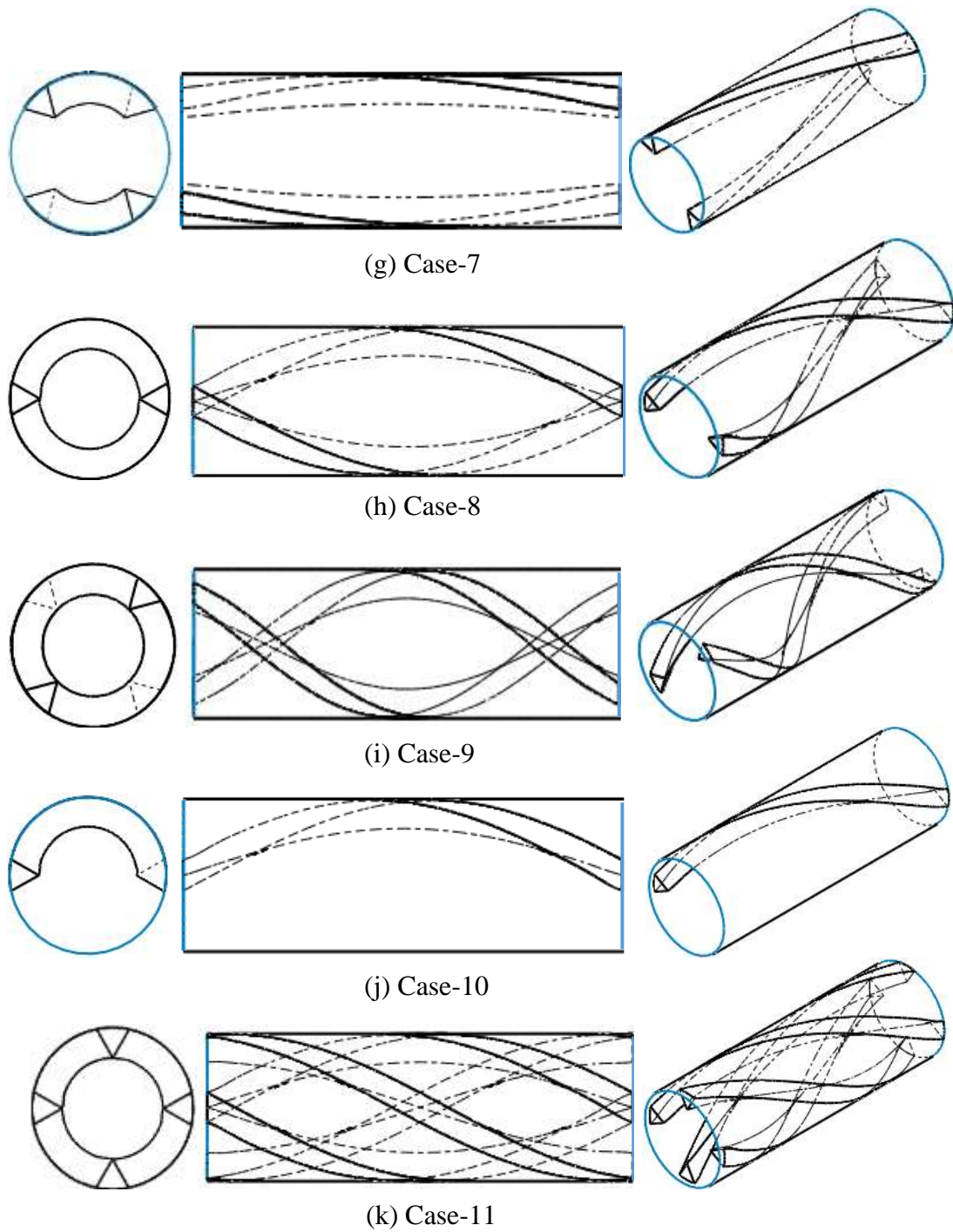


Figure 4.4. Three different views of all the tested cases.

4.3 Analysis of results

4.3.1 Relative residence time (RRT)

Spatial variation of WSS in the flow are derived from the velocity vectors. These vectors starts to oscillate with the unsteady flow and it changes its directions of low

WSS. Hence, low WSS and high OSI values do not always collocate (Fytanidis et al. 2014). To overcome this difficulty Himburg et al. (2004) has suggested the use of Relative Residence Time (RRT) with the correlation of OSI and Time Averaged WSS and is defined as

$$RRT = \frac{1}{(1-2*OSI)TAWSS} \quad (4.1)$$

$$OSI = 0.5 \left[1 - \frac{\left| \int_0^T \overline{WSS} \right|}{\int_0^T |\overline{WSS}|} \right] \quad (4.2)$$

$$TAWSS = \frac{1}{T} \left| \int_0^T \overline{WSS} \right| \quad (4.3)$$

where T is the pulse period, \overline{WSS} is the instantaneous wall shear stress.

The relative residence time (RRT) indicates the residence time of fluid layer at endothelium layer of wall (Himburg et al. 2004, Soulis et al. 2011). Friedman et al. (1981) and Ku et al. (1985) observed that oscillating nature of WSS causes changes in flow separation and sudden change of vortex structure. Flow visualization studies carried out by Ku and Giddens (1983) showed the attachment of separation bubbles near to the outer wall of sinus for a longer period of time, which enhances the fluid residence time. Hence, RRT can be used as an effective marker for indicting the probability of plaque formation through settlement of atherogenic materials.

4.3.2 Pressure loss in the bifurcated region

Static pressure drop in the artery is one of the most important parameter considered in the present study. An increase in the pressure drop indicates an increased flow resistance in the channel. Static pressure drop is calculated as the area average pressure difference between the inlet of swirl generator and at the bifurcation section. This is then time averaged over the entire cycle. An ideal swirl generator may be causing minimum time averaged static pressure drop.

4.3.3 Descriptors for swirl flow topology

Topology of helical flow structure in the bifurcated artery has been analysed with swirl flow strength and relative rotational direction. Following expressions are derived from Gallo et al. (2012).

$$h_1 = \frac{1}{TV} \int_T \int_V H dv dt \quad (4.4)$$

$$h_2 = \frac{1}{TV} \int_T \int_V |H| dv dt \quad (4.5)$$

$$h_3 = \frac{h_1}{h_2} \quad (4.6)$$

where ‘T’ is the cardiac pulse cycle, ‘V’ is the volume of fluid in domain, ‘H’ is the helicity and it can be expressed as $H = u \cdot \omega$. Where ‘U’ is the velocity and ‘ ω ’ is the vorticity of the fluid. To define the bulk flow parameter integration is carried out over time (T) and volume (V).

The term h_1 is helical intensity, which is integral measure of helical flow accounting for helicity sign changes. h_1 equals ‘0’ when there is no helical flow in the domain or it may have reflectional symmetric counter rotating helical structures. The parameter h_2 defines total amount of helical flow in the fluid domain, irrespective of direction. The term h_3 is a non-dimensional quantity ranging between -1 to +1. h_3 value equals -1 (+1) only when left-handed (right-handed) helical flow structures are present in the domain and it equals 0 in case of reflectional symmetry or no helical structures in the flow field.

4.4 Results

4.4.1 Effect of swirl generator on the hemodynamics

The time averaged relative residence time at the bifurcation zone, time averaged pressure drop across the CCA and the helicity descriptor h_2 are calculated for all the designs. Table 4.2 gives a comprehensive view for all these parameters for each design as well as their percentage deviation compared to the base case. As the objective of this swirl generator is to reduce the *RRT* near the bifurcated channels, design with least *RRT* (i.e. Case 3) may be the best selection. However, it causes a pressure drop of 110.5 Pa which is 107% more than the base case. The swirl generator must create minimum blockage and fluid resistance to the flow while minimizing the *RRT*. Owing to this condition, Case 9 stands out as the best choice as it does not generate any additional pressure drop compared to the base case, while bringing down the *RRT* by 36%.

4.4.2 Relative residence time (RRT) analysis

Figure 4.5 shows the relative residence time of ten swirl generator designs in

comparison with the base case. The RRT has been plotted on the outer wall of the ICA as major separated region are centered here. The two peaks observed in the RRT plots, correspond to two stagnation points formed within the recirculation regions. The introduction of swirl generator reduces RRT of each design at varying magnitude. The effect of rib height on RRT is visible from the comparison of Cases 1 – 4. With increase in the rib height the two stagnation points comes closer and with a rib height of 2 mm the second stagnation point almost disappears (Case 4). However, the smallest value of RRT is observed for a rib height of 1.5 mm (Case 3). Compared to base case, in Case 3 the point of separation is delayed due to the enhanced helicity in the passage. The separated region is shrinked and the recirculation zone is also reduced (Figure 4.5). Further increase in the rib height (i.e. beyond 1.5 mm) seems to be not yielding any appreciable reduction in the RRT values. On the contrary the RRT value at the first stagnation point starts increasing further, whereas the secondary stagnation point vanishes due to increased helicity in the passage.

Cases 5 – 8 depicts the variation of RRT with the helical angle of the rib. A large helical angle induces more helicity to the flow. However, the RRT values need not be always come down with the helicity induced. This is evident with the comparison between Case 7 and Case 8. With an increase in helical angle from $\gamma = 180$ deg. (Case 7) to $\gamma = 270$ deg. (Case 8) the helicity induced increases by 20% but the RRT value also increases from 4.8 to 6.5. The residence time again comes down to 4.7 when the helical angle is increased to 360 deg. (Case 3). The reasons for this unforeseen behaviour may be explained with helicity contours plotted at two cross sections near the bifurcation zone (Figure 4.6). These are instantaneous values of helicity plotted at deceleration time step. For a helical angle of 270 deg. the flow streamlines gets modified in such a way that the helicity contours (both clockwise spin and anticlockwise spin) are moved away from the outer wall of the ICA. The outer wall of the ICA is seen mostly with zero helicity and is characterized by strong local recirculation and low WSS which will enhance the residence time of fluid near the wall. This implies that even though the volumetric average of helicity (h_2) increases with helical angle the same may not reflect in the RRT which is basically a function of the local values of helicity.

Table 4.2 Comparison of swirl generator designs with base case.

Models	Rib height (mm)	Helical angle (degree)	No. of helical Ribs in the flow domain	Time average pressure difference (Pa)	Pressure drop, % deviation compared with Base case	Average Relative Residence Time	RRT, % difference compared with Base case	Helicity intensity (h_2)
Base case	-	-	-	53.1	-	13.9	-	126.1
Case-1	0.5	360	2	57.5	8.29	10.9	21.58	176.6
Case-2	1	360	2	77.1	41.74	9.1	34.53	231.2
Case-3	1.5	360	2	110.5	74.45	4.7	66.19	294.0
Case-4	2	360	2	136.8	75.75	7.2	48.20	360.0
Case-5	1.5	45	2	66.2	9.58	11.3	18.71	167.0
Case-6	1.5	90	2	68.8	23.72	7.8	43.88	177.9
Case-7	1.5	180	2	72.2	27.76	4.8	65.47	214.5
Case-8	1.5	270	2	92.3	54.29	6.5	53.24	259.1
Case-9	1.5	180	1	53.48	0.41	8.9	35.97	191.5
Case-10	1.5	180	4	94.1	75.53	8.0	42.45	254.9

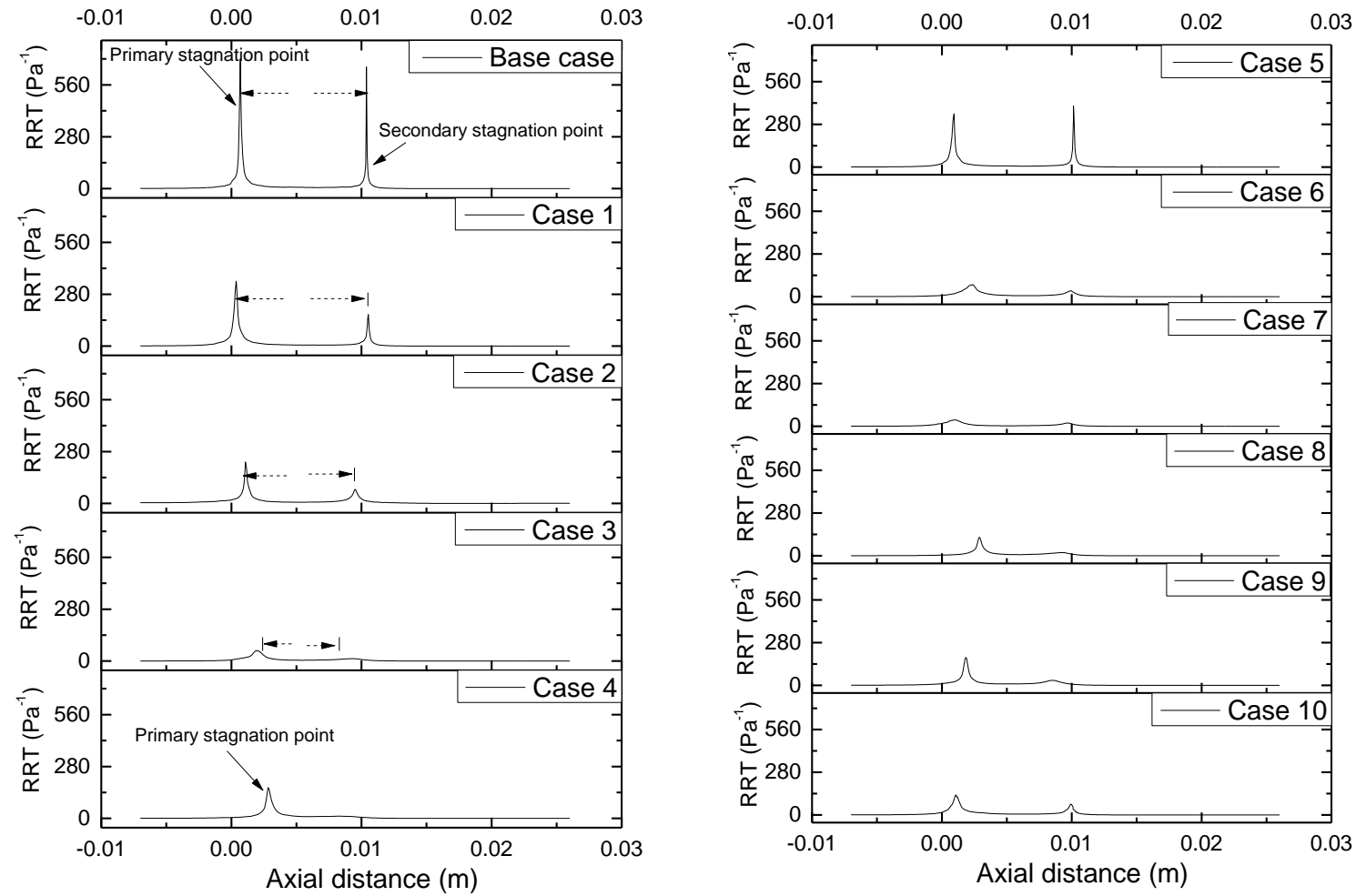


Figure 4.5. Relative residence time of fluid layers near the ICA outer wall compared with Base case.

The number of ribs is another important parameter which can influence the helicity generated and the RRT. A helical angle of 180 deg. and a rib height of 1.5 mm is selected as the optimum choice based on the smaller relative residence time. Hence fixing these configurations the number of ribs are varied and the simulations are carried out. Comparing the Cases 7, 9 and 10 it turns out that, single rib configuration produce least flow resistance. The pressure drop generated by Case 9 is similar to that of base case while reducing the RRT by 36%. Increase in the rib height from 1.5 mm to 2mm enhance the turbulence which results in more resistance to the fluid flow. As a result, the pressure drop increases roughly by 24% with a small increment of rib height.

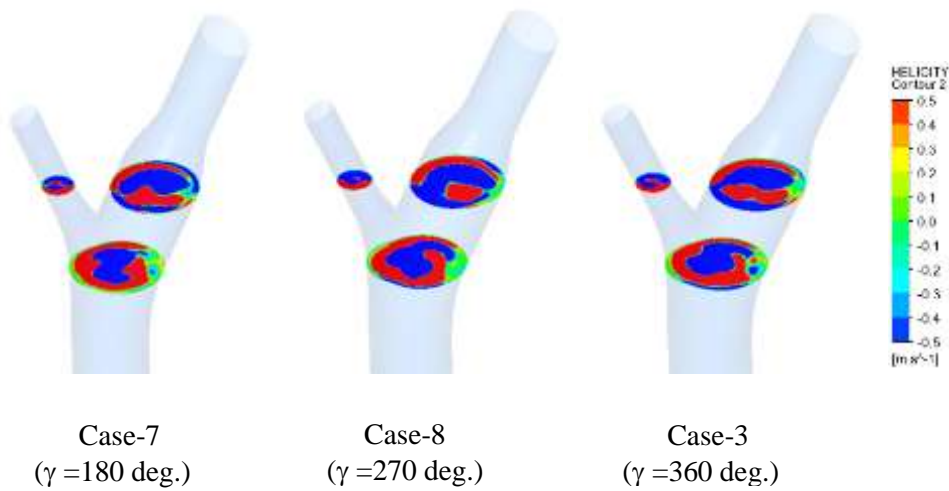


Figure 4.6. Helicity contours for different helical angles at the bifurcation region during diastolic deceleration time step.

4.4.3 Detailed analysis on the flow modifications

Velocity contours at the central axial plane has been plotted and shown in Figure 4.7. The primary and secondary stagnation point which are responsible for two peaks in the RRT plot has been demarcated in this figure. As a result of the helical movement, the kinetic energy has been redistributed from the centre of the arterial passage to the periphery. This helps in mitigating the recirculation regions near the bifurcation passage. The velocity vectors at the bifurcation section is shown in Figure 4.7 for different rib heights. As the rib height increases it induces more helicity and the primary stagnation point moves proximal to the bifurcation region. The effective flow area also increases in the sinus region due to the increased helicity. Similar observations are made with increasing the number of ribs in the passage.

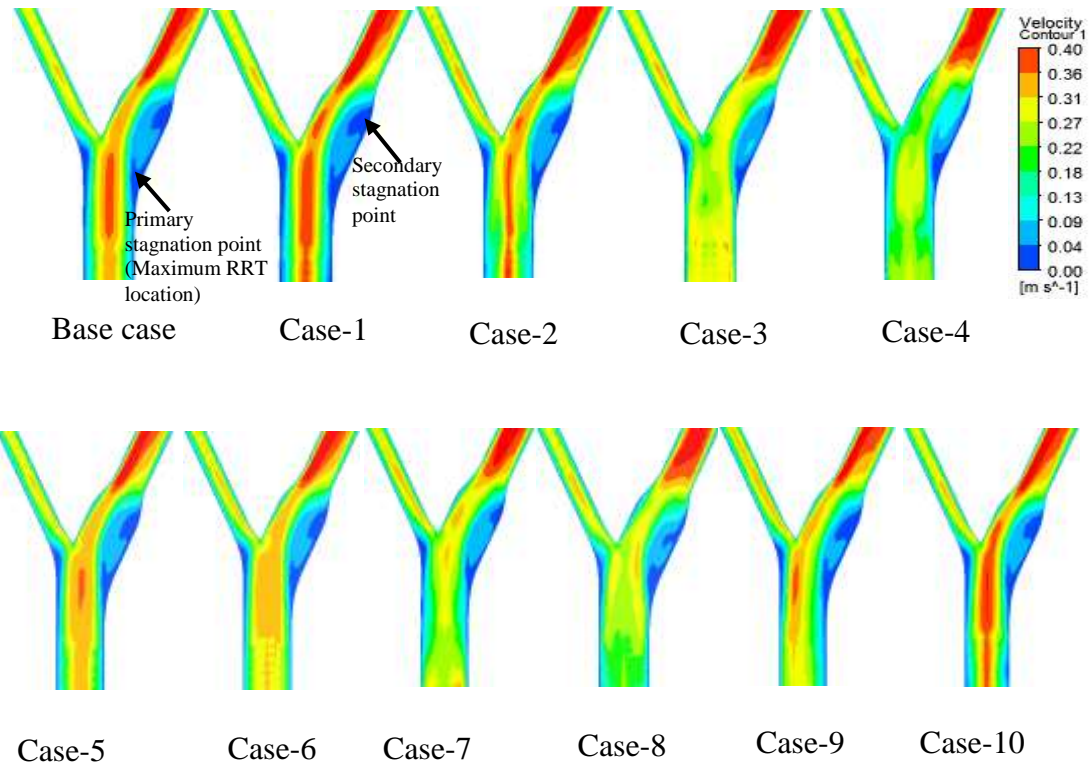


Figure 4.7. Velocity contours at an axial plane during deceleration time step.

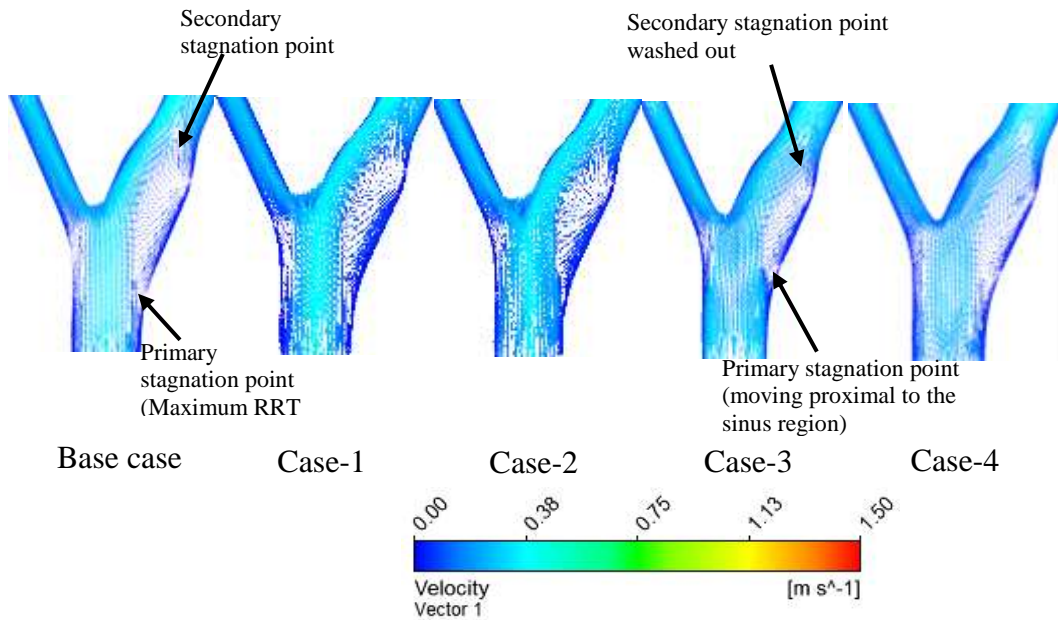


Figure 4.8. Velocity vectors during diastolic deceleration time instance for different rib heights.

Presence of coherent vortical structures in the flow field are identified by Q-criterion (Hunt and Hussain 1991) and shown in Figure 4.9. The vortical structures are drawn at

diastolic deceleration time instance for two different isovalues. The comparison is made with base case, single rib (Case 9) and two rib (Case 3) configurations. Smaller, weak vortices are filled in the CCA for the base case. These weaker vortices are washed away by a strong linked vortex in single rib design and two strong swirling vortices in the case of two rib configuration. The vortices present in the sinus region of base case is formed due to the bifurcation. They are seen at the middle of the passage without getting connected to the recirculation zone. Absence of swirl velocity component enhances more rigid vortices in the sinus region (Kolář 2007). It provokes the atherogenic particles to settle on the arterial wall. During the cardiac cycle, swirl generator induces strong swirl velocity component which intersect with weaker vortices at the sinus region. Random movement of weaker vortices is restricted by the action of swirl flow which washes out the weaker vortices component. Existence of stronger shear layers can be observed in the flow domain. Hence, in the swirl generator case sinus region gets filled with helical flows which are instrumental in reducing the stagnant regions.

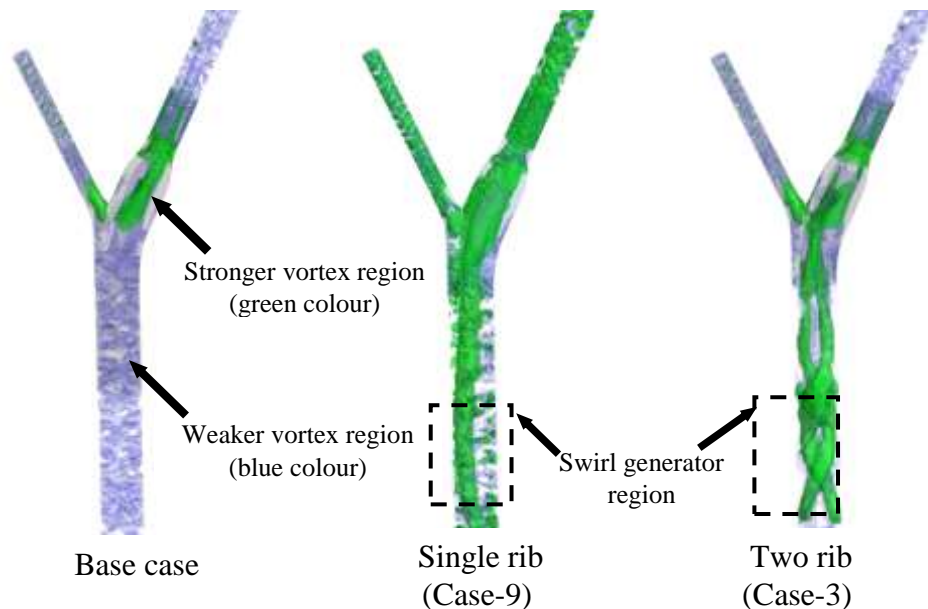


Figure 4.9. Coherent vortical structures expressed with Q criterion during diastolic instance.

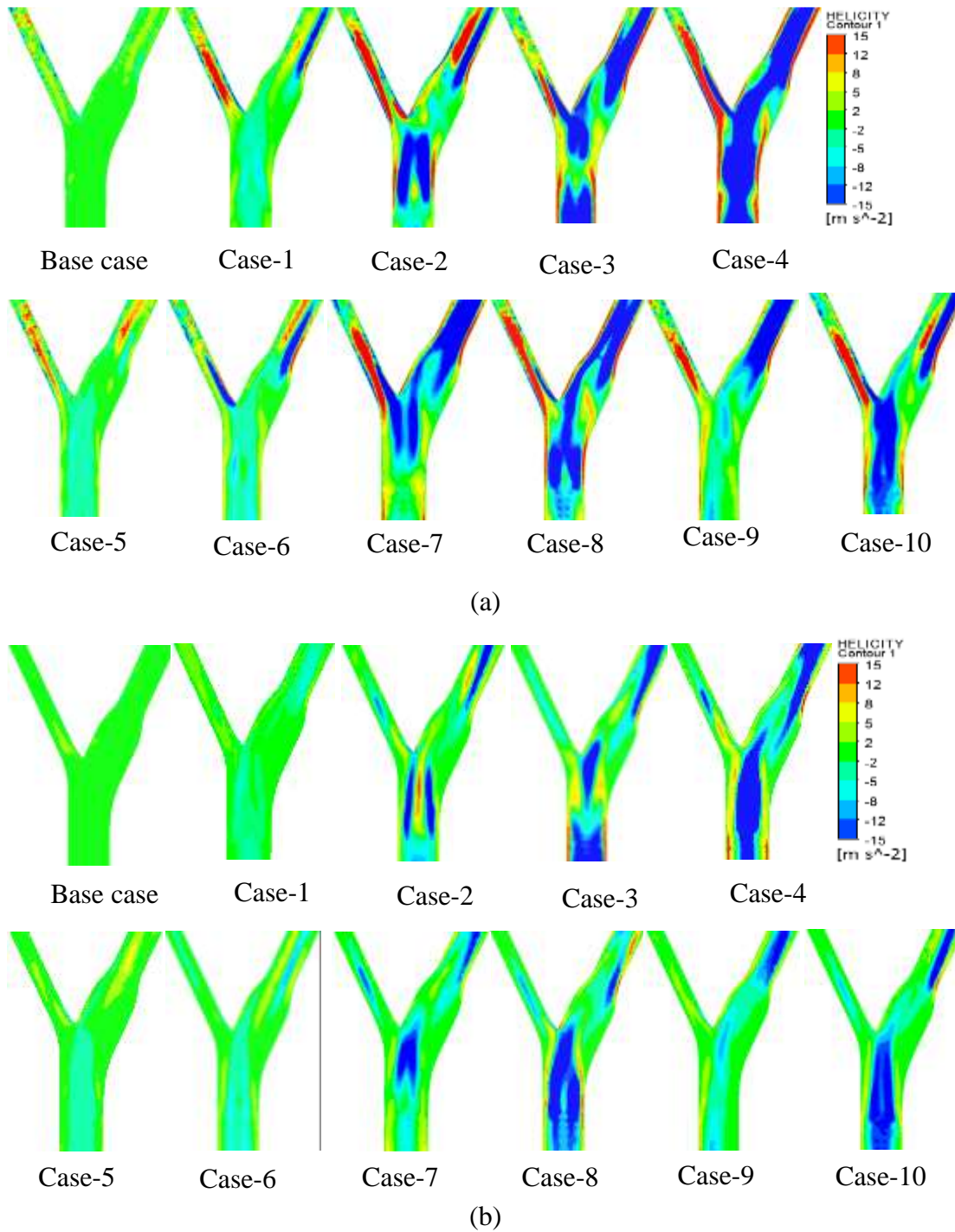


Figure 4.10. Helicity contours (a) Peak systolic (b) Diastolic deceleration time step.

4.4.4 Analysis on the induced helicity

The smaller residence time reported for the Cases 1-10 can be attributed to the helicity induced in the CCA by the swirl generator. This has been visualized by plotting the

helicity contour on an axial plane that passes through the center (Figure 4.10). With increasing rib height, helical angle and number of ribs the swirl generator induces more helicity in the arterial passage. Basically two counter rotating helical flow structures are generated in the passage. One with negative helicity (clockwise spin) in the ICA and with positive helicity (anticlockwise spin) in the ECA. A helical flow which replicates lower residence time with moderate pressure drop has favorable hemodynamic in the artery (Van Canneyt et al. 2013). Figure 4.10 represents the helicity induced at peak systolic as well as diastolic instances. The base case is devoid of any helicity mostly during the diastolic instance. Alignment of helix in the swirl generator induces anticlockwise spin near the periphery and clockwise spin at the center. Strengthened clockwise vortex at the center pushes the weakened vortices surrounding it to the arterial wall (Lee et al. 2011). This is evident from the plot of helical descriptors h_3 (Figure 4.11b). The value of h_3 vary from -1 to +1. Results indicate that base case inherently has a small positive spin while the swirl generator induces mainly a clockwise spin (negative vorticity) to the fluid domain.

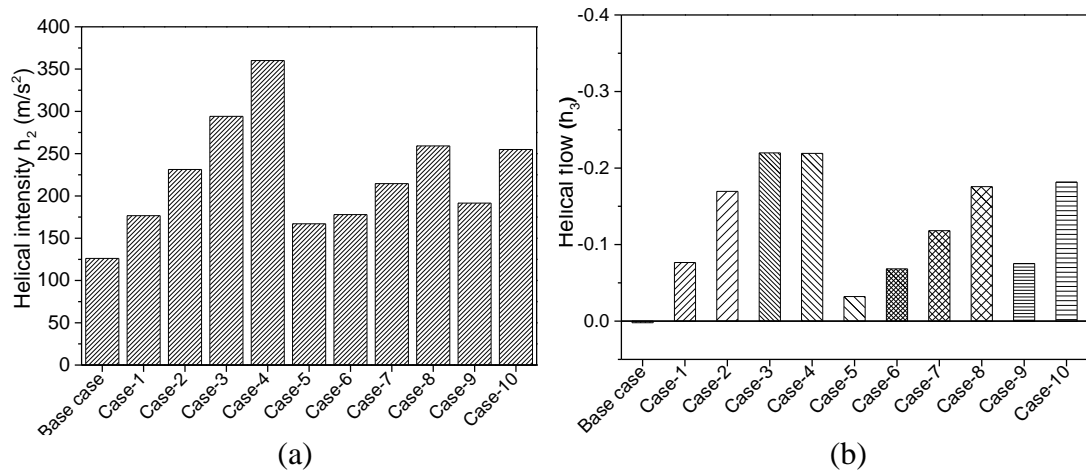


Figure 4.11. Quantitative analysis of helical flow strength in the bifurcated artery (a) Amount of helical flow in the domain represented with helical intensity (b) Helical flow structures in the domain.

4.5 Discussions

The degenerative material responsible for atherosclerotic plaque settles mainly at the outer ICA sinus region of the bifurcation zone (Berger and Jou 2000, Chiastra et al. 2017, Huang et al. 2014, Perktold et al. 1991, Pinto and Campos 2016, Steinman et al.

2000). Maximum relative residence time appears at this location and two stagnation points are observed. The primary stagnation point appears due to the separation of the boundary layer from the outer wall of the ICA, whereas the secondary one appears at the point of re-attachment. Inside the boundary layer flow reversal happens whose starting and ending points are demarcated by these two stagnation points. The helical flow makes the maximum kinetic energy from the centre to redistribute to the periphery. Due to this outward bound energy transfer from the central region, the boundary layer fluid gets energized. This delays the separation and hence the primary stagnation point move proximal to the bifurcation region.

Helical or swirl flow can minimize the risk factors that causes the atherogenesis. It can suppress the low and oscillating shear and act as a protective mechanism against plaque formation (Gataulin et al. 2015, Ha et al. 2015, Liu et al. 2015, Morbiducci et al. 2009, Stonebridge et al. 2004, Sun et al. 2010, Wong et al. 2010, Zheng et al. 2014, Zovatto and Pedrizzetti 2017). The present study reveals that adding a single rib swirl flow generator proximal to the stent treated passage can generate sufficient helicity to bring down the RRT 36% without creating any flow disturbances. The helicity values are positive near the wall, possibly due to the large velocity gradient in the radial direction. Predominantly negative helicity is induced in the main passage. However, after the bifurcation, both helicity streams (with opposite spin) interact in the sinus region. If the recirculation regions are pulled inside the helicity contours, then the RRT comes down as seen in Case 3. On the other hand, an improper helical angle makes the helical core regions move away from the recirculation zone. Under such circumstances the RRT value may be still high even though a large helicity is induced in the passage (as observed with Case 8).

Absence of swirl flow in the arteries makes it a poiseuille flow which may generate Kelvin–Helmholtz instability between centerline velocity of stream and surrounding fluid near to the wall region (Ha et al. 2015). The swirl flow adds azimuthal instability which increase vortex formations in the passage. Increased vortex formation enhances the mass, energy and momentum transport near to the wall region (Ha et al. 2015, Liang and Maxworthy 2005, Ma et al. 1997). Kilner et al. (1993) observed corkscrew like flow pattern in the ascending aorta as a result no atherosclerotic plaque formation

occurs in this region. This vortex formation is different from the vortices formed at the separated recirculation regions and the bifurcated zones. The induced helical flow in the domain provokes more linked vortices (coherent vortices), which may act as self-cleaning the arterial wall and may increase the stent life from restenosis. If the helical angle is not oriented properly the induced vortices may not efficiently bring down the residence time. In such cases, larger helical flow may not be very useful to prevent atherogenises.

A high value of helicity in the flow structure can increase in the flow resistance. The pressure drop incurred in the passage can be a measure of this flow resistance. The selection of the swirl generator has to be made based on the minimum time averaged pressure drop occurred in the passage. Among ten swirl case generator that has been tested Case-9 has been suggested for clinical practice as it does not offer any additional pressure drop, but reduces the RRT by 36%.

4.6 Effect of swirl generator in a flexible bifurcated artery

This section explores the effect of swirl generator fitted in a flexible artery model. Comparisons are made between bifurcated artery with and without swirl flow generator (base case). Arterial walls are considered as healthy (free from disease), isotropic, elastic homogeneous and incompressible with young's modulus of $E=0.4\text{MPa}$ and Poissons ratio=0.499 (Baldewsing et al. 2004). The portion with the swirl generator has been taken as rigid. Fluid boundary condition and properties are similar to the previous analysis. Simulations have been carried out for sufficient number of pulse cycles until to negligible difference has been observed with the results of last two cycles and final cycle results has been considered for the analysis.

4.6.1 Distribution of wall shear stress and Von misses stress on the Elastic wall

Figure 4.13 shows the wall shear stress distribution at the outer wall of the bifurcation region as well as on the ICA outer wall during one cardiac cycle. Enhanced swirl flow in the arterial passage improves the flow behavior during the diastolic phase. Increase of WSS during the deceleration phase decreases the residence time of particles, which

may settle on the arterial wall periphery. The low WSS value has been improved with the addition of swirl generator.

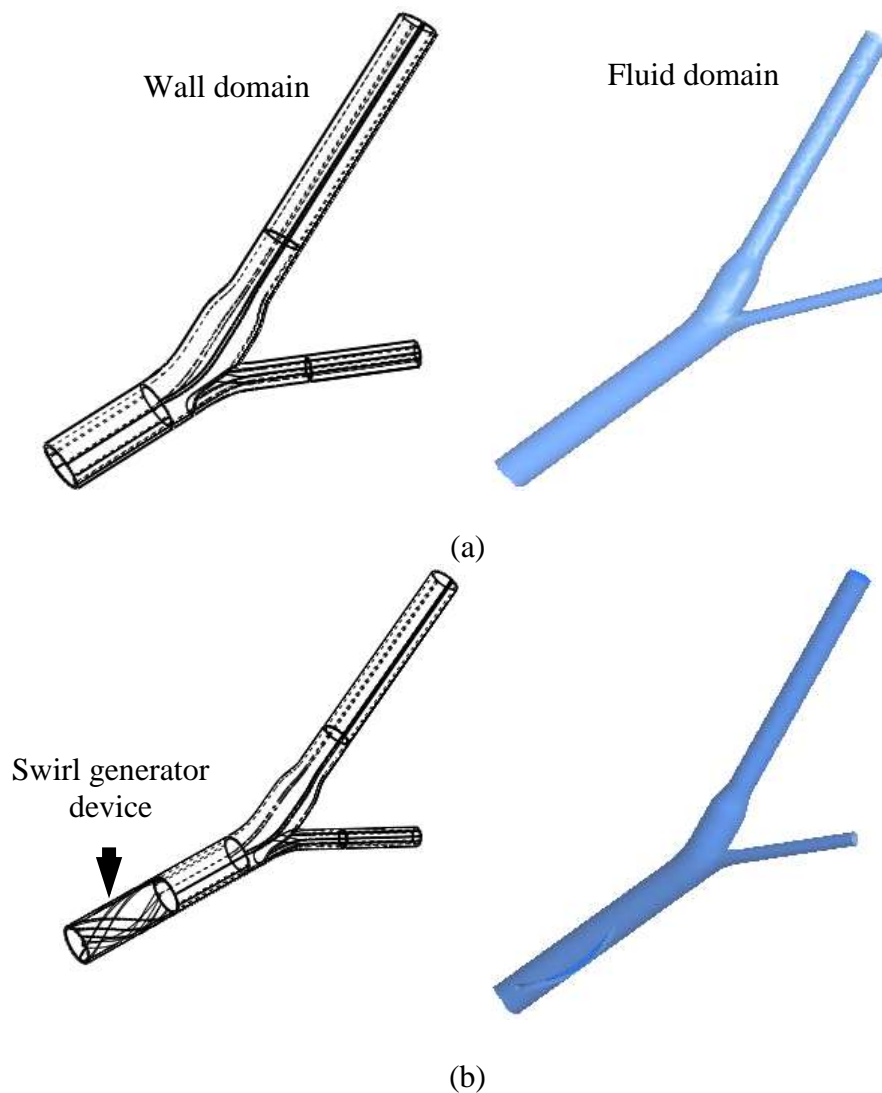


Figure 4.12. Models used for the simulation (a) Base case model (b) Swirl generator case (Case-9).

The Vonmises stress has been plotted on the wall at a cross section near the bifurcation (Figure 4.14). It shows that the stresses acting on the wall are similar for both cases during peak time step at the bifurcation region. However in the ICA region the swirl generator imposes slightly higher stresses on the wall.

Figure 4.15 shows the variation of Vonmises stress during one cardiac cycle on the outer wall. Once the flow enters through the daughter branches (ICA), reduction in the arterial passage may cause an increase in the stress for swirl generator case in

comparison with the base case. The average increase in the Vonmises stress is noted as 3% at the bifurcation zone and 5% in the ICA region for the selected points.

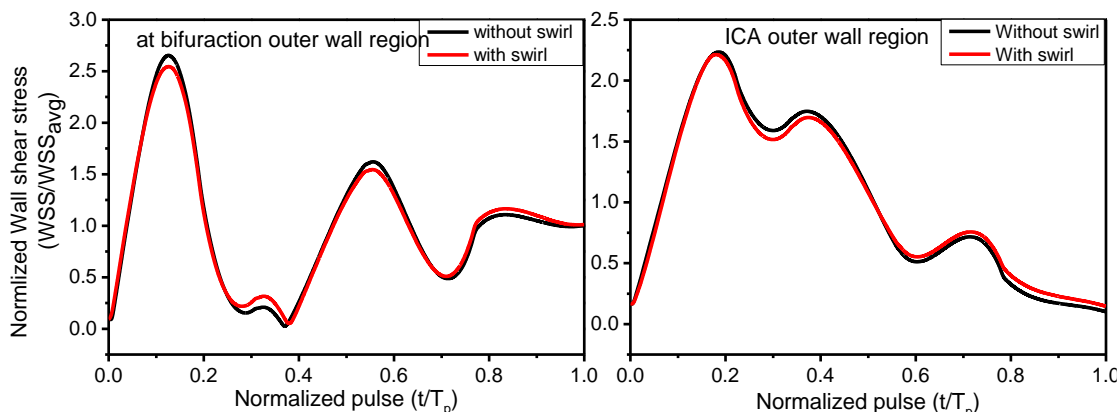


Figure 4.13. Comparison of wall shear stress distribution between without swirl generator and with swirl generator case (Case-9) during the cardiac pulse plotted on internal walls of ICA at bifurcation zone and in the ICA region.

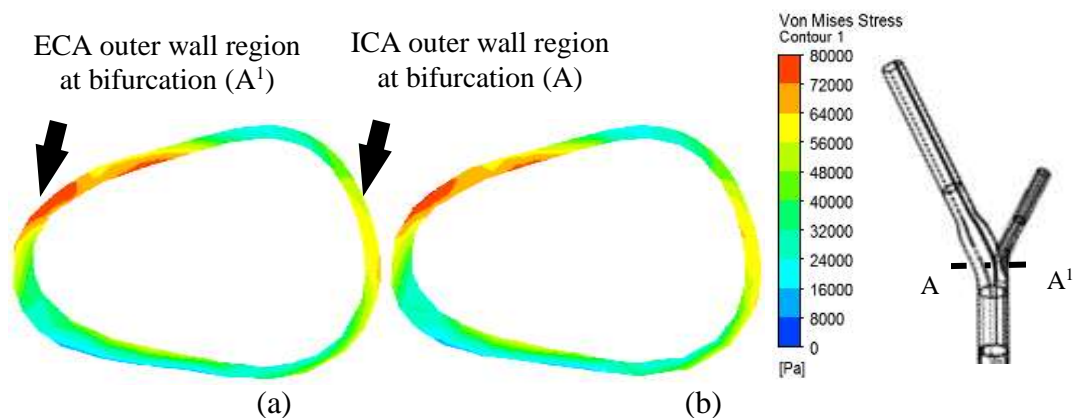


Figure 4.14. Von mises stress distribution at the bifurcation wall region (AA¹) during peak cardiac cycle (a) without swirl generator (b) with swirl generator.

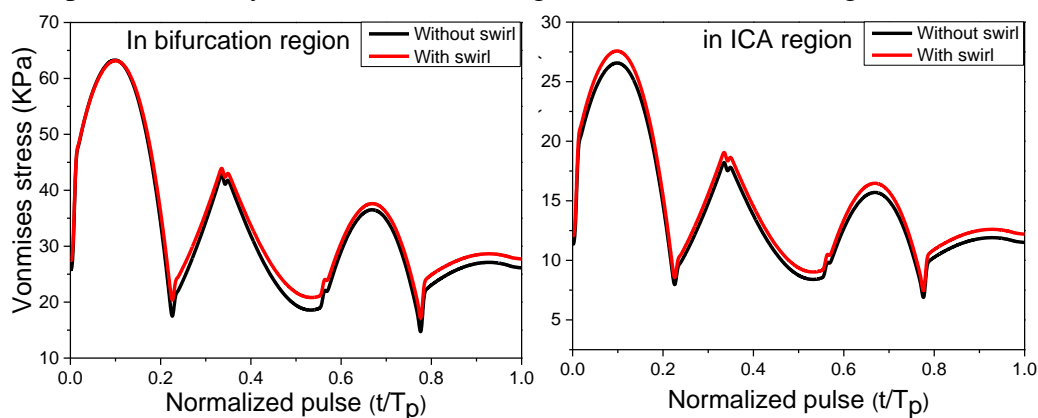


Figure 4.15. Comparison of Vonmises stress distribution between without swirl generator and with swirl generator case (Case-9) during the cardiac pulse plotted on internal walls of ICA at bifurcation zone and in the ICA region.

4.7 Summary of the chapter

A computational investigation has been carried out on an idealized bifurcated artery to understand the effect of an induced helicity on the hemodynamics. For inducing helicity, a swirl generator has been proposed. The present study focuses on the conceptual design of the swirl generator and it is envisaged as a stent-like device with an internal groove.

- Generation of helical flow and disturbed shear layers in the complex flow field is effectively suppressing the recirculation zones. Thus the, accumulation of atherogenic particles is minimized by controlling the relative residence time of fluid layer near the wall.
- The height of the rib, helical angle and number of rib have varied systematically to identify an ideal swirl generator which brings down the RRT while offering minimum flow resistance.
- Two stagnant regions are observed at the outer wall of the ICA. With increased helicity the primary stagnation point moves proximal to the bifurcation region.
- The helical flow makes redistribution of the kinetic energy from the centre to the periphery. This outward bound energy transfer from the central region, makes the boundary layer fluid gets energized causing a delay in the separation of fluid layer from the arterial wall.
- Among the tested configurations, swirl generator with single rib and 180 deg. helical angle offers 36% reduction in the relative residence time without creating any significant flow resistance.
- Detailed flow analysis revealed the existence of stronger shear layers due to the induced helicity, which washes out the weaker vortices component by the action of swirl flow.

- The turbulent kinetic energy is uniformly distributed around the arterial periphery by the induced swirl flow and hence it does not create any vascular injury on the arterial wall.

5 STUDIES ON PATIENT SPECIFIC GEOMETRIES

In this chapter computational investigations are carried out on real patient specific arterial geometries. Initially studies are carried out to understand the effect of degree of stenosis (DOS) on the temporal and spatial variations of wall shear and oscillatory shear. The study has been undertaken on four different subjects whose DOSs are 41%, 56%, 62% and 69%. The effect of swirl generator on the hemodynamics of this real arterial geometry has also been studied in the later part of this chapter.

5.1 Geometry reconstruction from CT scan images

The patients in the current study are a subset of the sample of patients studied in previous works by this group (Gupta et al. 2014, Gupta et al. 2015), focused on correlation of plaque imaging characteristics and symptomatic disease. This study, including the retrospective review of clinical standard of care imaging data performed between August 2009 and March 2014, was approved by the Human Subjects Institutional Review Board of our institution. Of note, the DICOM imaging data analyzed for this study contains no protected health information. Moderate-to-high-grade extra-cranial internal carotid artery stenosis (50 to 99% stenosis) has been measured on CT angiography studies. The detailed method for NASCET stenosis measurement is described in these prior works (Gupta et al. 2014, Gupta et al. 2015), though of note the degree of stenosis used for our analysis was not based on NASCET-style measurements. Atherosclerotic plaques included in this study has been analyzed by a board-certified neuro-radiologist to determine the single axial source image with greatest luminal diameter narrowing.

A series of scanned Computed Tomography (CT) images of four patients covering the carotid bifurcation artery with significant carotid artery stenosis, lumen and wall surface of the carotid bifurcation are obtained. The DOS of all the patients are calculated based on the relative minimum diameter (D_{min}) of the internal carotid artery (ICA) with respect to the diameter of the non-stenosis (D) region in the common carotid artery (CCA).

$$\text{Degree of stenosis} = \left(1 - \frac{D_{min}}{D}\right) \times 100 \% \quad (5.1)$$

A series of scanned images are shown in Figure 5.1a, for a representative model, to demarcate the CCA, ICA, ECA and the bifurcation regions. The bright white spot in the image represents the calcium deposit within the plaque. The lumen portion was traced out from the CT image using an in-house software (ImgTracerTM, courtesy of AtheroPoint, Roseville, CA, USA). The output of the ImgTracerTM is the x-y coordinates in terms of pixels. This is further converted into millimeter (based on the resolution) and then feed into a commercially available 3D geometry modeller ICEM CFD to prepare the required polylines upon which the surface will be created (Figure 5.1c). Smoothing of the surface has been done using another 3D modelling software CATIA. The three dimensional computational models of the four geometries are shown in Figure 5.2. For the present study, the computational simulations are carried out using a Finite Volume Method (FVM). Unstructured tetrahedral elements are used for grid generation. Prism elements are attached to the walls in order to capture the boundary layer effects.

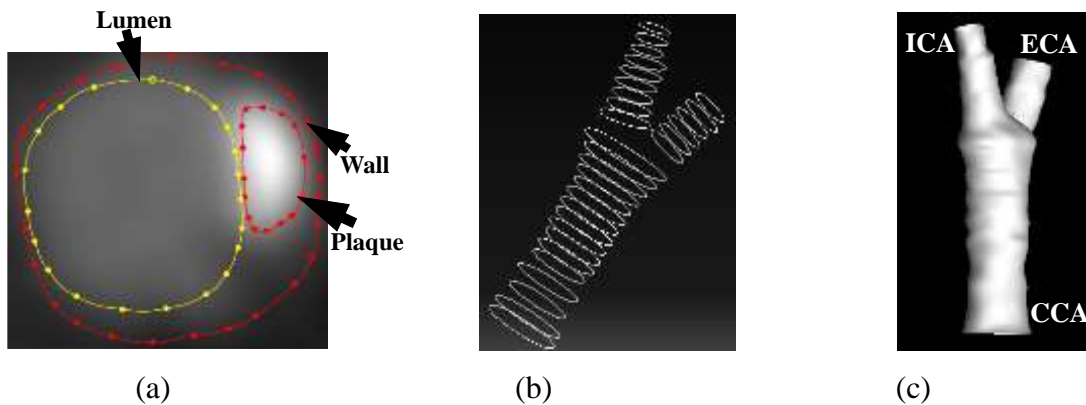


Figure 5.1. (a) Tracing of the vessel lumen with image tracer (b) Traced points are converted into polylines in ICEM CFD (c) Final 3D model generated.

Table 5.1 Degree of stenosis calculated for each patient.

Patients No.	DOS (%)
<i>Patient 1</i>	62
<i>Patient 2</i>	41
<i>Patient 3</i>	56
<i>Patient 4</i>	69

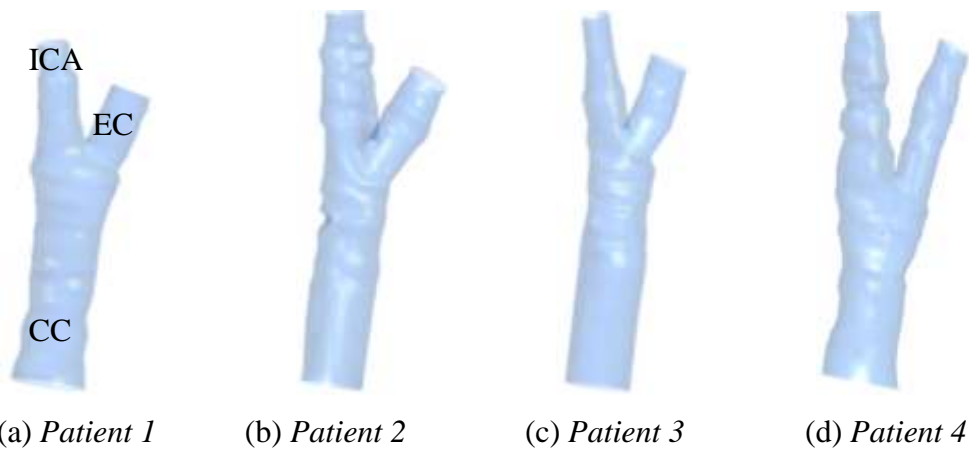


Figure 5.2. Carotid bifurcation models for the four models, showing the common carotid artery (CCA), external carotid artery (ECA) and internal carotid artery (ICA).

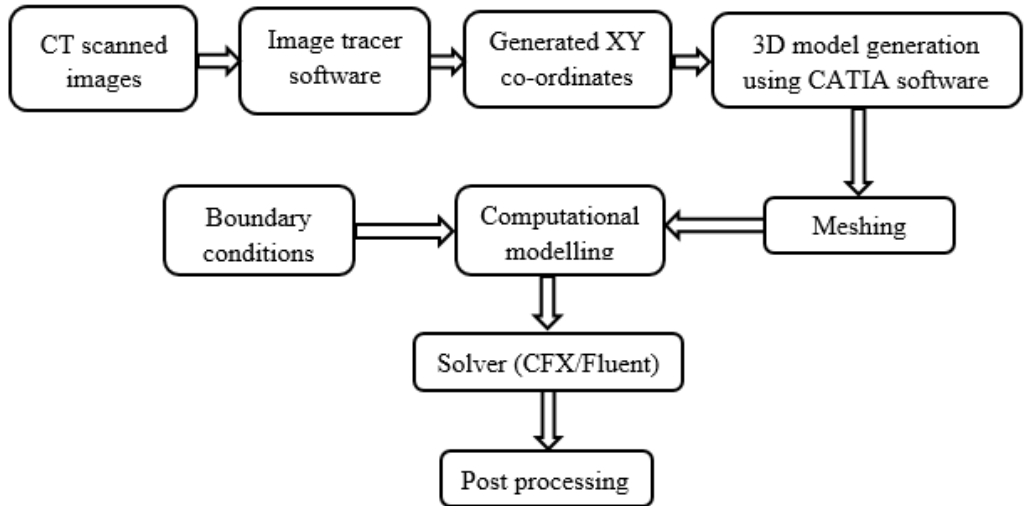


Figure 5.3. Computational approach for a real patient specific data.

5.2 Fluid models and boundary conditions

Blood modelled as an incompressible, homogeneous viscous fluid, with a density of 1060 kg/m³. The rheological model of blood has been studied by several researchers (Lee and Steinman 2007, Morbiducci et al. 2011, Perktold et al. 1991) accordingly it is treated as Non-Newtonian using the Carreau- Yassuda model. The governing equations are the time dependent Navier-Stokes equations (Perktold et al. 1991).The turbulence methodology adopted for this study is the Large Eddy Simulation (LES). LES resolves

the larger turbulent eddies whereas the smaller ones are modelled during the pulsatile flow (Lantz et al. 2016, Varghese et al. 2008).

A time varying pressure boundary condition is specified at the inlet and time varying velocity profile is set at the end of ICA and ECA (Figure 5.4). The specified values are spatially uniform, but pulsating with respect to time. The assumed pulse frequency is 80 strokes per minute. Time dependent behavior for unsteady simulations is specified through time period and time step. A time step (t) of 0.001s is specified and the iterations are carried out till the convergence criteria is met.

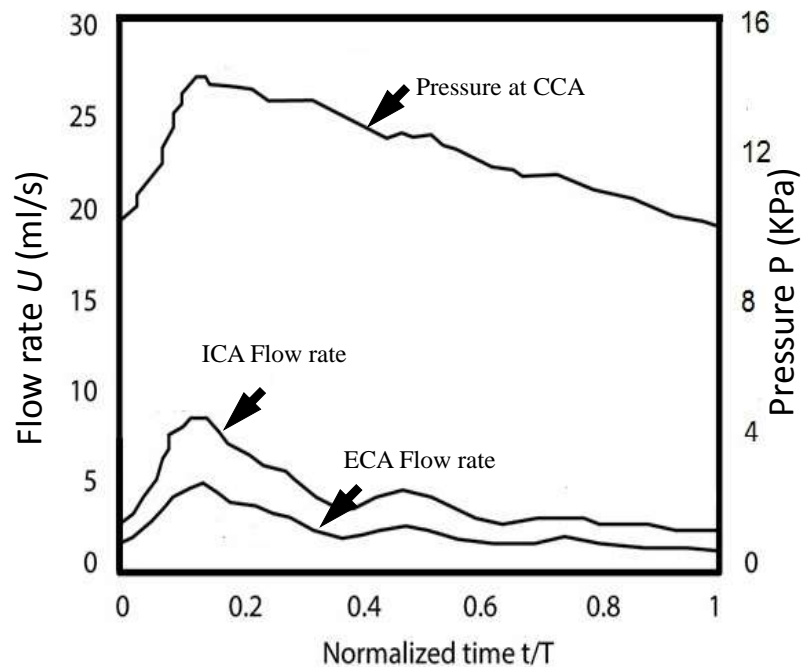


Figure 5.4. Inlet pressure as a function of normalized time used for the simulation within the carotid bifurcation. The corresponding flow rate at the exit of ICA and ECA are also shown.

5.3 Results and discussion

5.3.1 Effect of degree of stenosis on WSS and OSI

The WSS in the vessel lumen is a function of the inlet velocity at the CCA. As the inlet velocity for all these models are different, this variation will reflect in the WSS comparison also. In order to avoid this, WSS values are normalized with their corresponding average values and then the comparison is made with different models.

The temporal and spatial variations of the WSS at the inner as well as outer wall of the ICA are noted down. Two polylines are created; the outer one running from the CCA inlet to the ICA outlet and the inner one running from the bifurcation zone to ICA outlet (Figure 5.5a) at systolic peak and the spatial average of WSS along the respective line is used for the normalization. Figure 5.6b - c show the variation of the normalized WSS along the inner and outer wall of the vessel lumen.

The variation of the WSS on the outer wall of four model reveals that, up to the bifurcation zone WSS is maximum for *patient 2* (low DOS model), and it was minimum for the *patient 1* (high DOS model). Note that the bifurcation zone starts at a normalized distance of around 0.64. After the bifurcation zone, the normalized WSS value suddenly has increased for *patient 1* due to the protrusion of the plaque, which restricts the effective flow area.

These characteristics indicate that with high stenosis models occupies a large value of normalized WSS in the ICA whereas they have smaller values of normalized WSS in the CCA. The peaks to trough variations are lower for the *patient 2*, which is attributed to its lower value of the DOS. Just after the bifurcation zone a sudden rise was observed for *patient 4*, followed by a sharp trough also. This low normalized WSS region may be identified as hotspot for further plaque progression. The peaks in the graph corresponds to the protruded plaques into the vessel lumen. The fluid accelerates here creating a high wall shear stress. Each protrusion is followed by a low velocity wake region causing potential zone for the progression of atherosclerotic plaques.

The temporal variation of normalized WSS is noted at two points on either side of location B. The peak value of WSS during systole, and the least value occur at the decelerating phase of the systole, indicating that the decelerating phase is the most conducive phase for atherogenesis. At the outer wall, *patient 1* showed large temporal variations in the WSS value, while at the inner wall it was with the *patient 4*. Hence, for *patient 4* further chances of atherosclerosis progression occurs at the inner wall of the ICA.

Figure 5.6a – d shows angular variation of the normalized WSS along the circumference at three different axial locations, A, B and C (Figure 5.5a). The normalized WSS are plotted at peak systole at different theta values with the radius showing the magnitude of the normalized WSS. The circumferential non-uniformity of the shear stress is quite visible from these plots. As the flow proceeds through the ICA, the peak value of shear stress shifts from one angular location to other due to the secondary flows. The locations where the WSS value becomes zero are recirculation/separation zone. Such a disturbed flow region occurs at 270° for *patient 4* in the CCA. It is observed that, the high degree of stenosis models (DOS above 60%) occupies a smaller values of normalized WSS in the CCA, but after the bifurcation zone the spatial and transient average shear stress rises with DOS. While comparing models with different degree of stenosis it is recommended to compare the normalized value of shear stress rather than the absolute value of shear stress in order to understand the severity of atherogenesis progression.

Oscillatory Shear Index (OSI) measures the cyclic departure of the wall shear stress vector from its predominant flow direction. A high value of OSI indicates a severe compression and stretching of the lumen wall which accelerate the plaque rupture (Equation 4.2). The variation of OSI along the inner and outer walls of the ICA are shown in Figure 5.7a - b. The magnitudes of the oscillatory shear are high for *patient 1* and *patient 4* and it is spread over a wider region along the circumference of the wall compared to *patient 2* and *patient 3*. The angular variation of OSI indicates a high level of risk for the *patient 1* and *patient 4* (Figure 5.7c - f). The larger magnitude of oscillatory shear implies a higher stretching and compression of the vessel wall which can cause sufficient damage to the endothelial cells. Higher OSI values along the circumference imply higher risk for plaque rupture in that region.

The location of the maximum OSI may not be correlating with the location of the peak shear stress. On the contrary, the OSI values are high where the flow disturbance are more. In the ICA region maximum oscillatory shear is observed for *patient 4* and the minimum is for *patient 2*. For *patient 2*, high level of oscillatory shear can be observed at certain localized points inside the ICA.

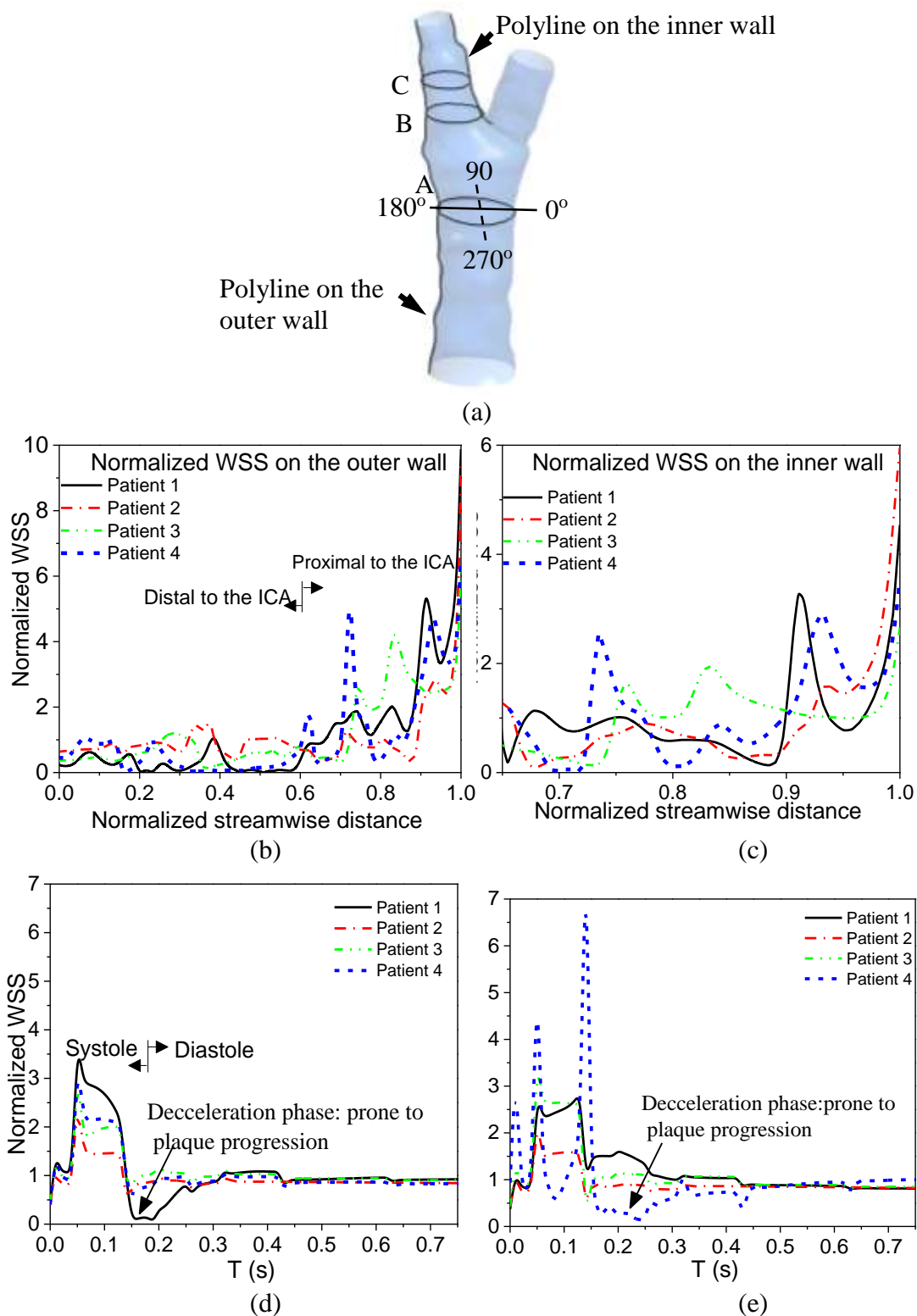


Figure 5.5. (a) Representative model showing specific locations where the WSS values are extracted. Variation of the normalized WSS during peak systole (b) on the outer wall of the vessel lumen (c) on the inner wall (d) on a point at the outer wall during pulsatile flow (e) on a point the inner wall during pulsatile flow.

The angular arrows in the Figure 5.7 represent the circumferential regions where the OSI value is zero. For *patient 2* and *patient 3* the OSI values are almost nil around the periphery of the vessel lumen, implies they are at less risk. With higher DOS the flow becomes more rotational in the vicinity of plaques causing the oscillatory shear to have a high non-zero values at these locations.

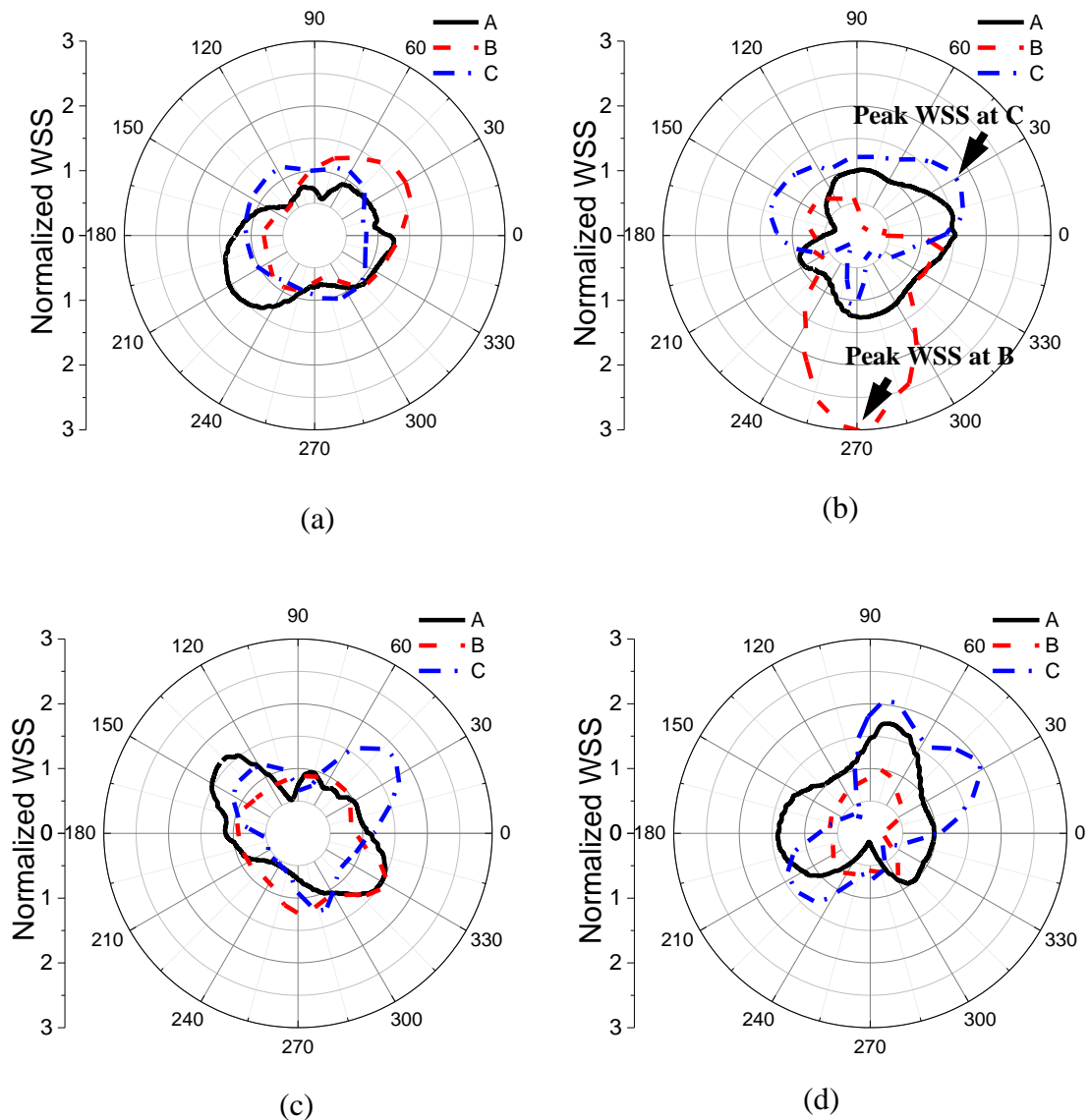


Figure 5.6. Angular variation of normalized WSS at different axial locations for (a) *patient 1* (b) *patient 2* (c) *patient 3* and (d) *patient 4*.

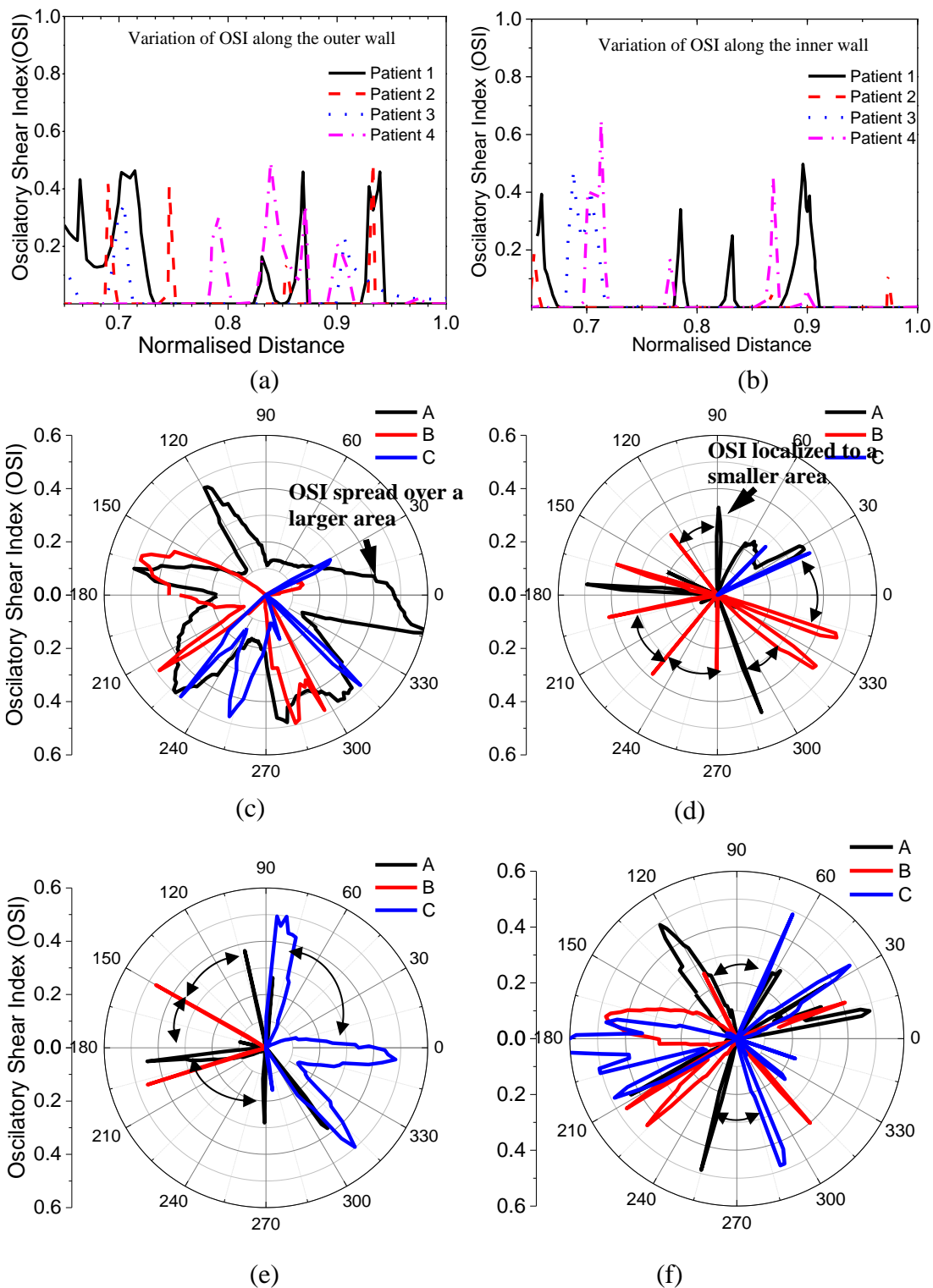


Figure 5.7. Variation of the OSI (a) on the outer wall of the vessel lumen (b) on the inner wall. Angular variation of OSI at different axial levels for (c) *patient 1* (d) *patient 2* (e) *patient 3* and (f) *patient 4* (The angular arrows shows the circumferential regions where the OSI value is zero).

The magnitudes of the oscillatory shear are high for *patient 1* and *patient 4* and it is spread over a wider region along the circumference of the wall. For the low DOS models (*patient 2* and *patient 3*) the oscillatory shear is absent at majority of regions, instead it appears only at certain localized regions. While the maximum value of OSI are comparable with the different DOS models, their average value throws a different picture. Hence, for clinical use in order to represent the severity, it is recommended to use the average value of oscillatory shear than the maximum value.

5.3.2 Understanding the bulk flow behavior through limiting streamlines plots

Observing the behaviour of surface streamlines, otherwise known as limiting streamlines, helps to understand the secondary flows, region of separation and reattachment points. The magnitude of WSS depends on the velocity vectors near the surface. In Figure 5.8 the pattern of the surface streamlines are different in each case and it solely depends on the irregularity of the vessel lumen. Just before the bifurcation zone a line of separation can be observed for all the cases.

In region where the plaque thickness are high, the intima region projects deep into the lumen and the streamlines flow around to form a low velocity wake region at the downstream. This further reduces the wall shear stress at the downstream which enhances the deposition. Secondary flow originates in the bifurcation region and spirals through the internal carotid artery. The stenosis in the ICA region is asymmetric which results in a nonuniform velocity contours. It can be seen that for *patient 2* the streamlines are almost straight and devoid of any secondary flow patterns. However this is not the case with *patient 1* and *patient 4*, where large crossflows are observed.

The behavior of the fluid flow can be understood by the nodal points and focal points. The nodal point of attachment can be identified from the lines that emerge from the point and spread out over the surface. On the other hand, the nodal point of separation acts as a sink where the lines may vanish (Tobak and Peake 1982). A focus is formed when a number of limiting streamlines spiral around the singular point, either away from it (a focus of attachment) or into it (a focus of separation) and it generally occur in the presence of rotation. The analysis of limiting streamlines for one representative model (*patient 4*) is shown in Figure 5.8b. For better understanding, flow vectors are

plotted on two longitudinal planes and is shown here. Corresponding to the nodal points, flow separation regions are visible from the flow vectors. In a similar fashion with the help of limiting streamlines, flow separation regions can be identified along the flow passage. A point of attachment is seen at the bifurcation zone where the limiting streamlines are going outwards. In the CCA a focal point is visible indicating the presence of swirl.

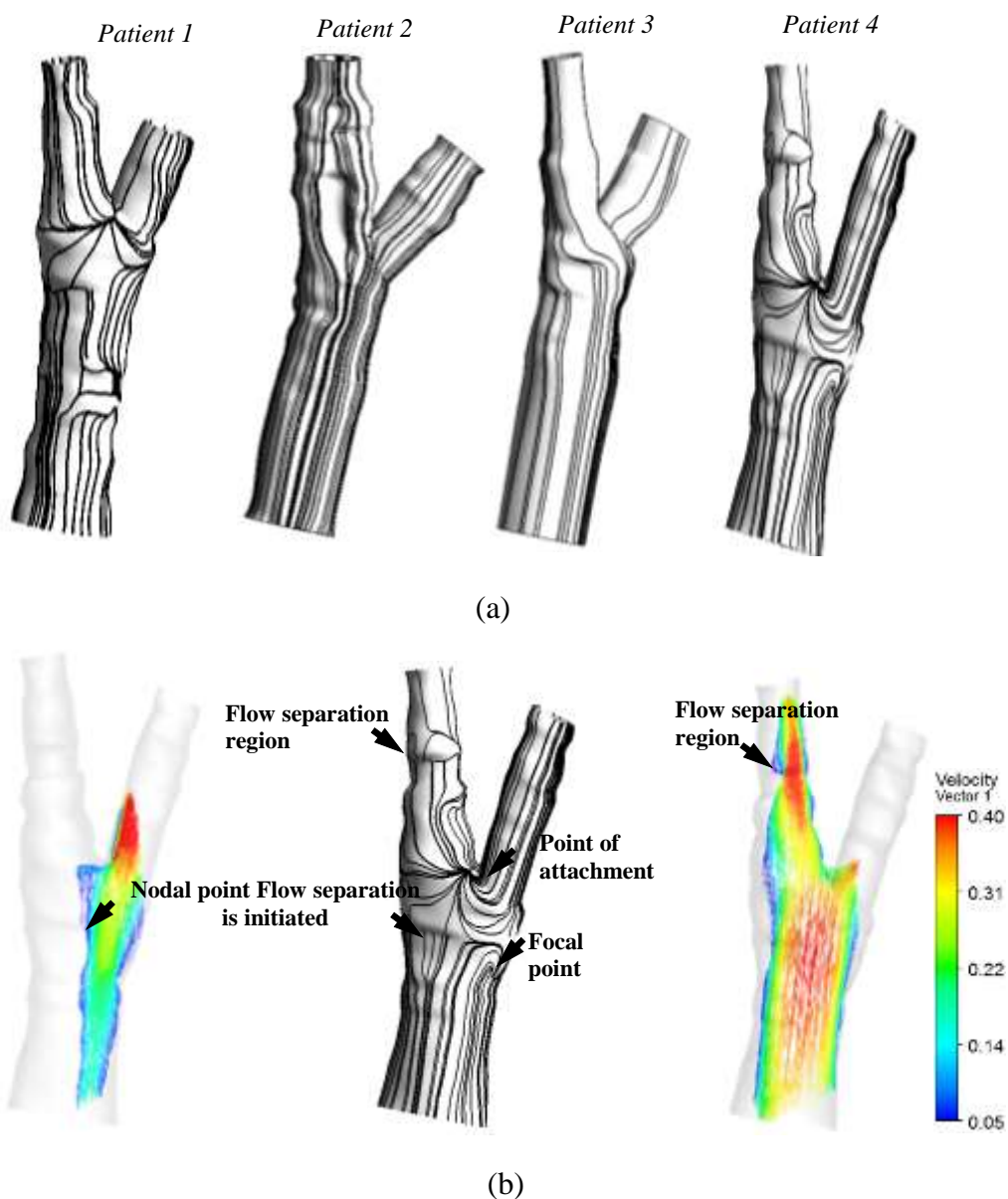


Figure 5.8. (a) Surface stream lines during peak systole ($t= 0.1$ s) for different geometric model (b) Limiting streamlines are shown along with the flow vectors inside the flow passage for *patient 4*.

5.3.3 Resultant vorticity contours

The swirling strength of the flow can be measured by calculating the resultant vorticity. In the present analysis it is observed that the vorticity in the X and Y directions are prominent compared to the Z direction. The Z direction is in align with the normal to the inlet of the CCA. Figure 5.9a shows the direction of the resultant vorticity with respect to X axis on the Z - X plane. From the positive Y direction a counter clockwise rotation is indicated by the red color and the clockwise rotation is shown with the blue. The change in the vorticity angle reveals that after bifurcation zone a change of spin happens with the resultant vorticity. This change of spin is caused by the secondary flows originated from the inner wall of the bifurcation zone to the outer wall. It is to be noted that the location at which this direction change happens move towards from the inner wall of the ICA to the outer wall. This can be seen in Figure 5.9b where the vorticity angle is plotted in three different planes for *patient 1*. This phenomena is observed in the other models as well. The resultant vorticity direction changes not only at the bifurcation zone, but it changes wherever the secondary flows are significant.

The variation of angular location of the peak shear stress inside the ICA is in correlation with this bulk flow hemodynamics. Table 5.2 shows the comparison of some of the critical attributes between the four models. Turbulence has a major role in the thrombogenesis and the mass transfer between the endothelial cells with the blood. Kefayati and Poepping (2013) detected transitional flow in 50-70% stenotic models through their study, in vitro, wherein the surface undulations are not taken into account. In the present analysis, it was observed that for a high stenosis of 66% (*patient 4*) the turbulent intensity is 8% at the stenotic region (Table 5.2). This is a local maximum and the within the computational model this may be even higher. However, for *patient 2* the turbulent intensity is only 0.1%. These results are in accordance with the studies conducted by May et al. (2002) in rat carotid artery. It could appear that a threshold DOS value of 60% generates a turbulent intensity more than 5%. However, this may not be seen as a general result as the present study has been done only on four models. Even though the maximum value of OSI is comparable for different DOS models, the average oscillatory shear stress of *patient 4* (DOS = 69%) is 300% higher than *patient 2* (DOS = 41%) at the outer wall and it is 400% higher at the inner wall.

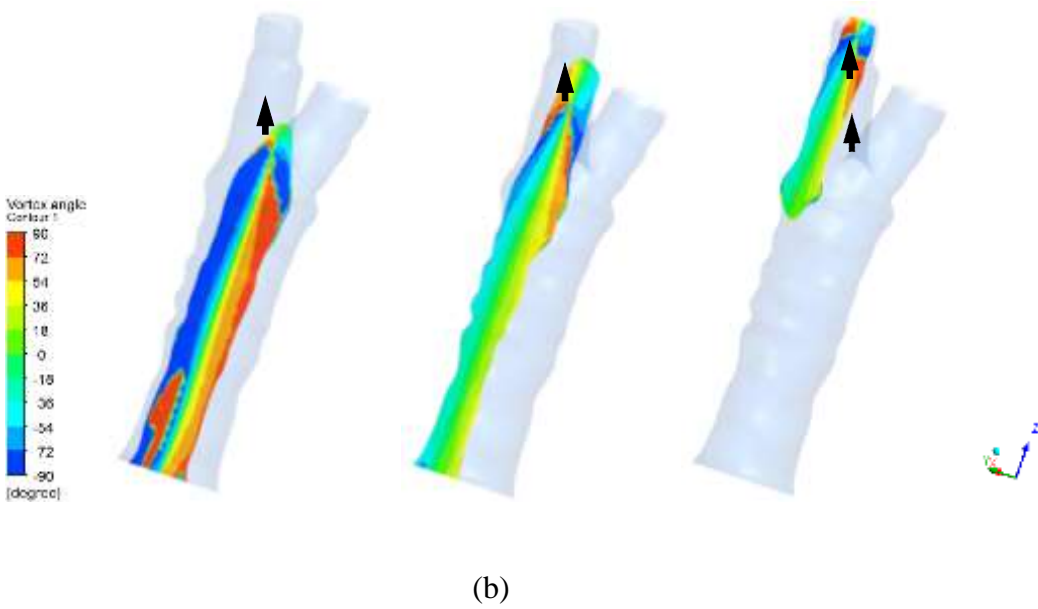
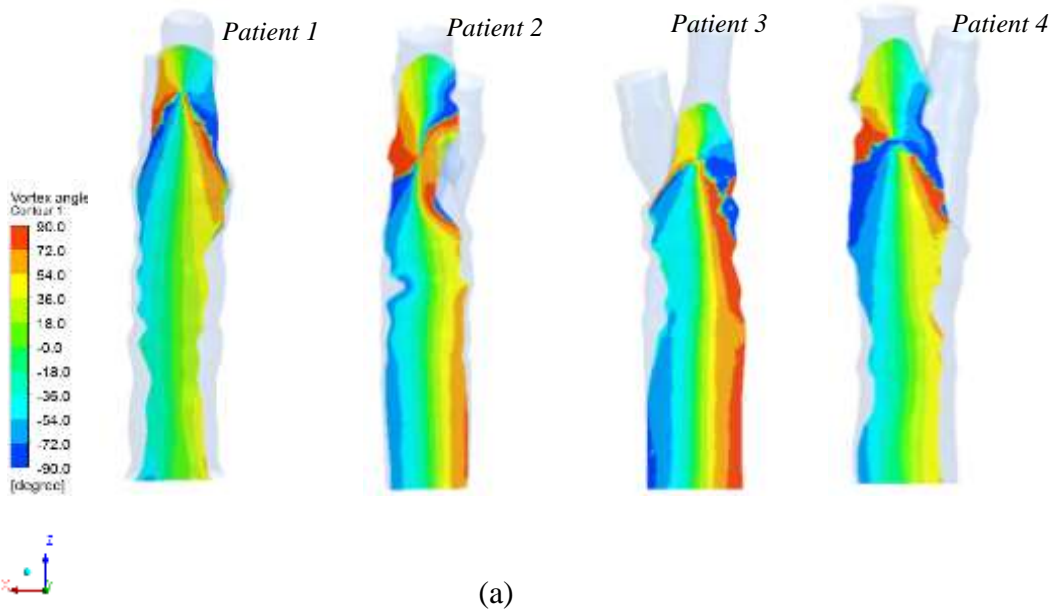


Figure 5.9. (a) The resultant vorticity angle with respect to X axis (b) The resultant vorticity angle at three different longitudinal planes for *patient 1* (arrow indicates location of spin change).

Table 5.2 Comparison of few critical attributes between the various computational models.

Attributes compared	<i>Patient 1</i>	<i>Patient 2</i>	<i>Patient 3</i>	<i>Patient 4</i>
DOS (%)	61.5	41.0	56.2	69.1
Turbulent intensity (%)	6.6	0.1	0.85	8
OSI average outer wall	0.22	0.016	0.056	0.10
OSI maximum (outer wall)	0.60	0.48	0.50	0.5
OSI average (inner wall)	0.05	0.02	0.04	0.08
OSI maximum (inner wall)	0.50	0.48	0.57	0.65

5.4 Performance of swirl generator in patient specific models

The suitability of swirl generator in real arterial geometry has been tested and detailed in this section. Due to the lack of available healthy (stent treated) patient data for the geometry construction, swirl flow inducer has been implemented in the available stenosed patient data. As mentioned previously the swirl generator must provide sufficient helicity while causing minimum pressure drop or flow resistance. With these criteria swirl generator with single rib and 180 deg. helical angle which offers 36% reduction in the relative residence time has been selected for patient specific arterial geometry (device diameter has been changed with respect to patient CCA diameter). Figure 5.10 shows the swirl flow inducer within the patient specific carotid artery model (*Patient 1*). Length of the helicity generator is three times the CCA diameter and it is placed away from the bifurcation region, enough length is provided to generate fully develop flow in the CCA passage and also at the inlet and outlets sufficient length have been provided to enhance the fully developed flow. The solver modeling and physics set up remains similar to that of the previous sections.

5.4.1 TAWSS on the outer wall

The hemodynamic performance in the swirl flow can be improved in terms WSS and fluid velocity near the arterial wall. Increase of these hemodynamic parameters reduces the possibility of plaque deposition. For analyzing the results two polylines are created;

the outer one running from the CCA inlet to the ICA outlet and the inner one running from the bifurcation zone to ICA outlet (Figure 5.10).

Figure 5.11 illustrates the distribution of time averaged wall shear stress (TAWSS) with respect to the normalized stream wise distance (CCA to ICA) for all the patients. Comparisons have been made with data obtained from cases without swirl generator (base case). Normalized stream wise distance 0 to 0.6 represents the CCA outer wall (ICA section side) and 0.6 to 1 shows bifurcation region to the ICA outlet. With the introduction of swirl flow at the entrance, increase of WSS can be observed throughout the TAWSS plots. Constricted (stenosed) flow passage in the ICA region reflects peak WSS, which starts from 0.6 stream wise distance. Swirl flow generator at the CCA enhances the azimuthal vortices by suppressing low wake turbulence in the pulsatile flow. Due to swirl flow effect, the newly formed azimuthal vortices expands radially, which enhance the momentum transfer near the arterial wall. As a result, the near wall velocity vector fields gets energized and enhances the WSS. Hence, patients with swirl flow reflects high WSS than base case models. Zeller et al. (2016) pointed out that high wall shear stress generated by swirling blood flow causes reduced progression/development of atherosclerosis and restenosis.

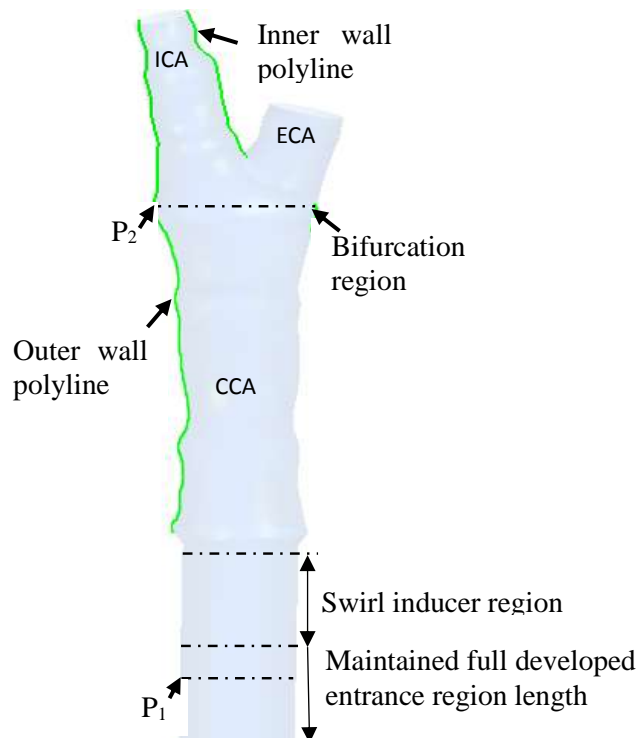


Figure 5.10. Swirl generator in the patient specific arterial passage.

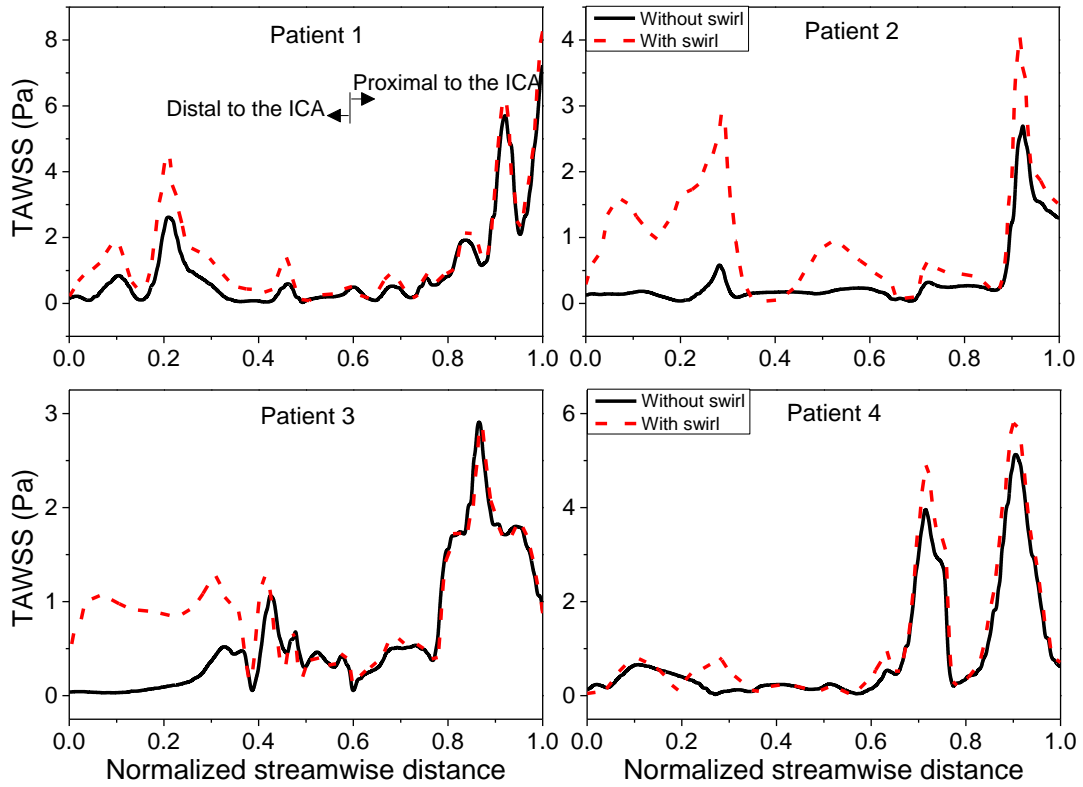


Figure 5.11. Variation of TAWSS along the outer wall of the arterial wall (CCA to ICA).

5.4.2 Flow field analysis with swirl generator

Detailed flow analysis of time averaged relative residence time on the outer wall (CCA to ICA), time averaged pressure drop across the CCA and the helicity descriptor h_2 (Chapter 4) are calculated for all the patient models with swirl generator and poiseuille flow inlet condition. Clinically, flow resistance across the blood vessel is an important parameter while inducing swirl flow at the CCA. Hence, area average pressure drop has been calculated between inlet of the swirl generator and the bifurcation region (noted as P_1 and P_2 in Figure 5.10). Table 5.3 represents the detailed comparison of major hemodynamic parameters with and without swirl generator. The pressure drop or the flow resistance caused by the swirl generator is smaller for *Patient 2* and *3* (3%). However for other two real geometries almost 8% increase is observed. In other words, cases with higher percentage of constriction (*Patient 1* and *Patient 4*) predicted higher pressure drop than with lesser degree of stenosis. Enhanced swirl in the pulsatile flow bring down the residence time of the fluid layer in all the cases. The percentage

reduction in the RRT is different for each models, suggesting that the topology of the lumen wall has significant impact on the residence time.

Table 5.3 Comparison of swirl generator designs with base case.

Patient specific model	DOS (%)	Case study	Pressure drop, % deviation compared with Base case	RRT, % decrement compared with Base case	Helicity γh_2 (m/s^2)
<i>Patient 1</i>	62	Without swirl	--	-	9.5
		With swirl	8.36	63	24.3
<i>Patient 2</i>	41	Without swirl	--	--	9.8
		With swirl	3.14	45.7	28.6
<i>Patient 3</i>	56	Without swirl	--	--	19.5
		With swirl	3.38	72.4	46
<i>Patient 4</i>	69	Without swirl	--	--	14.6
		With swirl	8.68	21.2	33.4

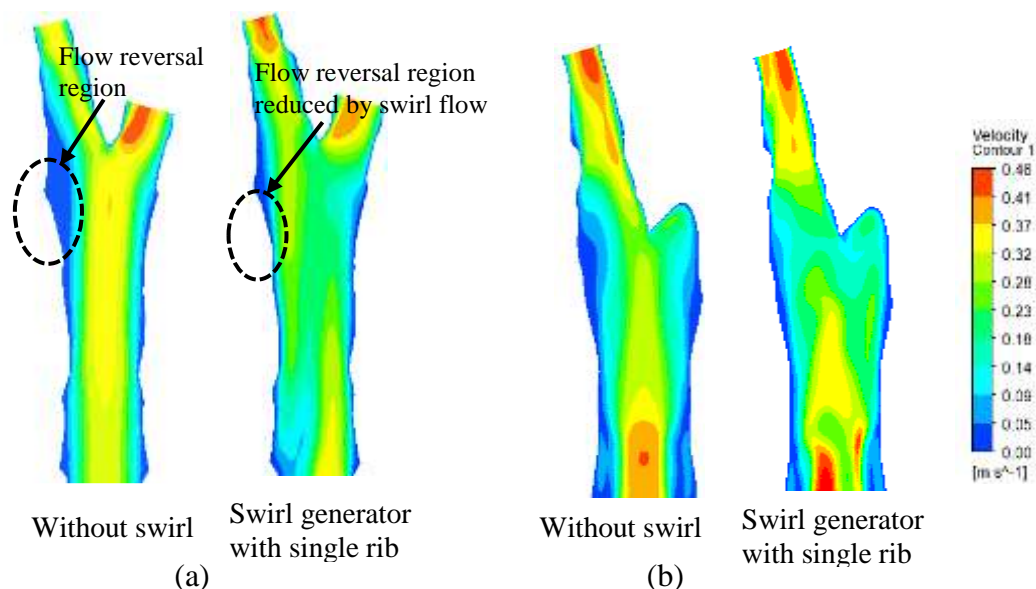


Figure 5.12. Velocity contours at an axial plane during diastolic deceleration time step (a) *Patient 1* (b) *Patient 4*.

Figure 5.12 depicts the typical flow nature in the arterial flow passage. During poiseuille flow inlet (without swirl), flow is stably propagated along the arterial passage without much exchange of momentum in the radial direction. As a result, large recirculations and low velocity wakes are created at the bifurcated regions (Figure 5.12

base cases). Unlike to this, when a swirl is introduced at the inlet, the newly generated vortices from the swirl generator, distributes centerline velocity towards the outer wall periphery. Hence near the wall, flow gets energized and this significantly reduce the recirculation region length and enhances the WSS at this region. The helical flow movement inside the arterial passage washes out the large number of recirculation zones which are presented in the bifurcation zone.

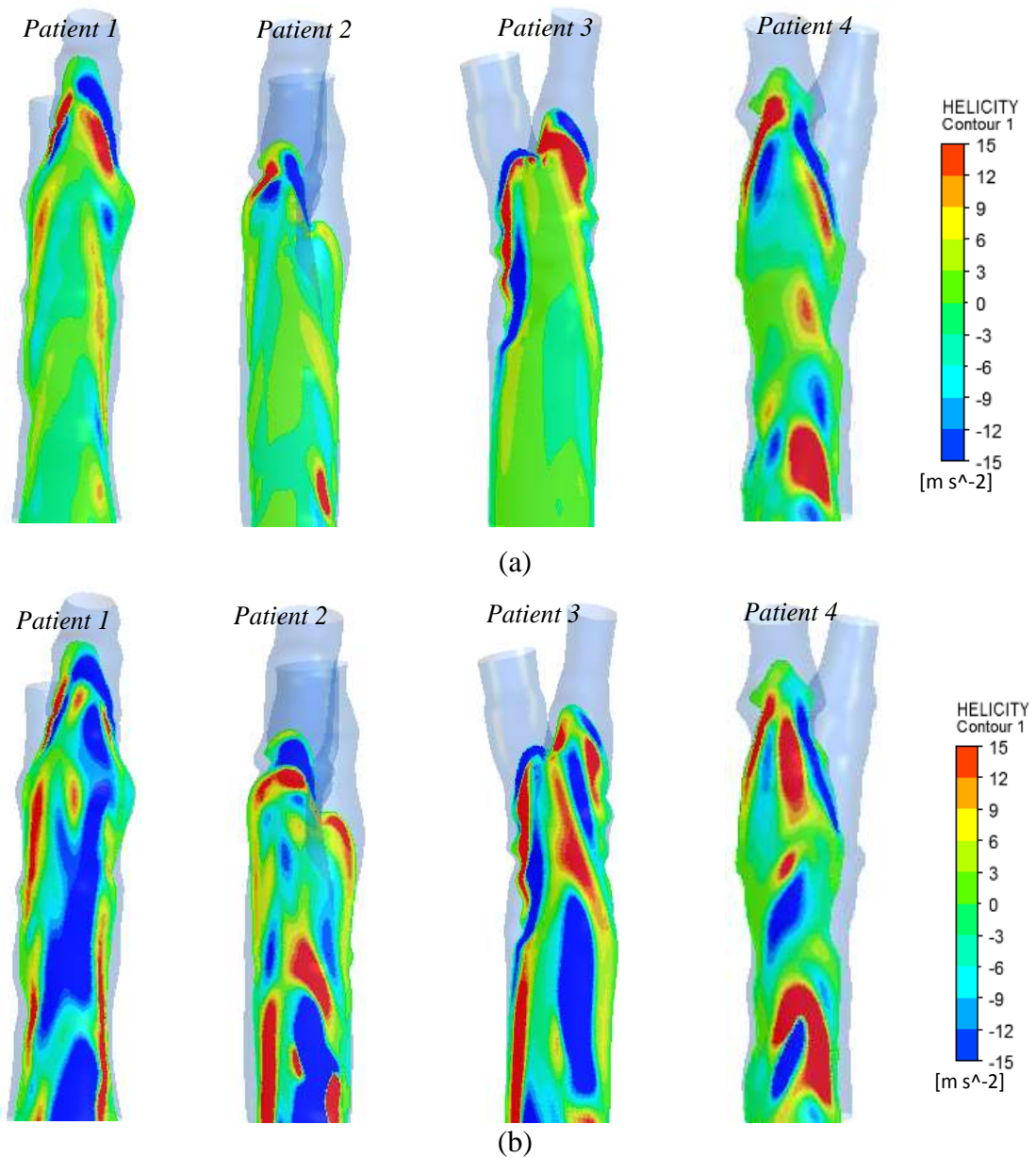


Figure 5.13. Distributed helicity contours during diastolic deceleration time step (a) cases without swirl generator (b) cases with swirl generator.

5.4.3 Effect of relative residence time (RRT)

Swirling strength of the flow can be represented with helicity flow parameter as shown in the Figure 5.13. All four cases with swirl generator are compared with the respective base case models (i.e. without swirl generator) during the decelerating time instance. Induced swirl flow in the cardiac cycle interact with the elongated weaker vortices near the outer wall region. For arterial passage, without swirl generator the helicity contours are seen predominantly near the bifurcation zone only. The secondary flow generated at this region causes the formation of this helicity. They are comparatively weaker and more localized. With the introduction of helical flow through swirl generator, the entire arterial passage is filled with helicities of positive and negative spin. Unlike the base case, the induced helicity contours are much more elongated and they produce stronger shear layer which can wash away the degenerative material which may possibly settle at the low velocity regions. As a result, they exhibit a significant reduction in the RRT values in comparison with the base case.

5.5 Summary of the chapter

Computational simulation of four realistic models are carried out to understand the effect of degree of stenosis on the temporal and spatial variation of wall shear and oscillatory shear.

- Present study recommend to use of normalized wall shear stress rather than the actual wall shear while comparing cases with varying stenosis.
- The high DOS models show smaller values of normalized WSS in the CCA but a larger value in the ICA. For clinical use, in order to represent the risk, it is recommended to use the average value of oscillatory shear than the maximum value.
- Use of limiting streamlines is a convenient method to identify the probable locations of the plaque progression.
- The bulk flow hemodynamics is represented with the direction of resultant vorticity. It reveals that, after the bifurcation zone a change of spin happens

with the resultant vorticity due to the secondary flows originated from the inner wall of the bifurcation zone.

- Induced swirl flow in the patient specific models, significantly reduces the RRT of fluid near the endothelium layer. Enhanced helical flow helps to wash out the recirculation and/or low velocity regions in the arterial passage.

6 CONCLUSIONS

The present work represents the detailed computational investigations of hemodynamics through straight and bifurcated arteries. Effect of different pulse frequencies on the hemodynamics of a straight stenosed artery has been investigated with atherogenic particles behavior through discrete phase modelling. Due to the low and oscillatory shear stress, atherogenic particles will settle at the separated and recirculated regions. To wash out the atherogenic particles a new swirl generator has been developed and has been tested in the arterial passage of bifurcated arteries. The swirl generator induces helicity to the blood flow, and thereby washes away the atherogenic particles that may settle at the low wall shear stress regions. This is evident from the reduced residence time of the fluid layers in these regions. To test the feasibility of the designed swirl generator, it has been implanted in the real patient specific models. The helical flow structures in the patient specific carotid bifurcated arteries minimizes the recirculation zones and keeps arterial wall clean without affecting the flow resistance. Following conclusions are derived from this study.

6.1 Studies on the symmetric and the asymmetric stenosed models

The effect of pulse flow rate on the hemodynamics and atherogenic particles behavior has been studied through discrete phase modelling using straight, idealized, stenosed geometries. It is observed that the magnitude of helicity in the post-stenotic region can be considered as an indicator for the progression of the atherosclerosis, as it directly influences the particle residence time (*PRT*) at that region. The asymmetric stenosis model exhibits less helical flow structure than the symmetric stenosis model. The vortical structures or the flow disturbances are not getting transported to the downstream side of the flow, which enhances the mass transport in the arterial flow. This triggers further occlusion/plaque build-up at the post-stenotic region.

The mean *PRT* values of the atherogenic particles are one order higher than the symmetric stenosis model. On the other hand, symmetric stenosis induces more helicity in the flow structure and hence the chances of occlusion of new cells on the arterial wall are minimal. The average residence time (mean *PRT*) for the symmetric stenosis model decreases with the Womersley number due to the increased helicity. Contrary to

this, the mean *PRT* value increases with the Womersley number for asymmetric stenosis model. More number of localized vortices are found to occur in the asymmetric stenosed model. Unlike the symmetric model, the vortices formed in the post-stenotic regions are not getting transported in the asymmetric model. The formation of secondary vortices in asymmetric model leads to severe undulations in the WSS distribution distal to the stenosis throat region. The extent of asymmetry in a diseased artery may be considered as a useful parameter in understanding the rate of progression of atherosclerosis.

Fluid structure interaction studies with the flexible wall assumption shows that the wall displacement, for asymmetrically stenosed model, is 50% more than the symmetric case. With increase of pulse rate the stress distribution on the arterial wall as well as the wall displacement increases. Due to the presence of larger curvature wall at one side, flow is pushed to one side of the arterial wall leading to higher stress in the asymmetric stenosis. It may cause an early vascular injury (plaque rupture) hence an increased asymmetric nature of stenosis is more precarious.

6.2 Effect of swirl flow in the idealized bifurcated artery

For inducing helicity, conceptual design of the swirl generator has been proposed. It has been observed that, generation of helical flow and disturbed shear layers in the complex flow field effectively suppresses the recirculation zones. Thus the, accumulation of atherogenic particles is minimized by controlling the relative residence time of fluid layer near the wall. The height of the rib, helical angle and number of ribs have been varied systematically to identify an ideal swirl generator which brings down the RRT while offering minimum flow resistance. The helical flow makes redistribution of the kinetic energy from the center to the periphery. This outward bound energy transfer from the central region, makes the boundary layer fluid gets energized causing a delay in the separation of fluid layer from the arterial wall. Among the tested configurations, swirl generator with single rib and 180 deg. helical angle offers 36% reduction in the relative residence time without creating any significant flow resistance. Detailed flow analysis revealed the existence of stronger shear layers

due to the induced helicity which washes out the weaker vortices component by the action of swirl flow.

Separate studies have been carried out to understand the stress distribution on the arterial wall. Comparisons are made between model with swirl generator and without swirl generator (base case). Enhanced swirl flow in the arterial passage improves the flow behavior during the diastolic phase. The increased WSS during the deceleration phase minimizes the particles residence time. The Vonmises stress on the interaction surface is almost similar for both cases. This indicates that there is no significant additional stress acting on the wall by the introduction of swirl generator.

6.3 Studies on patient specific carotid artery models

Computational investigations on four patient specific models have been carried out to understand the effect of degree of stenosis on the temporal and spatial variation of wall shear and oscillatory shear. Additionally, the suitability of swirl generator has been tested in these real arterial geometries. The study reveals that, use of normalized wall shear stress is recommended rather than the actual wall shear while comparing cases with varying degree of stenosis (DOS). The high DOS models show smaller values of normalized WSS in the CCA but a larger value in the ICA. For clinical use, in order to represent the risk, it is recommended to use the average value of oscillatory shear than the maximum value. Surface streamlines are proven to be a convenient method to identify the probable locations of the plaque progression. The bulk flow hemodynamics is represented with the direction of resultant vorticity. It reveals that, after the bifurcation zone a change of spin happens with the resultant vorticity due to the secondary flows originated from the inner wall of the bifurcation zone. Detailed flow analysis revealed that induced swirl flow is not generating significant flow resistance and it enhances swirl in the pulsatile flow thereby bringing down the relative residence time (RRT). The percentage reduction in the RRT is different for each models, suggesting that the topology of the lumen wall has significant impact on the residence time.

6.4 Limitations and suggestions for future work

The following areas have been identified for future studies:

- The present study is focused on only the conceptual design of the swirl generator from the hemodynamics perspective. The study can be extended further in identifying the suitable biomaterials for the swirl generator.
- The present investigation has not considered the realistic biomechanical wall properties (lipid pool) while studying the flexible wall behavior in the idealized models. In future study, this may be considered on a patient specific basis in consultation with clinicians.
- Due to the unavailability of individual patient specific data (velocity profile and transient pressure variation), boundary conditions are taken from the literature for the present study irrespective of their degree of stenosis. In future studies, patient specific velocity waveform may be implemented for all the realistic models.
- The present study has not been considered the flexible wall behavior during real patient data analysis due to the poor quality of scanned images. The study can be extended further by obtaining good quality scanned images from real patients and carry out fluid structure interaction studies on those data.

REFERENCES

- Ahmed, S. A. and Giddens, D. P. (1984). "Pulsatile poststenotic flow studies with laser Doppler anemometry." *Journal of biomechanics*, 17(9), 695-705.
- Anayiotos, A. and Papaharilaou, Y. (2011). Vascular hemodynamics of the carotid bifurcation and its relation to arterial disease *Ultrasound and Carotid Bifurcation Atherosclerosis* (pp. 41-51): Springer.
- Antiga, L., Ene-Iordache, B., Caverni, L., Cornalba, G. P. and Remuzzi, A. (2002). "Geometric reconstruction for computational mesh generation of arterial bifurcations from CT angiography." *Computerized Medical Imaging and Graphics*, 26(4), 227-235.
- Arzani, A., Gambaruto, A. M., Chen, G. and Shadden, S. C. (2017). "Wall shear stress exposure time: a Lagrangian measure of near-wall stagnation and concentration in cardiovascular flows." *Biomechanics and modeling in mechanobiology*, 16(3), 787-803.
- Augusto, L., Lopes, G. and Goncalves, J. (2016). "A CFD study of deposition of pharmaceutical aerosols under different respiratory conditions." *Brazilian Journal of Chemical Engineering*, 33(3), 549-558.
- Babuska, I. and Oden, J. T. (2004). "Verification and validation in computational engineering and science: basic concepts." *Computer methods in applied mechanics and engineering*, 193(36-38), 4057-4066.
- Baldewsing, R. A., de Korte, C. L., Schaar, J. A., Mastik, F. and van der Steen, A. F. (2004). "Finite element modeling and intravascular ultrasound elastography of vulnerable plaques: parameter variation." *Ultrasonics*, 42(1-9), 723-729.
- Balossino, R., Pennati, G., Migliavacca, F., Formaggia, L., Veneziani, A., Tuveri, M. and Dubini, G. (2009). "Influence of boundary conditions on fluid dynamics in models of the cardiovascular system: a multiscale approach applied to the carotid bifurcation." *Comput. Meth. Biomech. Biomed. Eng.*, 12(1).
- Banerjee, M. K., Ganguly, R. and Datta, A. (2012). "Effect of pulsatile flow waveform and Womersley number on the flow in stenosed arterial geometry." *ISRN Biomathematics*, 2012.
- Banks, J. and Bressloff, N. (2007). "Turbulence modeling in three-dimensional stenosed arterial bifurcations." *Journal of biomechanical engineering*, 129(1), 40-50.
- Berger, S. and Jou, L.-D. (2000). "Flows in stenotic vessels." *Annual review of fluid mechanics*, 32(1), 347-382.
- Bharadvaj, B., Mabon, R. and Giddens, D. (1982). "Steady flow in a model of the human carotid bifurcation. Part I—flow visualization." *Journal of biomechanics*, 15(5), 349-362.

- Bonfanti, M., Balabani, S., Alimohammadi, M., Agu, O., Homer-Vanniasinkam, S. and Díaz-Zuccarini, V. (2018). "A simplified method to account for wall motion in patient-specific blood flow simulations of aortic dissection: Comparison with fluid-structure interaction." *Medical Engineering & Physics*.
- Buchanan Jr, J., Kleinstreuer, C. and Comer, J. (2000). "Rheological effects on pulsatile hemodynamics in a stenosed tube." *Computers & Fluids*, 29(6), 695-724.
- Caro, C., Pedley, T., Schroter, R. and Seed, W. "et, al.,(1978) The Mechanics of the Circulation." *Oxford University Press*.
- Caro, C. G., Doorly, D. J., Tarnawski, M., Scott, K. T., Long, Q. and Dumoulin, C. L. (1996). "Non-planar curvature and branching of arteries and non-planar-type flow." *Proc. R. Soc. Lond. A*, 452(1944), 185-197.
- Chen, Y., Zhang, P., Deng, X., Fan, Y., Xing, Y. and Xing, N. (2017). "Improvement of hemodynamic performance using novel helical flow vena cava filter design." *Scientific reports*, 7, 40724.
- Chiastra, C., Gallo, D., Tasso, P., Iannaccone, F., Migliavacca, F., Wentzel, J. J. and Morbiducci, U. (2017). "Healthy and diseased coronary bifurcation geometries influence near-wall and intravascular flow: A computational exploration of the hemodynamic risk." *Journal of biomechanics*, 58, 79-88.
- Constantinides, P. (1984). "Atherosclerosis—A General Survey and Synthesis." *Pathology and Immunopathology Research*, 3(6), 477-498.
- de la Arteria, N. d. B. and en Relación, C. C. (2006). "Common carotid artery bifurcation levels related to clinical relevant anatomical landmarks." *Int. J. Morphol*, 24(3), 413-416.
- Ethier, C. R. (2002). "Computational modeling of mass transfer and links to atherosclerosis." *Annals of biomedical engineering*, 30(4), 461-471.
- Fabbri, D., Long, Q., Das, S. and Pinelli, M. (2014). "Computational modelling of emboli travel trajectories in cerebral arteries: influence of microembolic particle size and density." *Biomechanics and modeling in mechanobiology*, 13(2), 289-302.
- Fan, Y., Xu, Z., Jiang, W., Deng, X., Wang, K. and Sun, A. (2008). "An S-type bypass can improve the hemodynamics in the bypassed arteries and suppress intimal hyperplasia along the host artery floor." *Journal of biomechanics*, 41(11), 2498-2505.
- Fatouraee, N., Deng, X., Champlain, A. and Guidoin, R. (1998). "Concentration polarization of low density lipoproteins (LDL) in the arterial system." *Annals of the New York Academy of Sciences*, 858(1), 137-146.
- Frattolin, J., Zarandi, M. M., Pagiatakis, C., Bertrand, O. F. and Mongrain, R. (2015). "Numerical study of stenotic side branch hemodynamics in true bifurcation lesions." *Computers in biology and medicine*, 57, 130-138.

Friedman, M. H., Hutchins, G. M., Barger, C. B., Deters, O. J. and Mark, F. F. (1981). "Correlation between intimal thickness and fluid shear in human arteries." *Atherosclerosis*, 39(3), 425-436.

Fytanidis, D., Soulis, J. and Giannoglou, G. (2014). "Patient-specific arterial system flow oscillation." *Hippokratia*, 18(2), 162.

Gallo, D., Steinman, D. A., Bijari, P. B. and Morbiducci, U. (2012). "Helical flow in carotid bifurcation as surrogate marker of exposure to disturbed shear." *Journal of biomechanics*, 45(14), 2398-2404.

Gataulin, Y. A., Zaitsev, D. K., Smirnov, E. M., Fedorova, E. A. and Yukhnev, A. D. (2015). "Weakly swirling flow in a model of blood vessel with stenosis: Numerical and experimental study." *St. Petersburg Polytechnical University Journal: Physics and Mathematics*, 1(4), 364-371.

Germano, M., Piomelli, U., Moin, P. and Cabot, W. H. (1991). "A dynamic subgrid-scale eddy viscosity model." *Physics of Fluids A: Fluid Dynamics*, 3(7), 1760-1765.

Guleren, K. M. (2013). "Numerical flow analysis of coronary arteries through concentric and eccentric stenosed geometries." *Journal of biomechanics*, 46(6), 1043-1052.

Gupta, A., Baradaran, H., Kamel, H., Pandya, A., Mangla, A., Dunning, A., Marshall, R. S. and Sanelli, P. C. (2014). "Evaluation of computed tomography angiography plaque thickness measurements in high-grade carotid artery stenosis." *Stroke*, 45(3), 740-745.

Gupta, A., Mtui, E., Baradaran, H., Salama, G., Pandya, A., Kamel, H., Giambrone, A. and Sanelli, P. (2015). "CT angiographic features of symptom-producing plaque in moderate-grade carotid artery stenosis." *American Journal of Neuroradiology*, 36(2), 349-354.

Ha, H., Choi, W. and Lee, S. J. (2015). "Beneficial fluid-dynamic features of pulsatile swirling flow in 45 end-to-side anastomosis." *Medical Engineering and Physics*, 37(3), 272-279.

Ha, H., Choi, W., Park, H. and Lee, S. J. (2015). "Effect of swirling blood flow on vortex formation at post-stenosis." *Proceedings of the Institution of Mechanical Engineers, Part H: Journal of Engineering in Medicine*, 229(2), 175-183.

Ha, H., Hwang, D., Choi, W.-R., Baek, J. and Lee, S. J. (2014). "Fluid-dynamic optimal design of helical vascular graft for stenotic disturbed flow." *PloS one*, 9(10), e111047.

Ha, H. and Lee, S.-J. (2013). "Hemodynamic features and platelet aggregation in a stenosed microchannel." *Microvascular research*, 90, 96-105.

Ha, H. and Lee, S. J. (2014). "Effect of pulsatile swirling flow on stenosed arterial blood flow." *Medical Engineering and Physics*, 36(9), 1106-1114.

- Haque, M. R., Hossain, M. E. and Hasan, A. T. (2014). "Effect of non-Newtonian behaviour on fluid structural interaction for flow through a model stenosed artery." *Procedia Engineering*, 90, 358-363.
- Hasis, F. B. A., Krishna, P. M., Aravind, G., Deepu, M. and Shine, S. (2018). "Thermo hydraulic performance analysis of twisted sinusoidal wavy microchannels." *International Journal of Thermal Sciences*, 128, 124-136.
- Himburg, H. A., Grzybowski, D. M., Hazel, A. L., LaMack, J. A., Li, X.-M. and Friedman, M. H. (2004). "Spatial comparison between wall shear stress measures and porcine arterial endothelial permeability." *American Journal of Physiology-Heart and Circulatory Physiology*, 286(5), H1916-H1922.
- Hoi, Y., Wasserman, B. A., Xie, Y. J., Najjar, S. S., Ferruci, L., Lakatta, E. G., Gerstenblith, G. and Steinman, D. A. (2010). "Characterization of volumetric flow rate waveforms at the carotid bifurcations of older adults." *Physiological measurement*, 31(3), 291.
- Houston, J. G., Gandy, S. J., Milne, W., Dick, J. B., Belch, J. J. and Stonebridge, P. A. (2004). "Spiral laminar flow in the abdominal aorta: a predictor of renal impairment deterioration in patients with renal artery stenosis?". *Nephrology Dialysis Transplantation*, 19(7), 1786-1791.
- Huang, Y., Teng, Z., Sadat, U., Graves, M. J., Bennett, M. R. and Gillard, J. H. (2014). "The influence of computational strategy on prediction of mechanical stress in carotid atherosclerotic plaques: comparison of 2D structure-only, 3D structure-only, one-way and fully coupled fluid-structure interaction analyses." *Journal of biomechanics*, 47(6), 1465-1471.
- Hunt, J. and Hussain, F. (1991). "A note on velocity, vorticity and helicity of inviscid fluid elements." *Journal of Fluid mechanics*, 229, 569-587.
- Jabir, E. and Lal, S. A. (2016). "Numerical analysis of blood flow through an elliptic stenosis using large eddy simulation." *Proceedings of the Institution of Mechanical Engineers, Part H: Journal of Engineering in Medicine*, 230(8), 709-726.
- Jahangiri, M., Saghafian, M. and Sadeghi, M. R. (2017). "Numerical simulation of non-Newtonian models effect on hemodynamic factors of pulsatile blood flow in elastic stenosed artery." *Journal of Mechanical Science and Technology*, 31(2), 1003-1013.
- Johnston, B. M., Johnston, P. R., Corney, S. and Kilpatrick, D. (2004). "Non-Newtonian blood flow in human right coronary arteries: steady state simulations." *Journal of biomechanics*, 37(5), 709-720.
- Johnston, B. M., Johnston, P. R., Corney, S. and Kilpatrick, D. (2006). "Non-Newtonian blood flow in human right coronary arteries: transient simulations." *Journal of biomechanics*, 39(6), 1116-1128.

Kabinejadian, F., McElroy, M., Ruiz-Soler, A., Leo, H. L., Slevin, M. A., Badimon, L. and Keshmiri, A. (2016). "Numerical assessment of novel helical/spiral grafts with improved hemodynamics for distal graft anastomoses." *PloS one*, 11(11), e0165892.

Kanyanta, V., Ivankovic, A. and Karac, A. (2009). "Validation of a fluid–structure interaction numerical model for predicting flow transients in arteries." *Journal of biomechanics*, 42(11), 1705-1712.

Kefayati, S. and Poepping, T. L. (2013). "Transitional flow analysis in the carotid artery bifurcation by proper orthogonal decomposition and particle image velocimetry." *Medical Engineering and Physics*, 35(7), 898-909.

Kilner, P. J., Yang, G. Z., Mohiaddin, R. H., Firmin, D. N. and Longmore, D. B. (1993). "Helical and retrograde secondary flow patterns in the aortic arch studied by three-directional magnetic resonance velocity mapping." *Circulation*, 88(5), 2235-2247.

Kolář, V. (2007). "Vortex identification: New requirements and limitations." *International journal of heat and fluid flow*, 28(4), 638-652.

Ku, D. N. (1997). "Blood flow in arteries." *Annual review of fluid mechanics*, 29(1), 399-434.

Ku, D. N. and Giddens, D. P. (1983). "Pulsatile flow in a model carotid bifurcation." *Arteriosclerosis, thrombosis, and vascular biology*, 3(1), 31-39.

Ku, D. N., Giddens, D. P., Zarins, C. K. and Glagov, S. (1985). "Pulsatile flow and atherosclerosis in the human carotid bifurcation. Positive correlation between plaque location and low oscillating shear stress." *Arteriosclerosis, thrombosis, and vascular biology*, 5(3), 293-302.

Lantz, J., Henriksson, L., Persson, A., Karlsson, M. and Ebbens, T. (2016). "Patient-specific simulation of cardiac blood flow from high-resolution computed tomography." *Journal of biomechanical engineering*, 138(12), 121004.

Lebanon, N. (2003). *FLUENT 6.1 User's Guide*.

Lee, E. S., Caldwell, M. P., Tretinyak, A. S. and Santilli, S. M. (2001). "Supplemental oxygen controls cellular proliferation and anastomotic intimal hyperplasia at a vascular graft-to-artery anastomosis in the rabbit." *Journal of vascular surgery*, 33(3), 608-613.

Lee, K. E., Lee, J. S. and Yoo, J. Y. (2011). "A numerical study on steady flow in helically sinuous vascular prostheses." *Medical Engineering and Physics*, 33(1), 38-46.

Lee, R. (2000). "Atherosclerotic lesion mechanics versus biology." *Zeitschrift für Kardiologie*, 89(2), S080-S084.

- Lee, S.-W. and Steinman, D. A. (2007). "On the relative importance of rheology for image-based CFD models of the carotid bifurcation." *Journal of biomechanical engineering*, 129(2), 273-278.
- Li, G., Hu, R. and Gao, F. (2015). "Numerical Simulation of Coronary Artery Stenosis Before and After Stenting." *Journal of Medical and Biological Engineering*, 35(4), 528-534.
- Li, M., Beech-Brandt, J., John, L., Hoskins, P. and Easson, W. (2007). "Numerical analysis of pulsatile blood flow and vessel wall mechanics in different degrees of stenoses." *Journal of biomechanics*, 40(16), 3715-3724.
- Liang, H. and Maxworthy, T. (2005). "An experimental investigation of swirling jets." *Journal of Fluid Mechanics*, 525, 115-159.
- Lilly, D. K. (1992). "A proposed modification of the Germano subgrid-scale closure method." *Physics of Fluids A: Fluid Dynamics*, 4(3), 633-635.
- Linge, F., Hye, M. A. and Paul, M. C. (2014). "Pulsatile spiral blood flow through arterial stenosis." *Computer methods in biomechanics and biomedical engineering*, 17(15), 1727-1737.
- Liu, B. (2007). "The influences of stenosis on the downstream flow pattern in curved arteries." *Medical Engineering and Physics*, 29(8), 868-876.
- Liu, X., Sun, A., Fan, Y. and Deng, X. (2015). "Physiological significance of helical flow in the arterial system and its potential clinical applications." *Annals of biomedical engineering*, 43(1), 3-15.
- Long, Q., Xu, X., Ramnarine, K. and Hoskins, P. (2001). "Numerical investigation of physiologically realistic pulsatile flow through arterial stenosis." *Journal of biomechanics*, 34(10), 1229-1242.
- Ma, P., Li, X. and Ku, D. N. (1997). "Convective mass transfer at the carotid bifurcation." *Journal of biomechanics*, 30(6), 565-571.
- May, P., Arrouvel, C., Revol, M., Servant, J. M. and Vicaut, E. (2002). "Detection of hemodynamic turbulence in experimental stenosis: an in vivo study in the rat carotid artery." *Journal of vascular research*, 39(1), 21-29.
- Moffatt, H. and Tsinober, A. (1992). "Helicity in laminar and turbulent flow." *Annual review of fluid mechanics*, 24(1), 281-312.
- Morbiducci, U., Gallo, D., Massai, D., Consolo, F., Ponzini, R., Antiga, L., Bignardi, C., Deriu, M. A. and Redaelli, A. (2010). "Outflow conditions for image-based hemodynamic models of the carotid bifurcation: implications for indicators of abnormal flow." *Journal of biomechanical engineering*, 132(9), 091005.

Morbiducci, U., Ponzini, R., Rizzo, G., Cadioli, M., Esposito, A., De Cobelli, F., Del Maschio, A., Montevecchi, F. M. and Redaelli, A. (2009). "In vivo quantification of helical blood flow in human aorta by time-resolved three-dimensional cine phase contrast magnetic resonance imaging." *Annals of biomedical engineering*, 37(3), 516.

Morbiducci, U., Ponzini, R., Rizzo, G., Cadioli, M., Esposito, A., Montevecchi, F. M. and Redaelli, A. (2011). "Mechanistic insight into the physiological relevance of helical blood flow in the human aorta: an in vivo study." *Biomechanics and modeling in mechanobiology*, 10(3), 339-355.

Morsi, S. and Alexander, A. (1972). "An investigation of particle trajectories in two-phase flow systems." *Journal of Fluid Mechanics*, 55(2), 193-208.

Motomiya, M. and Karino, T. (1984). "Flow patterns in the human carotid artery bifurcation." *Stroke*, 15(1), 50-56.

Mukherjee, D., Padilla, J. and Shadden, S. C. (2016). "Numerical investigation of fluid–particle interactions for embolic stroke." *Theoretical and Computational Fluid Dynamics*, 30(1-2), 23-39.

Myers, J., Moore, J., Ojha, M., Johnston, K. and Ethier, C. (2001). "Factors influencing blood flow patterns in the human right coronary artery." *Annals of biomedical engineering*, 29(2), 109-120.

Nguyen, K. T., Clark, C. D., Chancellor, T. J. and Papavassiliou, D. V. (2008). "Carotid geometry effects on blood flow and on risk for vascular disease." *Journal of biomechanics*, 41(1), 11-19.

Pagiatakis, C., Tardif, J.-C., L'Allier, P. L. and Mongrain, R. (2017). "Effect of stenosis eccentricity on the functionality of coronary bifurcation lesions—a numerical study." *Medical & biological engineering & computing*, 55(12), 2079-2095.

Papathanasopoulou, P., Zhao, S., Köhler, U., Robertson, M. B., Long, Q., Hoskins, P., Yun Xu, X. and Marshall, I. (2003). "MRI measurement of time-resolved wall shear stress vectors in a carotid bifurcation model, and comparison with CFD predictions." *Journal of Magnetic Resonance Imaging*, 17(2), 153-162.

Paul, M. and Molla, M. M. (2012). "Investigation of physiological pulsatile flow in a model arterial stenosis using large-eddy and direct numerical simulations." *Applied Mathematical Modelling*, 36(9), 4393-4413.

Paul, M. C. and Larman, A. (2009). "Investigation of spiral blood flow in a model of arterial stenosis." *Medical Engineering and Physics*, 31(9), 1195-1203.

Perktold, K. and Rappitsch, G. (1995). "Computer simulation of local blood flow and vessel mechanics in a compliant carotid artery bifurcation model." *Journal of biomechanics*, 28(7), 845-856.

- Perktold, K., Resch, M. and Peter, R. O. (1991). "Three-dimensional numerical analysis of pulsatile flow and wall shear stress in the carotid artery bifurcation." *Journal of biomechanics*, 24(6), 409-420.
- Peterson, S. D. and Plesniak, M. W. (2008). "The influence of inlet velocity profile and secondary flow on pulsatile flow in a model artery with stenosis." *Journal of Fluid Mechanics*, 616, 263-301.
- Pinto, S. and Campos, J. (2016). "Numerical study of wall shear stress-based descriptors in the human left coronary artery." *Computer methods in biomechanics and biomedical engineering*, 19(13), 1443-1455.
- Raz, S., Einav, S., Alemu, Y. and Bluestein, D. (2007). "DPIV prediction of flow induced platelet activation—comparison to numerical predictions." *Annals of biomedical engineering*, 35(4), 493-504.
- Richardson, P. D., Davies, M. and Born, G. (1989). "Influence of plaque configuration and stress distribution on fissuring of coronary atherosclerotic plaques." *The Lancet*, 334(8669), 941-944.
- Roache, P. J. (1998). *Verification and validation in computational science and engineering* (Vol. 895): Hermosa Albuquerque, NM.
- Ryval, J., Straatman, A. and Steinman, D. (2004). "Two-equation turbulence modeling of pulsatile flow in a stenosed tube." *Journal of biomechanical engineering*, 126(5), 625-635.
- Schoenhagen, P., Ziada, K. M., Kapadia, S. R., Crowe, T. D., Nissen, S. E. and Tuzcu, E. M. (2000). "Extent and direction of arterial remodeling in stable versus unstable coronary syndromes: an intravascular ultrasound study." *Circulation*, 101(6), 598-603.
- Schulz, U. G. and Rothwell, P. M. (2001). "Major variation in carotid bifurcation anatomy: a possible risk factor for plaque development?". *Stroke*, 32(11), 2522-2529.
- Shah, P. K. (2003). "Mechanisms of plaque vulnerability and rupture." *Journal of the American college of cardiology*, 41(4 Supplement), S15-S22.
- Sherwin, S. and Blackburn, H. M. (2005). "Three-dimensional instabilities and transition of steady and pulsatile axisymmetric stenotic flows." *Journal of Fluid Mechanics*, 533, 297-327.
- Sherwin, S., Shah, O., Doorly, D., Peiro, J., Papaharilaou, Y., Watkins, N., Caro, C. and Dumoulin, C. (2000). "The influence of out-of-plane geometry on the flow within a distal end-to-side anastomosis." *Journal of biomechanical engineering*, 122(1), 86-95.
- Shinke, T., Robinson, K., Burke, M. G., Gilson, P., Mullins, L. P., O'Brien, N., Heraty, K. B., Taylor, C., Cheshire, N. J. and Caro, C. G. (2008). Novel helical stent design

elicits swirling blood flow pattern and inhibits neointima formation in porcine carotid arteries: Am Heart Assoc.

Shuib, A., Hoskins, P. and Easson, W. (2010). "Flow regime characterization in a diseased artery model." *World Acad Sci Eng Technol*, 62, 110.

Smagorinsky, J. (1963). "General circulation experiments with the primitive equations: I. The basic experiment." *Monthly weather review*, 91(3), 99-164.

Soulis, J. V., Lampri, O. P., Fytanidis, D. K. and Giannoglou, G. D. (2011). *Relative residence time and oscillatory shear index of non-Newtonian flow models in aorta*. Paper presented at the Biomedical Engineering, 2011 10th International Workshop on.

Steinman, D. A., Poepping, T. L., Tambasco, M., Rankin, R. N. and Holdsworth, D. W. (2000). "Flow patterns at the stenosed carotid bifurcation: effect of concentric versus eccentric stenosis." *Annals of biomedical engineering*, 28(4), 415-423.

Stonebridge, P. and Brophy, C. (1991). "Spiral laminar flow in arteries?". *The Lancet*, 338(8779), 1360-1361.

Stonebridge, P., Buckley, C., Thompson, A. and Dick, J. (2004). "Non spiral and spiral (helical) flow patterns in stenoses: in vitro observations using spin and gradient echo magnetic resonance imaging (MRI) and computational fluid dynamic modeling." *International angiology*, 23(3), 276.

Sun, A., Fan, Y. and Deng, X. (2010). "Numerical comparative study on the hemodynamic performance of a new helical graft with noncircular cross section and swirlgraft." *Artificial organs*, 34(1), 22-27.

Tan, F., Soloperto, G., Bashford, S., Wood, N., Thom, S., Hughes, A. and Xu, X. (2008). "Analysis of flow disturbance in a stenosed carotid artery bifurcation using two-equation transitional and turbulence models." *Journal of biomechanical engineering*, 130(6), 061008.

Tang, D., Teng, Z., Canton, G., Yang, C., Ferguson, M., Huang, X., Zheng, J., Woodard, P. K. and Yuan, C. (2009). "Sites of rupture in human atherosclerotic carotid plaques are associated with high structural stresses: an in vivo MRI-based 3D fluid-structure interaction study." *Stroke*, 40(10), 3258-3263.

Tang, D., Yang, C., Huang, Y. and Ku, D. N. (1999). "Wall stress and strain analysis using a three-dimensional thick-wall model with fluid-structure interactions for blood flow in carotid arteries with stenoses." *Computers & Structures*, 72(1-3), 341-356.

Tang, D., Yang, C., Kobayashi, S. and Ku, D. N. (2004). "Effect of a lipid pool on stress/strain distributions in stenotic arteries: 3-D fluid-structure interactions (FSI) models." *Journal of biomechanical engineering*, 126(3), 363-370.

- Tang, D., Yang, C., Kobayashi, S., Zheng, J. and Vito, R. P. (2003). "Effect of stenosis asymmetry on blood flow and artery compression: a three-dimensional fluid-structure interaction model." *Annals of biomedical engineering*, 31(10), 1182-1193.
- Tang, D., Yang, C., Zheng, J., Woodard, P. K., Saffitz, J. E., Sicard, G. A., Pilgram, T. K. and Yuan, C. (2005). "Quantifying effects of plaque structure and material properties on stress distributions in human atherosclerotic plaques using 3D FSI models." *Journal of biomechanical engineering*, 127(7), 1185-1194.
- Tarbell, J. M. (2003). "Mass transport in arteries and the localization of atherosclerosis." *Annual review of biomedical engineering*, 5(1), 79-118.
- Teng, Z., He, J., Sadat, U., Mercer, J. R., Wang, X., Bahaei, N. S., Thomas, O. M. and Gillard, J. H. (2014). "How does juxtaluminal calcium affect critical mechanical conditions in carotid atherosclerotic plaque? An exploratory study." *IEEE Transactions on Biomedical Engineering*, 61(1), 35-40.
- Tobak, M. and Peake, D. J. (1982). "Topology of three-dimensional separated flows." *Annual review of fluid mechanics*, 14(1), 61-85.
- Tutty, O. (1992). "Pulsatile flow in a constricted channel." *Journal of biomechanical engineering*, 114(1), 50-54.
- Van Canneyt, K., Morbiducci, U., Eloit, S., De Santis, G., Segers, P. and Verdonck, P. (2013). "A computational exploration of helical arterio-venous graft designs." *Journal of biomechanics*, 46(2), 345-353.
- van der Wal, A. C. and Becker, A. E. (1999). "Atherosclerotic plaque rupture—pathologic basis of plaque stability and instability." *Cardiovascular research*, 41(2), 334-344.
- Varghese, S. S., Frankel, S. H. and Fischer, P. F. (2007). "Direct numerical simulation of stenotic flows. Part 1. Steady flow." *Journal of Fluid mechanics*, 582, 253-280.
- Varghese, S. S., Frankel, S. H. and Fischer, P. F. (2008). "Modeling transition to turbulence in eccentric stenotic flows." *Journal of biomechanical engineering*, 130(1), 014503.
- Wong, K. K. L., Cheung, S. C. P., Yang, W. and Tu, J. (2010). "Numerical simulation and experimental validation of swirling flow in spiral vortex ventricular assist device." *International Journal of Artificial Organs*, 33(12), 856-867.
- Zeller, T., Gaines, P. A., Ansel, G. M. and Caro, C. G. (2016). "Helical centerline stent improves patency: two-year results from the randomized mimics trial." *Circulation: Cardiovascular Interventions*, 9(6), e002930.
- Zhang, Z.-G., Zhang, X.-W. and Liu, Y.-X. (2012). "Effects of fluid recirculation on mass transfer from the arterial surface to flowing blood." *Acta Mechanica Sinica*, 28(3), 904-910.

Zhang, Z., Fan, Y. and Deng, X. (2007). "Oxygen transfer in human carotid artery bifurcation." *Acta Mechanica Sinica*, 23(3), 305-309.

Zheng, T., Wen, J., Jiang, W., Deng, X. and Fan, Y. (2014). "Numerical investigation of oxygen mass transfer in a helical-type artery bypass graft." *Computer methods in biomechanics and biomedical engineering*, 17(5), 549-559.

Zovatto, L. and Pedrizzetti, G. (2017). "Fluid flow in a helical vessel in presence of a stenosis." *Meccanica*, 52(3), 545-553.

PATENT

Patent title: “*Swirl Generator for Human Arterial Network*”

Title	Swirl Generator for Human Arterial Network
Application Number	201841010102
Filing date	20/03/2018
Applicant	National Institute of Technology Karnataka
Inventors	1. Anish S 2. Prashantha B

LIST OF PUBLICATIONS

INTERNATIONAL JOURNALS

- 1) Basavaraja, P., Surendran, A., Gupta, A., Saba, L., Laird, J. R., et al., (2017). “Wall shear stress and oscillatory shear index distribution in carotid artery with varying degree of stenosis: a hemodynamic study”. *Journal of Mechanics in Medicine and Biology*, 17(02), 1750037.
- 2) Prashantha, B., Anish, S (2018) “Discrete phase modelling of an asymmetric stenosis artery under different Womersley number” *Arabian Journal of science and Engineering* (10.1007/s13369-018-3391-z).
- 3) Prashantha, B., & Anish, S. (2017). “A comparative CFD study on the hemodynamics of flow through an idealized symmetric and asymmetric stenosed artery”. In *Journal of Physics: Conference Series* (Vol. 822, No. 1, p. 012020). IOP Publishing.
- 4) Prashantha, B., Anish, S., (2017) “A Computational Study on the Stenosis Circularity for a Severe Stenosed Idealized Artery” *Lecture Notes in Mechanical Engineering* (In press).
- 5) Prashantha, B., Anish, S (2017) “A computational hemodynamic study on idealized bifurcated arteries”. *Recent Patents on Mechanical Engineering, International Journal by Bentham Science Publishers* (In press).

- 6) Prashantha, B., Anish, S (2018) “Computational investigations on the hemodynamic performance of a new swirl generator in bifurcated arteries” Computer methods in biomechanics and biomedical engineering (minor reviews submitted).

CONFERENCES

- 1) Prashantha, B., Anish, S “A Comparative CFD Study on the Hemodynamics of Flow through an Idealized Symmetric and Asymmetric Stenosed Artery”. 15th Asian Congress of Fluid Mechanics, Malaysia 2016.
- 2) Prashantha, B., Anish, S (2016). “The influence of symmetric and asymmetric stenosis in the arterial flow: A numerical study”. International Conference on CompFlu 2016.
- 3) Prashantha, B., Anish, S “A Computational Study On The Stenosis Circularity For A Severe Stenosed Idealized Artery”. International Conference on Numerical Heat Transfer and Fluid Flow 2017.
- 4) Prashantha, B., Anish, S “A computational hemodynamic study on idealized bifurcated arteries”. 44th National conference on Fluid Mechanics and Fluid power 2017.

BIODATA

- 1. Name** : Prashantha. B
- 2. Father's Name** : Basavraja. B. S
- 3. Date of Birth** : 23rd November 1989
- 4. Nationality** : Indian
- 5. Marital Status** : Single
- 6. Address** : Department of Mechanical Engineering
National Institute of Technology Karnataka
Surathkal, PO Srinivasnagar 575 025
Karnataka, India.
- 7. Mobile Number** : +91 7353269954
- 8. E-mail id.** : *prashanthb.mech@gmail.com*
- 9. Educational Qualification:**

Qualification	University/Board	Year of Passing
Ph.D. (Mechanical Engineering)	National Institute of Technology Karnataka	2014-2018
M.Tech. (Mechanical Engineering)	Visvesvaraya Technological University, Belgaum	2013
B.E. (Mechanical Engineering)	Kuvempu University, Shimoga (Shankargatta)	2011
